CHALMERS
UNIVERSITY OF TECHNOLOGY

University of Stuttgart
Germany

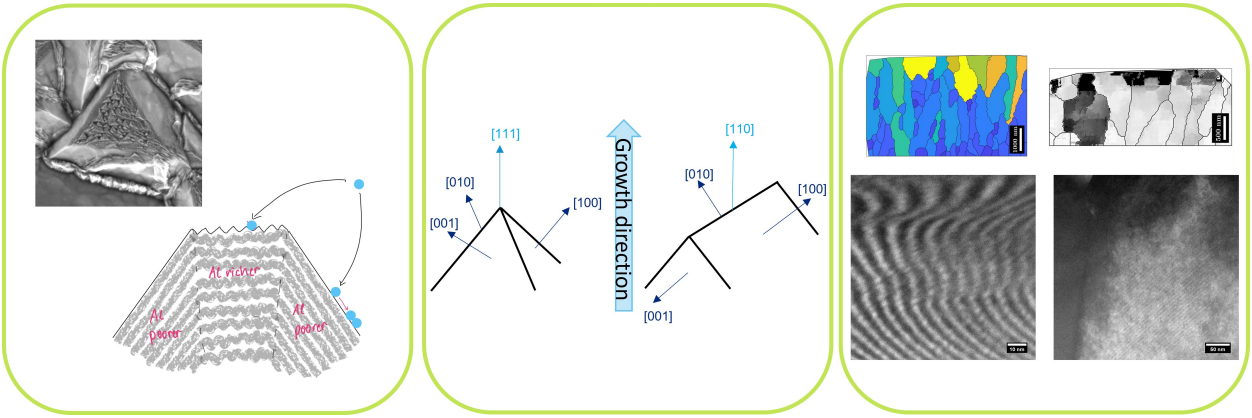

Detailed Microstructure and the Influence of Post-Treatment on CVD TiAlN Wear Resistant Coatings

A study of the microstructure before and after blast-treatment with Al_2O_3 particles by SEM, TEM and TKD

Master's thesis for the Double Degree in Materials Engineering/Science
submitted to Chalmers University of Technology and the University of Stuttgart

MONICA AUDREY MEAD

DEPARTMENT OF PHYSICS
CHALMERS UNIVERSITY OF TECHNOLOGY
Gothenburg, Sweden 2023
www.chalmers.se

Master's thesis 2023

Detailed Microstructure and the Influence of Post-Treatment on CVD TiAlN Wear Resistant Coatings

A study of the microstructure before and after blast-treatment with Al_2O_3 particles by SEM, TEM and TKD

MONICA MEAD

CHALMERS
UNIVERSITY OF TECHNOLOGY

Department of Physics
Division of Microstructure Physics
Chalmers University of Technology
Gothenburg, Sweden 2023

Detailed Microstructure and the Influence of Post-Treatment on CVD TiAlN Wear Resistant Coatings
A study of the microstructure before and after blast-treatment with Al_2O_3 particles by SEM, TEM and TKD
MONICA MEAD

Supervisor: Dr. Olof Bäcke
Examiner (Chalmers): Prof. Dr. Mats Halvarsson
Examiner (University of Stuttgart): Prof. Dr. Dr. h.c. Guido Schmitz

Thesis contributing to the Vinnova project "High-performance nano-structured CVD TiAlN coated cutting tools for difficult-to-cut materials" in collaboration with Walter AG and Sandvik Coromant

Master's Thesis 2023
Department of Physics
Division of Microstructure Physics
Chalmers University of Technology
SE-412 96 Gothenburg
Telephone +46 31 772 1000

Cover: Scanning electron microscopy (SEM) image of a truncated pyramidal grain with many small pyramids on the top surface. Schematic illustrating the characteristics of a truncated grain and shorter diffusion paths to special sites on the surface with many small facets. Schematics of pyramidal and ridge-like grains and their crystallographic orientations. Grain orientation spread and grain reference orientation deviation of a thin foil cross-section of the TiAlN coating deposited by low-pressure chemical vapour deposition (LPCVD). Scanning transmission electron microscopy (STEM) high-angle annular dark field (HAADF) images illustrate the bending and disappearance of nano-lamellae as a result of blasting.

Typeset in LaTeX
Printed by Chalmers Reproservice
Gothenburg, Sweden 2023

Author declaration

I declare that I have developed and written the enclosed thesis completely by myself and that I have not used sources or means without declaration in the text. Any thoughts from others or literal quotations are clearly marked.

The thesis was not used in the same or in a similar version to achieve an academic grading or is being published elsewhere.

The enclosed electronic version is identical to the printed versions.

01.09.2023
Date


Signature

Detailed Microstructure and the Influence of Post-Treatment on CVD TiAlN Wear Resistant Coatings
A study of the microstructure before and after blast-treatment with Al_2O_3 particles by SEM, TEM and TKD
MONICA MEAD
Department of Physics
Chalmers University of Technology

Abstract

The deposition of TiAlN by chemical vapour deposition (CVD) for the application as wear-resistant coatings for cutting tools has been the subject of research interest for numerous years, yet a comprehensive understanding of its growth mechanism and intricate microstructural characteristics remains incomplete. Furthermore, although the positive effect of blast-treatment on the stress state of wear-resistant coatings has received attention in scientific studies, there remains a relative sparsity of research investigating its influence on the microstructure. In this work, the detailed microstructure of nano-lamellar low-pressure CVD TiAlN coatings on cemented carbide substrates and the influence of post-treatment on the microstructure was investigated by scanning electron microscopy (SEM), scanning transmission electron microscopy (STEM) and transmission Kikuchi diffraction (TKD). SEM imaging revealed two distinct types of surface morphologies corresponding to specific grain orientations unveiled by TKD on thin foil cross-sections. As previously shown [1], pyramidal surface morphology is connected to growth in a <111> direction, additionally, a ridge-like surface morphology was connected to growth along <110> directions. Both growth directions enable fast growth with low-energy {100} facets. Furthermore, truncation of pyramidal and ridge-like surface morphologies was observed. A growth mechanism was proposed aiming to explain the characteristics of the truncated grain morphology. Here, strongly facetted surfaces emerging on the truncated grains increase the surface reaction kinetics, leading to an increased Al/Ti-ratio in the core region of the grain compared to its sides with large {100} facets. Blast-treatment of the TiAlN coatings with corundum particles led to plastic deformation up to a few hundred nanometres in depth. Impact jet wear introduced a high defect density and crack or void formation beneath the surface. Plastic deformation of the near-surface region of the coating led to the bending or disappearance of the Ti- and Al-rich lamellae typical in TiAlN coatings prepared by CVD and a continuous lattice rotation in three dimensions. The available data indicates that grains which have grown along one of their <110> directions exhibit a more pronounced lattice rotation when compared to grains that have grown along a <111> direction.

Keywords: TiAlN, LPCVD, lamella, SEM, STEM, TKD, film growth, texture, blasting, plastic deformation.

Acknowledgements

I am delighted to express my deepest gratitude to all people who helped and supported me during the work on this thesis. I am deeply appreciative of my examiner Mats Halvarsson, who welcomed me to work on this thesis and opened the doors for me to get insight into the collaborations with the industrial partners. I greatly value our discussions on the topics and the mentoring, not only on the scientific aspect but also its presentation. My sincere thanks also go to Guido Schmitz, who willingly agreed to be my examiner at the University of Stuttgart. I am thankful to my supervisor Olof Bäcke for his invaluable guidance and expertise in microscopy and support in all questions during the work on this thesis. I want to thank the collaboration partners at Sandvik Coromant and especially Walter Tools for welcoming me to this project, in particular, I want to thank Dirk Stiens for his time introducing me to the CVD deposition at Walter Tools and answering all my questions. I want to convey my thanks to the laboratory staff at Chalmers Materials Analysis Laboratory (CMAL) where all analysis for this work was performed for their help. Special thanks also go to all the people at the Division of Microstructure Physics for creating such a supportive environment and wonderfully random discussions during lunch and fika breaks. Especially, I want to thank Andrea Fazi, Emil Eriksson, Magnus Hörnqvist Colliander and Aina Edgren for their help on the TKD measurements and analysis. I am honoured and incredibly grateful to have received financial support from the International Max-Planck Research School for Condensed Matter Science (IMPRS-CMS), the Baden-Württemberg Stiftung and the Adlerbertska Foreign Student Hospitality Foundation, which enabled me to focus on my studies and research during my Master's studies.

Last but not least, I want to express my deepest gratitude to all the lovely people in my life who always support me, without them I would not be where and who I am today. I am truly thankful to my amazing friends, both those who have been part of my life for years and those that open-heartedly built new friendships with me during my time in Sweden. And finally, I want to thank my family who have always supported and believe in me.

Monica Mead, Gothenburg, July 2023

Acronyms

ADF annular dark field
AEM analytical electron microscopy
APT atom probe tomography
BF bright field
BSE backscattered electrons
CCD charge-coupled device
CVD chemical vapour deposition
DF dark field
DFT density functional theory
EBSD electron backscatter diffraction
EBSP electron backscatter pattern
EDS energy-dispersive x-ray spectroscopy
EELS electron energy loss spectroscopy
fcc face centred cubic
FEG field emission gun
FFT fast Fourier transform
FIB focused ion beam
GOS grain orientation spread
GROD grain reference orientation deviation
HAADF high-angle annular dark field
IPF inverse pole figure
LPCVD low-pressure chemical vapour deposition
MUD multiples of uniform pole density
ODF orientation distribution function
PECVD plasma-enhanced CVD
PVD physical vapour deposition
SAD selected area diffraction
SE secondary electrons
SEM scanning electron microscopy
STEM scanning transmission electron microscopy
TEM transmission electron microscopy
TKD transmission Kikuchi diffraction
WDS wavelength-dispersive spectrometry
XRD x-ray diffraction

Nomenclature

Symbols

a	lattice parameter
Al	aluminium
Ar	argon
As	arsenic
B	boron
C	carbon
Cl	chlorine
Co	cobalt
Cu	copper
C1/2/3	condenser lens 1/2/3
E_A	energy of activation
E_a	evaporation energy
E_d	diffusion energy
E_i	binding energy of a cluster of size i
e^-	electron(s)
g	gaseous
Ga	gallium
ΔG^M	molar Gibbs energy
H	hydrogen
L	characteristic length
N	nitrogen
$\vec{n}$	sample normal
n_∞	concentration
O	oxygen
Pt	platinum

R	gas constant
R	rate of arrival
s	solid
T	temperature
T_S	substrate temperature
Ti	titanium
W	tungsten
x	aluminium nitride fraction
X	composition
Z	mean atomic number
α	tilt angle along the holder axis
β	tilt angle along the axis in the sample plane and perpendicular to the holder axis
δ	boundary layer thickness
$\overline{\delta}$	strain
λ	lamella periodicity
σ	surface energy
θ	angle of the feature to the normal of the shear stress plane after deformation
θ_{B}	Bragg angle
ζ	angle of the feature to the normal of the shear stress plane before deformation

Contents

List of Figures

List of Tables

1 Introduction

1.1 Background

In the present work, the microstructure of wear-resistant TiAlN coatings that are applied on cutting tools for metal machining is investigated. In general, metal cutting includes processes where a chip is formed, for example turning and milling, that produce workpieces with a defined geometry fulfilling specific quality features. For this, a cutting tool with at least one cutting edge is applied. The cutting edge comprises two surfaces, the rake and the flank face, which meet to form the cutting edge under the wedge angle [2]. The rake face is the surface where the chip traverses during the cutting process, while the flank face is orientated towards the cut surface. The surface quality of the workpiece and the dimensional accuracy during machining can be improved with an accurate geometry of the cutting tool, illustrating the importance of the characteristics and quality of the used cutting tool. Two important properties of relevant cutting tool materials are hardness and wear resistance, as well as toughness. Figure 1.1 shows the hardness versus the toughness of typical cutting tool materials, illustrating that optimal hardness and toughness cannot be achieved simultaneously, as the toughness decreases with increasing hardness and wear resistance [2]. Therefore, the cutting tool material has to be chosen depending on the application and research in this area focuses on the optimization of the material's properties in terms of hardness and toughness. Data from 2014 shows that the majority of the cutting tools on the market are made of cemented carbide (53%) and high-speed steel (20%) [3]. While high-speed steels show favourable toughness values, cemented carbides have a significantly higher hardness [2]. Cemented carbides are composite materials, where carbides of transition metals such as W are embedded in a soft binder phase, typically Co. They are mostly manufactured by the powder metallurgical processes of pressing and sintering and their specific properties can be adapted by tuning the carbide to binder phase ratios.

During the machining of workpieces, the cutting tools are subject to high temperatures and pressure. Furthermore, increasing requirements on productivity, cost reduction and sustainability result in the need for increased cutting speeds and feed rates, as well as minimization of the usage of lubricants [5, 6, 7, 8, 9]. The introduction of new workpiece materials presents unique challenges to the development of cutting tools [5, 3, 10]. In order to handle these demands, there is a trend towards higher cutting temperatures [5]. A summary of failure mechanisms depending on cutting temperature is shown in Figure 1.2 [2, 5]. With increasing cutting temper-

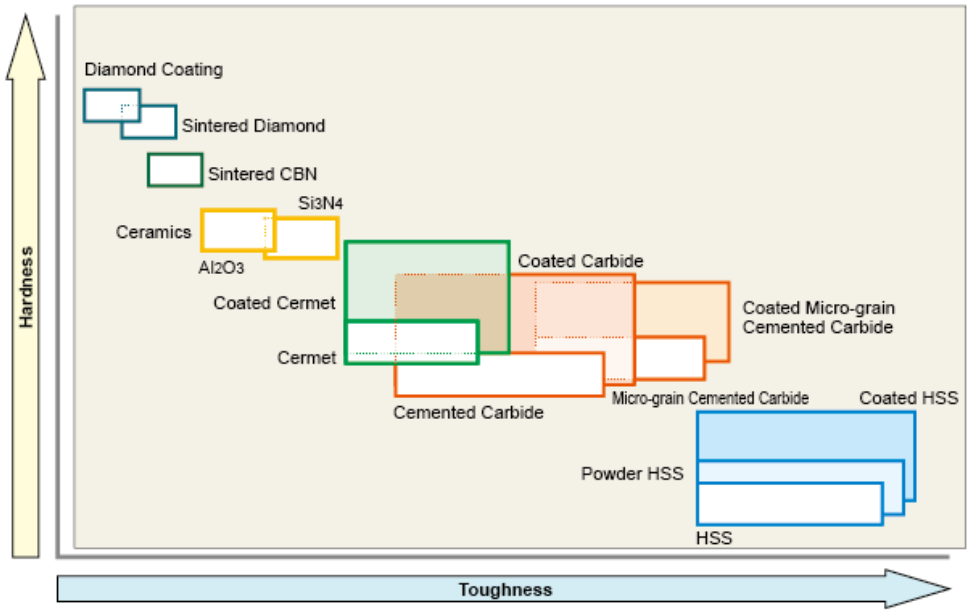

Figure 1.1: Hardness versus toughness of typical cutting tool materials. Taken from [4].

ature, the role of failure due to adhesion becomes less critical, while failure due to diffusion and oxidation is introduced by thermal activation [2]. Therefore, oxidation and corrosion resistance as well as thermal stability gain importance in addition to wear resistance, low friction coefficients, high fracture toughness and hardness [5, 6]. Furthermore, failure mainly concerns the interface of the cutting tool surface and the workpiece. As a consequence, coatings are generally deposited on the cutting tool material to enable the independent tailoring of volume and surface properties [5, 11, 12]. The improvement of the properties in comparison to the uncoated cutting tool is indicated in Figure 1.1.

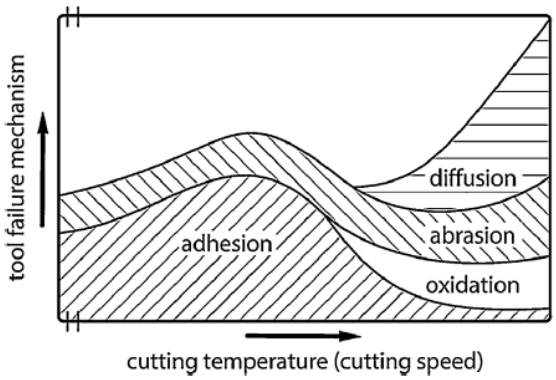

Figure 1.2: Failure mechanisms of cutting tools in dependence of cutting temperature. Taken from [5], reproduced by [5] from [2].

1.2 TiAlN coatings

TiAlN coatings exhibit good chemical stability, oxidation resistance, hardness at room temperature and hot hardness, as well as a relatively low friction coefficient and wear rate [13, 14, 15]. The first commercially available TiAlN coated cutting tool was introduced in 1989 and has been one of the most important coatings deposited by physical vapour deposition (PVD) since then [5, 16]. In comparison to other Ti-based coatings, TiAlN has a lower friction coefficient than TiN as well as a higher corrosion resistance and hot hardness [6, 15, 17]. TiAlN shows a lower wear rate in comparison to TiCN, despite having a higher friction coefficient [6, 15]. In addition, the hot hardness of TiAlN is higher than that of both TiN and TiCN [14]. Overall, the suitable properties of TiAlN coatings, such as hardness, oxidation and corrosion resistance, can be improved even further by an increased Al content [6, 15, 17, 18]. However, the Al content in PVD TiAlN coatings is limited to a maximum of about 67 at.% [5, 6, 19]. TiAlN coatings prepared by low-pressure chemical vapour deposition (LPCVD) have pushed this limit and allow a higher Al/Ti ratio [18, 20, 21]. As a result, TiAlN coatings prepared by LPCVD show better oxidation and corrosion resistance in comparison to those prepared by PVD [6, 15, 17, 18]. Additionally, the desired cubic phase of TiAlN, which exists as a supersaturated solid solution in chemical vapour deposition (CVD) and PVD TiAlN coatings, is metastable [22]. TiAlN coatings prepared by LPCVD showed higher thermal stability than those prepared by PVD despite higher Al contents [20, 21]. It has been speculated, that a nano-lamellar arrangement of Ti- and Al-rich regions in TiAlN coatings deposited by LPCVD contribute to their improved thermal stability [23]. Despite existing intensive research on the growth of TiAlN coatings by LPCVD and the evolving microstructure, the growth mechanisms and detailed microstructural characteristics are not fully understood and are subject to scientific debate.

1.3 Post-treatment

In addition to tuning the microstructure by adapting the deposition parameters to optimize the coating properties and resulting performance, post-treatment can be performed on the coatings to further enhance the material properties. Blasting of cutting tool coatings deposited by CVD and PVD, particularly Al_2O_3, has shown to have the ability to transform coatings from a state of residual tensile stress to residual compressive stress [24, 25, 26, 27, 28]. This change of residual stress state can lead to the closing of thermal cracks [25, 28]. Further, blasting post-treatment after coating deposition has been shown to increase coating hardness and decrease surface roughness which can positively influence other relevant properties, such as the friction coefficient and adhesion. This leads to better wear resistance and overall improved tool life [24, 26, 28, 29]. In addition, Tanaka et al. [30] reported that the fracture toughness of PVD TiAlN coatings could be increased by blasting post-treatment. Blast-treatment can be performed either dry or wet, where the abrasive particles are accelerated towards the cutting tool insert either by high-pressure air or water,

respectively [29]. Bouzakis et al. [31] concluded that wet-blasting post-treatment is more suitable for increasing tool life from wet- and dry-blasting experiments on PVD TiAlN coatings. While the effect of blast-treatment on the stress state and the consequent positive impacts on the coating properties has received attention in numerous scientific publications, there remains a relative sparsity of investigations unveiling the underlying microstructural changes.

1.4 Aim

This thesis contributes to the Vinnova research project "High-performance nano-structured CVD TiAlN coated cutting tools for difficult-to-cut materials" involving Chalmers University of Technology, Walter, Alleima, Seco Tools and Sandvik Coromant. The aim of the overarching project is to explore the possibility of tailoring the nano-structure of wear-resistant TiAlN coatings to improve their protective properties, making them a suitable choice when machining materials that are hard to machine today. The thesis contributes to the work packages of the Vinnova project concerning the revelation of the microstructure of the CVD TiAlN coatings. Attention is given to the detailed microstructure of LPCVD TiAlN coatings with three different periodicities of nano-lamellae of Ti- and Al-rich regions and the influence of wet-blasting post-treatment. Characterization is done by scanning electron microscopy (SEM), scanning transmission electron microscopy (STEM), energy-dispersive x-ray spectroscopy (EDS) and transmission Kikuchi diffraction (TKD). In particular, the observed surface morphology is connected to the grain growth, where surface kinetics, surface energies, texture and the development of facets play important roles. The effect of blast-treatment on the surface and coating morphology reveals information on how the material is influenced by external stresses on a microstructural level, where a possible influence of the varying nano-lamella periodicity is considered.

2

Chemical Vapour Deposition

In chemical vapour deposition, gas phase precursors react to form a solid film on a substrate [32, 33]. Film thicknesses from atomic layers deposited by specialized CVD techniques up to more than 100 µm can be achieved. The reaction of the precursors can occur homogeneously in the gas phase in the reactor's reaction zone to form powder particles, or heterogeneously on the substrate and reactor wall surfaces. The homogeneous reaction causes porosity and inhomogeneities in morphology and film thickness, and is therefore undesired. The reactions occurring in the reactor in the gas phase and at the surface of the substrate are of great complexity and mostly not fully understood. However, an overall reaction scheme can summarize the chemical reactions taking place, while disregarding the complexity. Most reactions that are applied to form films by CVD are thermodynamically endothermic and possess a kinetic energy barrier which must be overcome to activate the process. Consequently, energy has to be supplied during CVD to facilitate the desired reactions.

2.1 The Chemical Vapour Deposition Process

A reactor for CVD includes the following three major parts: Firstly, a gas handling system which controls the flow of the gaseous precursors to the reaction zone [32]. Secondly, a reaction zone containing the substrate holders and substrate, often enclosed by a furnace. And third, an exhaust system in conjunction with a vacuum pump in low-pressure reactors, to remove waste products. A waste treatment facility including monitoring devices is attached if necessary.

Conventionally, the energy necessary to facilitate the chemical reactions and to overcome the kinetic energy of activation is provided by thermal energy [32, 33]. In general, hot-wall and cold-wall reactors are distinguished, where in a hot-wall reactor the whole reactor is heated and acts as a furnace, while only the substrate is heated in a cold-wall reactor. The exclusive heating of the substrate presents the advantage of suppressing the homogeneous reaction in the gas phase and the reaction at cold reactor walls, leading to the favouring of the heterogeneous reaction at the surface of the substrate. However, it presents challenges in the control of the flow field and homogeneous heating of the substrate. Commonly, the substrate or substrate holder is heated by direct resistance heating, radio frequency induction or radiation heating (thermal or photo radiation). However, the heating of the substrate limits the choice of substrates to those that are not temperature sensitive and damaged during heating. As a consequence, alternative paths of supplying energy

to the system to accommodate the desired reaction during CVD have been applied. For example, plasma-enhanced CVD (PECVD) initiates a homogeneous reaction to form active intermediates that subsequently react heterogeneously at the substrate surface to form a solid layer. Additional ways of supplying the required energy include high-energy photons (photo-assisted CVD).

A crucial parameter for the growth of films by CVD is the flow of the gaseous precursors [32]. The flow conditions near the substrate surface are schematically shown in Figure 2.1. When the gaseous precursors reach the substrate, a gradient in velocity is present at the substrate surface, forming a stagnant boundary layer. The boundary layer thickness varies across the substrate surface, and the degree of variation influences the uniformity of the resulting solid layer. In addition to the velocity of the precursor gas, the concentration gradient influences the diffusional flux of precursors into the stagnant layer and by that the deposition. Generally, an increase in bulk velocity and a decrease in reactor dimensions result in a thinner boundary layer. Furthermore, the side of the substrate closer to the gas source is exposed to a higher precursor concentration and a lower boundary layer thickness, as shown in Figure 2.1, leading to an increased deposition rate. To solve the issue of varying deposition across a substrate surface, the substrates can be rotated at a rotation speed adjusted to the deposition rate to ensure uniform deposition [32].

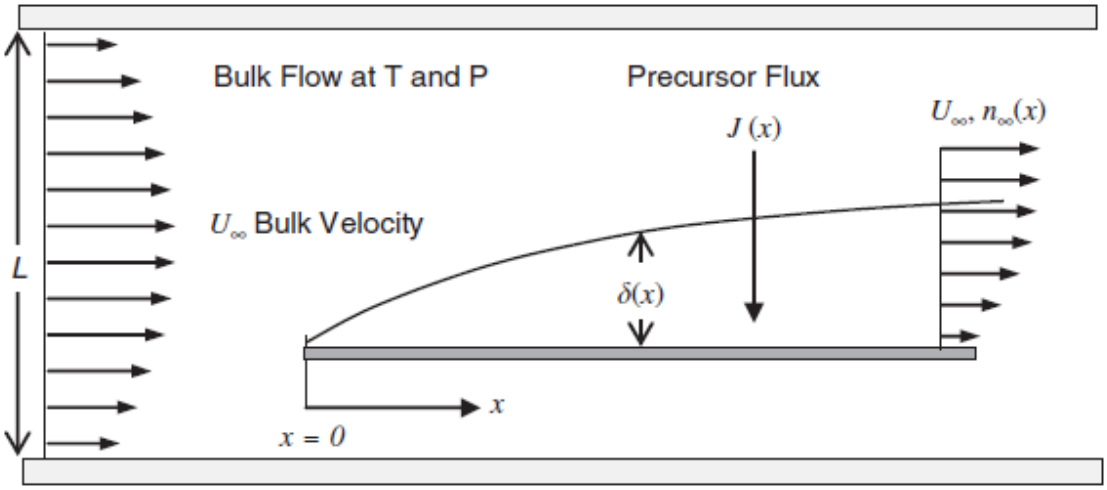

Figure 2.1: Flow conditions near the substrate surface. L describes a characteristic length determined by the hydraulic diameter (tube diameter in the case of a flow in a tube). $n_\infty(x)$ is the concentration and $\delta(x)$ the boundary layer thickness as a function of the position x on the substrate. Taken from [32].

Suitable precursors for CVD need to have sufficient volatility [32]. Either, they are gaseous at the handling conditions, as determined by their phase diagram, or if they are liquid or even solid the volatility has to be enhanced. Additionally, precursors have to show optimum stability, with a favourable range between evaporation and decomposition, high chemical purity and decomposition that yields deposition without impurities. The compatibility of co-precursors also needs to be ensured. Further requirements include sufficient stability for a long shelf-life, preferably low cost and

a low hazard risk and toxicity.

2.2 Growth and Morphology of Coatings

Deposition parameters, including substrate temperature, reactor pressure, precursor partial pressures, chemistry of precursors, arrival rate at the substrate surface and energy of the species, play a crucial role in the growth and resulting morphology of CVD coatings [32, 33]. Figure 2.2 shows the logarithm of the growth rate as a function of the reciprocal growth temperature during the deposition by CVD of GaAs as an illustrative example. Three regions can be distinguished: At lower temperatures, the deposition is controlled by surface kinetics. In this region, the growth rate follows the Arrhenius equation and therefore increases exponentially with the substrate temperature, as shown in Equation 2.1 where E_A is the energy of activation, T the temperature and R the gas constant. At more elevated temperatures, a second region can be distinguished in Figure 2.2 that is nearly independent of temperature. In the second region, the growth rate is determined by mass transport or diffusion through the boundary layer. In the third region that is identified in Figure 2.2, desorption of precursors from the substrate surface and side reactions in the gas phase result in a decreasing growth rate. The transition between one region to another seems sharp in Figure 2.2 due to the logarithmic plot of the growth rate. In a linear plot, the transitions appear more gradual, showing a region in which the difference in the rate of each mechanism is not significant enough for one to prevail. The positioning of the boundaries between the regions will depend on the precursor, its viscosity, reaction and partial pressure, as well as the bulk flow velocity.

$$\text{growth rate} \propto \exp\left(\frac{E_A}{\mathrm{R}T}\right) \tag{2.1}$$

Figure 2.3 illustrates the precursor processes during reaction, adsorption, nucleation and growth on surfaces. Those processes marked with an orange colour include parameters that influence the mass transport/diffusion of precursor molecules to the surface, while those marked with a blue colour include processes that are part of the kinetics of the surface reaction. As discussed in the previous paragraph, there are parameter windows where one or the other limits the growth rate. Precursor molecules or resulting species that are adsorbed to the surface may diffuse across the surface until they nucleate to clusters, are captured by an existing cluster or imperfections of the surface, or re-evaporate [35, 32, 36]. These processes have characteristic times that are determined by their activation energy and a frequency factor, in the case of thermally activated processes such as evaporation, diffusion or cluster formation [36]. The major independent experimental parameters that govern adsorption, nucleation and growth processes are the rate of arrival R and the substrate temperature T_S. Other parameters such as the evaporation E_a and diffusion energy E_d and the binding energy of a cluster of size i E_i are material dependent. During CVD, the chemical reaction occurring at the substrate surface introduces further complexity as well as material and precursor-dependent parameters to the processes [32]. Film formation proceeds through nucleation and growth, where generally three different growth modes are differentiated: island growth, layer growth

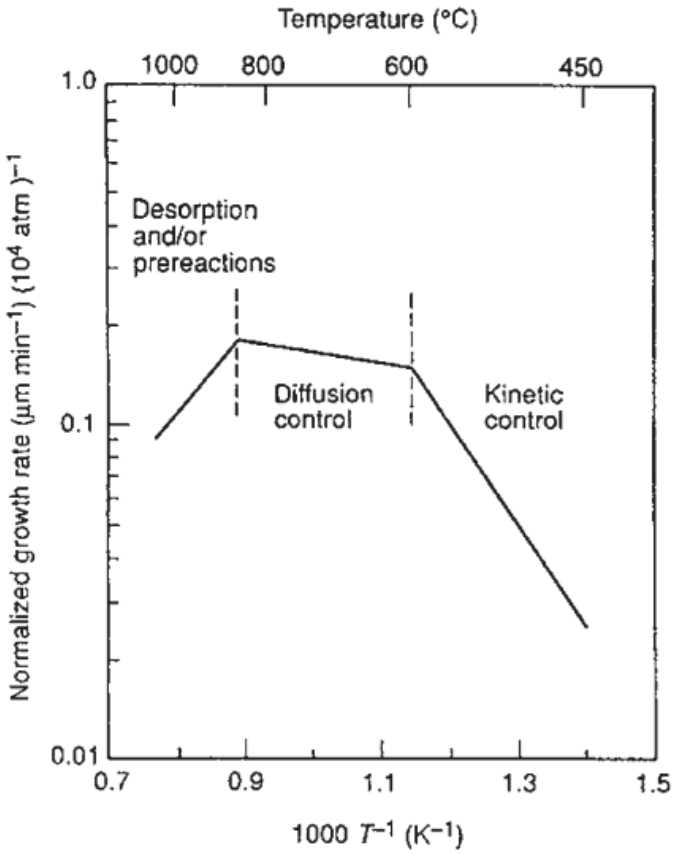

Figure 2.2: Logarithm of the growth rate as a function of reciprocal temperature for CVD of GaAs. Taken from [32], reproduced by [32] from [34].

and an intermediate between the two, where initial layer growth transforms into the formation of islands [36]. By coalescence and further growth, a coating of desired thickness is formed. Overall, crystal nucleation and growth is a non-equilibrium process, as there would be no net growth in equilibrium. Therefore, vapour deposition of films will not necessarily lead to the thermodynamically most stable state, but instead to a kinetically determined state. Nevertheless, there are some aspects for which a local equilibrium can be considered, for example, the shape of the crystals [36]. According to thermodynamics, the most stable crystal shape is the Wulff shape, which is determined by the minimization of surface energies. Facets with high surface energy grow faster, consequently, their area is reduced, while the facets with low surface energy are revealed. In the case of crystal growth on a surface, additional arguments have to be made that take into account the surface energy between the crystal and substrate. However, in many cases, the equilibrium shape determined by the Wulff shape is not maintained due to insufficient speed of the surface diffusion relative to the other kinetic processes during nucleation and growth. Additionally, the time needed to achieve equilibrium is a strong function of the crystallite size and is consequently frequently not achieved as the crystallite coalesces and grows. Commonly, the crystals are more facetted than the equilibrium shape due to slower growth of the surfaces with comparably low surface energy than at the edges.

In many cases, films deposited by vapour deposition show a preferred direction of growth (preferred texture). Two fundamentally different mechanisms for the development of texture in a coating grown by vapour deposition are observed [37]. Firstly, texture evolving from nuclei with a preferred orientation, for example, due to epitaxial growth on a crystalline surface. In this case, the misfit of the different lattice constants is minimized by a specific orientation relationship to the crystal on which the layer is grown [38]. To facilitate epitaxy during growth by CVD, low growth rates and high temperatures are necessary to provide fast surface diffusion relative to the arrival of new species to the surface [32]. Secondly, a texture may evolve from randomly orientated nuclei due to a faster vertical growth rate of specific crystallographic orientations. In the competitive growth of differently-orientated grains in a polycrystalline film, those grains with a faster vertical growth rate will undergo "evolutionary selection" [37]. While the degree of texture is constant in epitaxial growth, it increases with the film thickness in the case of evolutionary selection.

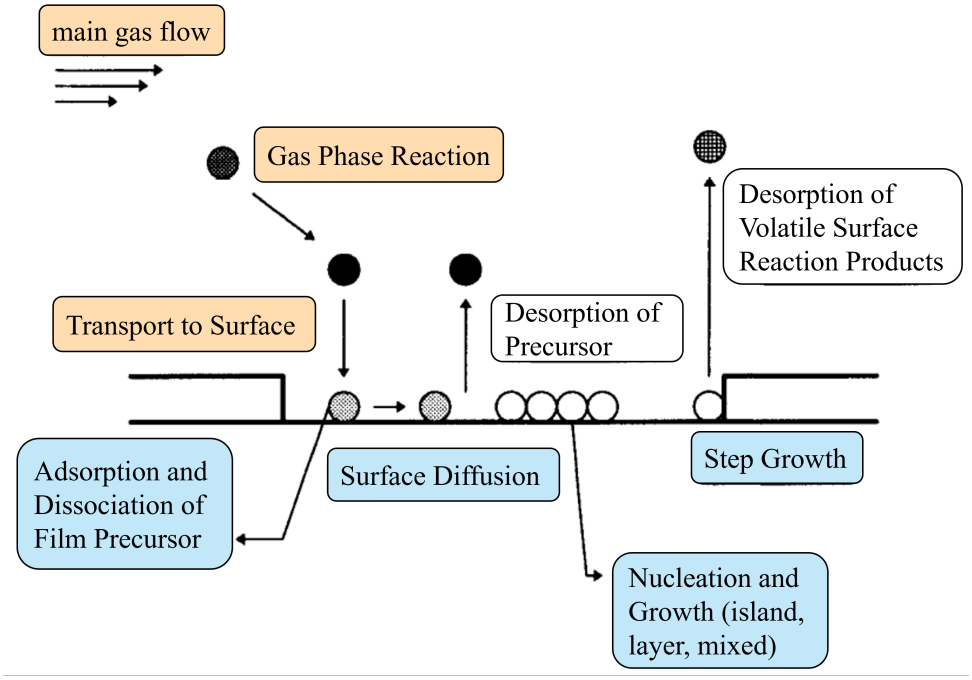

Figure 2.3: Transport and reaction processes of precursors during nucleation and growth by CVD on surfaces. Adapted from [32]. Orange-marked processes include parameters that influence the mass transport/diffusion of precursor molecules to the surface. Blue-marked processes contribute to the kinetics of the surface reaction.

2.3 Low-Pressure Chemical Vapour Deposition

LPCVD is conducted below atmospheric pressure, where convection is forced by pumping at the outlet [39]. The gas flow is more random in nature as a consequence of increasingly low pressures [32]. Additionally, the diffusivity of the precursor gas

is proportional to the temperature and the inverse of the pressure. As discussed in the previous section, this will influence the growth and resulting morphology of the coating. The low pressure in the LPCVD process effectively suppresses homogeneous reactions of precursors in the gas phase, the reactions are subsequently induced on the substrate by elevated temperatures [39]. This is particularly relevant when highly reactive precursors are required and leads to dense coatings with superior homogeneity and better step coverage compared to PECVD processes [40]. As shown in Figure 2.2 and discussed in section 2.2, the growth is limited by surface kinetics at relatively low temperatures and by mass transport at higher temperatures depending on the precursor reactions [32]. For instance, the kinetically controlled growth enabled by low process pressures in LPCVD is utilized for semiconductor films to achieve highly uniform, epitaxially grown coatings [35].

2.4 Comparison to Physical Vapour Deposition

CVD and PVD are two of the major methods of depositing films onto substrates [41]. In comparison to CVD, where coatings are formed by chemical reactions at the substrate surface, PVD coatings are deposited by condensation of vapour on a substrate. PVD process are typically distinguished by the method of vaporization of solid material such as thermal evaporation, arc vapour deposition, ion plating and sputtering, as well as their variants, yielding atoms, molecules or clusters thereof, which are subsequently transported to the substrate where they condensate to form a film. Similarities in film deposition by CVD and PVD can be found in the mechanisms of nucleation and growth, however, there are fundamental differences due to additional thermodynamic and kinetic factors from the chemical reactions in CVD. Furthermore, important experimental parameters for film deposition such as deposition temperature and deposition rate differ depending on the specific process and process conditions. Characteristics of both processes, PVD and CVD, are summarized in Table 2.1.

Table 2.1: Comparison of CVD and PVD process characteristics.

CVD	**PVD**
simple and complex compounds, co-deposition and multilayers possible [41, 32, 42]	metals and alloys, simple compounds (oxides, nitrides, etc.) can be fabricated for example by introducing reactive gases such as O_2 or N_2, possible to deposit multilayers and graded composition deposits [41, 43]
precursors liquid or gaseous, toxic side-products might be produced that have to be handled [32, 42]	precursors solid, addition of gas precursors (e.g. O_2, N_2) possible, no toxic or environment-damaging side-products [43, 42]
coating thicknesses from atomic layers to several hundred micrometres, high deposition rate [32, 41]	from a few nanometres to micrometres [41]
high temperature required unless the energy for activating the reaction is supplied by other methods (plasma, radiation, etc.) [32]	low process temperatures enable the use of temperature-sensitive substrates [43]
uniform deposition on complex substrate geometries possible [32, 42]	straight trajectories of vaporized atoms and molecules (line-of-site process) leading to shadowing and non-uniform coatings on complex geometries [41, 42]
typically columnar grains with larger grain size [44]	typically columnar grains with smaller grain size [45]
roughness slightly higher than coated surfaces [45, 46]	surface roughness reflects roughness of coated surface [45]
residual tensile stress due to deposition at elevated temperatures and subsequent cooling [45]	residual compressive stress [45]

2.5 Applications for Hard Coatings

As introduced in chapter 1, cutting tools are frequently coated with hard coatings to improve the wear behaviour, especially abrasion and adhesion, as well as diffusion, oxidation and corrosion resistance [5]. Product innovations in this field are mostly accounted for by new or improved material systems [10]. In general, PVD coatings are preferred in milling applications due to their residual compressive stresses and sharper cutting edges, while CVD coatings are prone to cracking in this repetitively

interrupted process that leads to abrupt changes in forces and temperature. CVD coatings exhibit superior behaviour in turning, where the cutting force is constant [5]. Typical hard coatings deposited by CVD include Al_2O_3 and diamond. In 2014, Dedalus Consulting predicted a rising market share of CVD coatings, primarily as a result of further development of diamond coatings, taking the place of the expensive super-hard cutting materials such as polycrystalline cubic BN (PcBN) and polycrystalline diamond (PCD) [3]. Further development of CVD coating processes continuously enables the deposition of new materials and multilayers, as well as control of crucial coating characteristics, such as crystal structure, grain size and morphology [5]. For instance, the deposition of metastable ternary nitrides (TiAlN) with cubic crystal structure, which was previously confined to PVD techniques, has been implemented by LPCVD [18, 20, 21].

3

TiAlN Coatings

In this work, TiAlN coatings prepared by LPCVD with high overall Al contents (up to metal contents of roughly 86 at.%) and the effect of post-treatment on the microstructure are investigated. In order to understand the findings during the analysis, a basis of known aspects of TiAlN coatings is required. The following sections discuss the phases found in TiAlN coatings, their crystal structure and thermodynamics. Specifically, the previously investigated microstructure of TiAlN coatings prepared by LPCVD is presented. Further, the effect of post-treatments on TiAlN hard coatings is discussed.

3.1 Phases - Crystal Structure and Thermodynamics

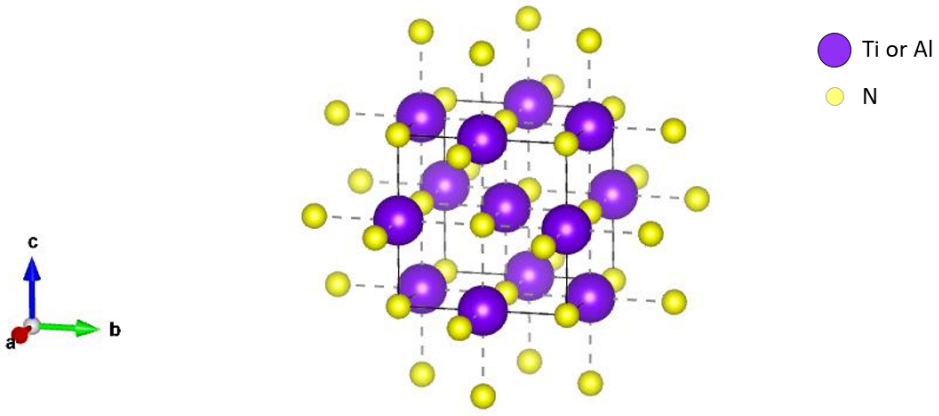

Figure 3.1: Rocksalt-type crystal structure of fcc TiAlN as a solid solution [22].

When assessing the occurring phases in ternary mixtures of Al, Ti and N it is helpful to look at the pseudo-binary behaviour of TiN and AlN. In equilibrium conditions, TiN with rocksalt structure and wurtzite AlN show no miscibility in the solid state [22] and cubic Al-rich phases are unstable [6]. However, metastable TiAlN coatings can be fabricated by PVD and CVD with cubic or hexagonal crystal structure [22]. The fabricated cubic TiAlN layers have face centred cubic (fcc) structure and exist as a supersaturated solid solution [22]. Here, Al atoms substitute Ti

atoms in the rocksalt structure of TiN, as illustrated in Figure 3.1. The lattice parameter of fcc TiAlN can be estimated by applying Vegard's law to the pseudo-binary of TiN and AlN [47, 48]. Vegard's law is an empirical rule suggesting a linear relation between the lattice constant of an alloy and the concentrations of the constituent elements at a constant temperature [49]. Experimentally, a lattice parameter $a = 4.241\,73\,\text{Å}$ was found for cubic TiN and filed in PDF 00-038-1420 [50] and $a = 4.0450\,\text{Å}$ for cubic AlN (PDF 01-077-6808) [50]. Therefore, the lattice parameter of a solid solution of the two can be determined by Equation 3.1 which is visualized in Figure 3.2, predicting a decrease of the lattice parameter with increasing Al fraction x [19]. Based on first principal calculations by Alling et al. [47] there is a slight deviation from linear behaviour above Al fractions of $x = 0.70$ in the case of TiAlN. Endler et al. [48] have summarized lattice parameters determined from TiAlN coatings deposited by PVD and corrected for prevailing compressive stresses and found a slight convex deviation from Vegard's law. However, the lattice parameter determined by Endler et al. [48] from fcc TiAlN prepared by CVD at an Al fraction of $x = 0.87$ (determined by EDS and wavelength-dispersive spectrometry (WDS)) fits well with the prediction by Vegard's law.

$$a(\text{TiAlN}) = 4.24173 - 0.1967x \tag{3.1}$$

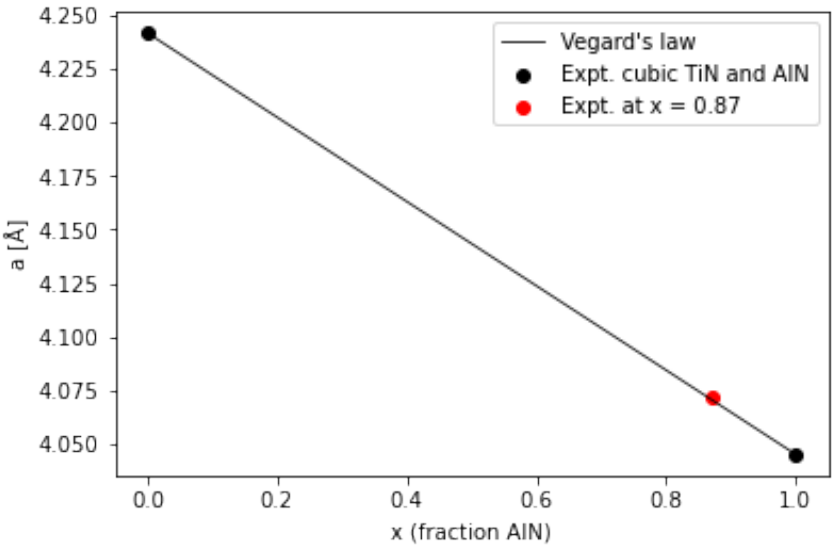

Figure 3.2: Vegard's law applied to a pseudo-binary solution of TiN and AlN. Lattice parameters for TiN and AlN are taken from PDF 00-038-1420 and PDF 01-077-6808 [50], respectively. Experimental data by Endler et al. [48] from CVD fcc TiAlN fits well with the prediction by Vegard's law.

Figure 3.3 shows the pseudo-binary theoretical phase diagram of TiN and AlN for the PVD TiAlN system with data taken from [51, 22]. It is dominated by a large miscibility gap over the range of compositions, where the decomposition of TiAlN is thermodynamically favoured. The miscibility gap is not symmetrical with respect to composition and shows a larger phase stability domain of TiAlN at low AlN fraction x [22, 51]. This is understandable when taking into account that TiN is cubic while

AlN is hexagonal under ambient conditions. Additionally, the miscibility gap is divided into a binodal and spinodal region. At the spinodal line, the second derivative of the Gibbs energy with respect to the composition is zero ($\partial^2 \Delta G^M / \partial X^2 = 0$) [52]. Within the region of spinodal decomposition, this derivative is negative, while it is positive within the binodal region. This influences the modes of phase transformation. Spinodal decomposition occurs spontaneously and typically results in a periodic arrangement of the decomposition products, while binodal transformation occurs through nucleation and growth [53, 54]. Furthermore, metastable TiAlN coatings as supersaturated solid solutions generally can be fabricated with both rocksalt structure or wurtzite structure [22]. Experimental investigations of PVD coatings, as well as theoretical calculations, reveal a metastable phase boundary between rocksalt and wurtzite TiAlN solid solution at roughly 0.7 mol fraction of AlN which is indicated in the phase diagram in Figure 3.3 [6, 22, 47, 55]. For cutting tool applications, a high Al content in combination with rocksalt structure in TiAlN is desirable, considering the enhanced oxidation and mechanical resistance [5, 6, 18, 19, 22]. The introduction of LPCVD for the deposition of TiAlN coatings has made the fabrication of fcc TiAlN coatings with high contents of Al above the metastable phase boundary at 0.7 mol fraction of AlN possible, leading the way to improved coatings TiAlN for cutting tool applications. These coatings are presented in section 3.2.

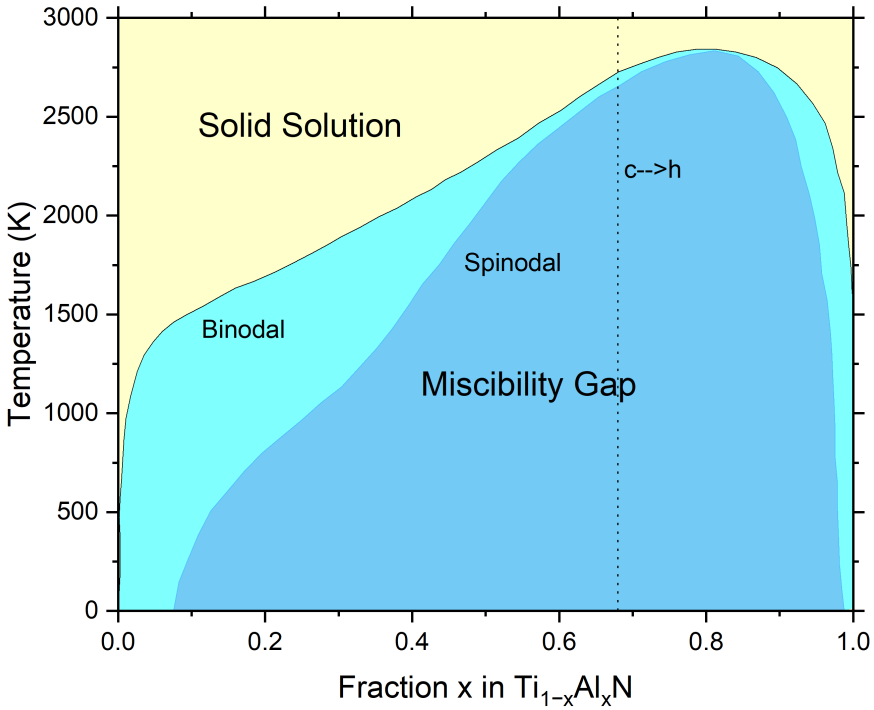

Figure 3.3: Phase diagram of $Ti_{1-x}Al_xN$. Data taken from [22, 51]. The blue-coloured area is the miscibility gap, where spinodal decomposition takes place in the slightly darker blue-coloured area and binodal decomposition in the turquoise-coloured area. The dotted line represents the approximate transition composition of the formation of hexagonal or cubic metastable TiAlN solid solution in PVD coatings.

3.2 TiAlN Coatings Prepared by Low-Pressure Chemical Vapour Deposition

In search of the possibility to deposit TiAlN coatings with Al contents above the metastable phase boundary at 0.7 mol fraction of AlN of PVD TiAlN coatings, LPCVD processes have been developed. The precursors typically used in this process are $TiCl_4$, $AlCl_3$, NH_3 and H_2, the overall reaction scheme is as follows [56]:

$$(1-x)\,TiCl_4\,(g) + x\,AlCl_3\,(g) + NH_3\,(g) + (1-x)/2\,H_2\,(g) \longrightarrow Ti_{1-x}Al_xN\,(s) + (1-x)\,HCl\,(g).$$

As discussed generally in chapter 2, reactor and substrate temperature as well as the flow and diffusivity of precursor gases are crucial parameters in the deposition of films by CVD that will govern growth kinetics and thereby the prevailing phases as well as the resulting coating morphology. Because of the metastability of fcc TiAlN and its spinodal decomposition at elevated temperature, the deposition tem-

peratures during the LPCVD process are relatively low (in the range of 650 °C to 900 °C) which leads to the necessity of reactive precursor molecules such as NH_3 instead of N_2 [20, 23, 56]. In addition, N_2 and Ar can be employed as carrier gases. Typically, cylindrical hot-wall type reactors are used for deposition and the precursor gases are supplied by a rotating central pipe [20, 56], pressures range between 5 mbar and 100 mbar [20, 56, 23]. Adsorption energies of the precursors calculated by density functional theory (DFT) reveal remarkably lower adsorption energies of Ti chlorides than of Al chlorides on the phases of the growing TiAlN film [18]. As a consequence, Ti deposition is assumed to be limited by mass transport, while Al deposition is limited by the surface reaction kinetics at the given process temperatures in LPCVD. The limitation of the Al deposition by surface reaction kinetics reveals an upper limit of gas flow velocity in the deposition of TiAlN coatings with high Al content, while the limitation of Ti deposition by mass transport reveals a lower limit of gas flow velocity, generating a window of optimum gas flow velocity.

It is possible to prepare TiAlN coatings by LPCVD with AlN fractions between 0.8 and 0.9 that are largely cubic, with small amounts of hexagonal AlN forming at grain boundaries and domains within TiAlN grains, however, in very small amounts that are only revealed in transmission electron microscopy (TEM) investigations and generally not in x-ray diffraction (XRD) data [18, 20, 23]. The grain morphology of the fcc TiAlN coatings is frequently columnar and some of the coatings show a pyramidal surface morphology, as presented in Figure 3.4a and Figure 3.4b [56, 23, 20, 21]. Commonly the coatings show a pronounced (111) texture [56, 23, 21], though (100), (110), (211) and (311) textures, as well as random orientations have also been reported [57, 58, 59, 60]. The (111) texture in combination with the threefold symmetry of the pyramidal surface morphology reveals that the facets of the pyramids are {100} planes [1]. According to DFT calculations, the {100} planes of TiAlN have significantly lower surface energy with little concentration dependence in comparison to the {110} and {111} planes [61]. The formation of (111) texture can therefore be explained by "evolutionary selection" (discussed in section 2.2) [1].

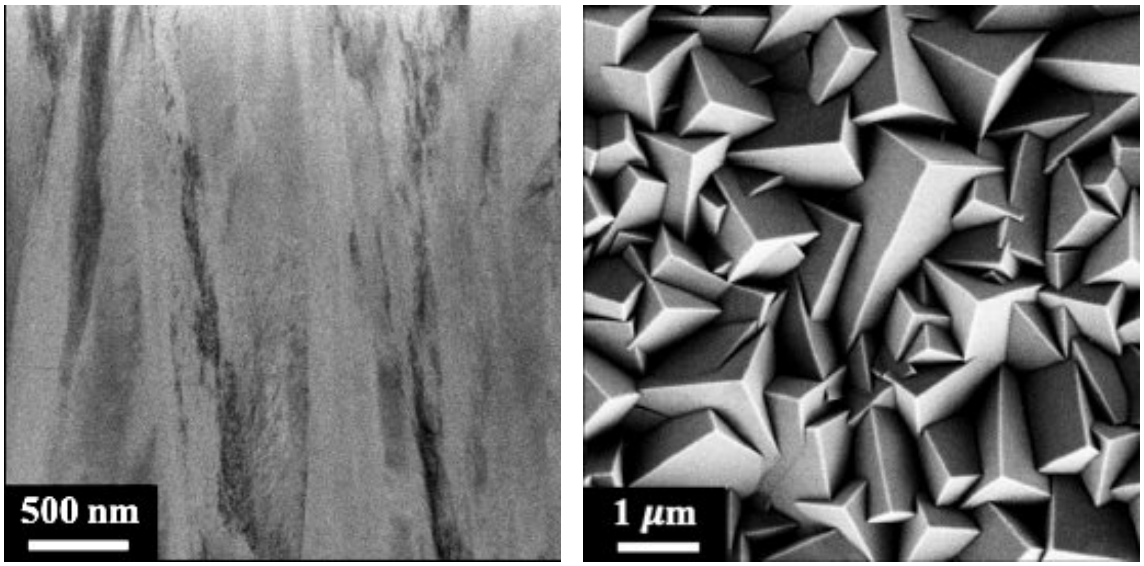

(a) (b)

Figure 3.4: (a) Columnar grain morphology of TiAlN coatings prepared by LPCVD imaged by STEM BF. (b) SEM image of the pyramidal surface morphology of TiAlN coatings prepared by LPCVD. Images taken from [1].

Within the columnar grains, the Ti and Al concentration is not constant but varies periodically along the <100> direction forming Ti- and Al-rich nano-lamellae, as shown in Figure 3.5 where an EDS linescan reveals the varying composition [1, 23, 21, 60, 62]. The nanolamellae appear with different periodicities but with consistently thinner Ti-rich lamellae and in comparison thicker Al-rich lamellae which are continuous across grains. The nanolamellae grow epitaxially with a cube-on-cube relationship between Ti- and Al-rich fcc solid solutions, as displayed in Figure 3.6 where the fast Fourier transform (FFT) reveals the orientations. The periodical variation of Ti and Al content in the growth direction has been connected to the rotational precursor gas supply in the LPCVD process by Qiu et al. [1]. During the rotation of the precursor gas supply, the gas flow will be orientated directly towards each sample for short amounts of time. On this occasion, the local gas flow velocity is very high and therefore also the mass transport, leading to an increased deposition rate of Ti that is limited by mass transport. When the gas beam rotates away, the local gas flow velocity is reduced, the deposition of Ti is suppressed and an Al-rich layer is formed as the deposition of Al is not influenced by the mass transport but limited by the surface reaction kinetics. No matter the rotation speed, the time during which the gas supply is directed at a sample will be shorter than the time it is rotated away from the sample, which explains the consistently lower layer thickness of Ti-rich lamellae compared to the Al-rich lamellae. The connection of the nanolamellae to the rotational precursor gas supply presents the opportunity to tune the periodicity of nanolamellae. In order to achieve distinct nanolamellae, specific deposition parameters are required where too high gas flow rate leads to Ti enrichment and formation of hexagonal AlN, deteriorating the nanolamellar arrangement as well as the columnar grains. The (111) texture is influenced neither by the absence of a nanolamellar structure nor columnar growth. The incoherency of

hexagonal AlN and cubic TiN from decomposition presents a large activation energy barrier and therefore retards its formation, while coherency between the Ti- and Al-rich nanolamellae might contribute to the stability of the cubic crystal structure [1, 23]. Yet, it is not necessary to produce fcc structured TiAlN with AlN contents up to about 90 at.% by LPCVD. It has been reported that the N content varies along with Ti and Al content in the nanolamellae, possibly furthering the coherency between the two [63, 23]. However, contradictory results as to how the N content varies in the nanolamellae have been reported. Qiu et al. [63] performed atom probe tomography (APT) measurements on TiAlN coatings prepared by LPCVD and found higher N content in the Ti lamellae in comparison to the Al lamellae. Their experimental results are confirmed by DFT calculations, which suggest lower formation energy of metal vacancies at low Al content and lower formation energy of N vacancies at high Al content. The high concentration of N vacancies in TiAlN coatings with high Al content might lead to increased thermal stability due to a decreased mixing enthalpy [63, 54]. On the contrary, electron energy loss spectroscopy (EELS) measurements by Zalesak et al. [23] show higher N content in the Al-rich lamellae. It has to be taken into account that quantification of N content by both methods, EELS and APT, is not trivial [63]. Nevertheless, the APT data appears more reliable as it is also confirmed by simulations and the EELS signals by Zalesak et al. [23] were not calibrated using samples with known chemical composition, influencing the accuracy of the quantification [63].

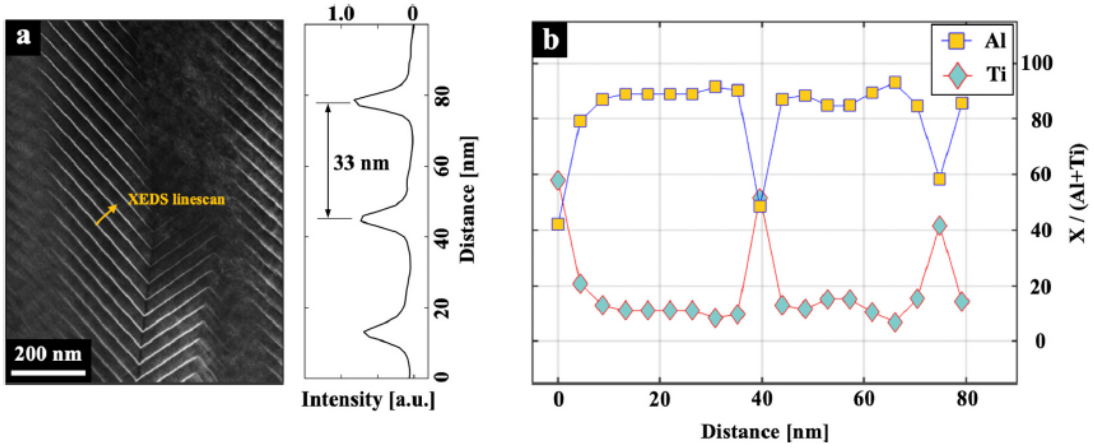

Figure 3.5: Periodical Ti- and Al-rich lamellae imaged by STEM. An EDS linescan reveals Al contents of about 90 at.% in the Al-rich lamellae ($Ti_{0.1}Al_{0.9}N$) and about 50 at.% in the Ti-rich lamellae ($Ti_{0.5}Al_{0.5}N$). Taken from [1].

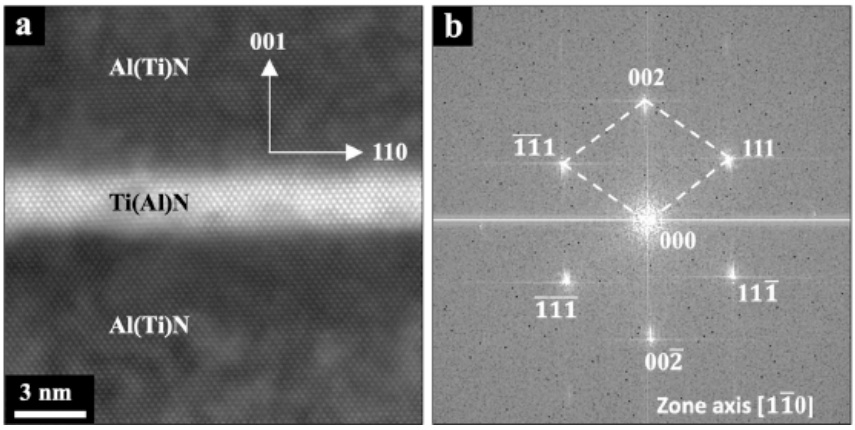

Figure 3.6: Periodical Ti- and Al-rich lamellae imaged by STEM. The FFT reveals the epitaxial growth of the lamellae and their growth along the <100> directions. Taken from [1].

3.3 Post-treatment

Post-treatment can be applied to the deposited TiAlN coatings to tailor the properties for cutting applications by influencing e.g. the present phases, microstructure and stress state. The effect of heat-treatment and blast-treatment is discussed in the following sections.

3.3.1 Heat-treatment

Spinodal decomposition in TiAlN coatings plays an important role in the properties and performance of TiAlN hard coatings for cutting tools [19, 22, 62]. A sequence of transformations is undergone in the process of spinodal decomposition of TiAlN coatings [62, 55]. First, the metastable fcc TiAlN decomposes into cubic TiN and cubic AlN. Subsequently, a transformation of cubic AlN to wurtzite AlN occurs. The coherency of the different decomposition phases plays an important role during this transformation sequence [55]. While the lattice parameters of cubic AlN and TiN show only a small mismatch, the transformation of AlN to the thermodynamically stable hexagonal phase has a large activation energy barrier due to the large volume change.

The first step of spinodal decomposition results in the typical self-organized fine nanostructure, leading to age-hardening by an increase in the wear resistance, hardness, Young's modulus, as well as oxidation resistance of the coating and the formation of a maximum in desired compressive strains in the coating [19, 22, 62]. This transformation occurs roughly between 850 °C and 950 °C in TiAlN coatings prepared by LPCVD with nanolamellar microstructure [64, 21]. In contrast, the cubic to hexagonal transformation of AlN results in a drastic degradation of mechanical properties such as hardness and Young's modulus (over-ageing) [19, 22, 62]. The transformation of fcc AlN to wurtzite AlN occurs at temperatures of roughly 950 °C and 1200 °C in TiAlN coatings prepared by LPCVD with nano-lamellar mi-

crostructure [64, 62, 21]. When the transformation of AlN from cubic to hexagonal symmetry is completed, the composition and lattice parameter of the TiN and AlN phase do not change significantly any more [62]. The cubic TiN globules embedded in a wurtzite AlN matrix (in the case of TiAlN coatings with high Al content) now merely change in shape and size, which does not further affect the strain state significantly. At elevated temperatures below the start of spinodal decomposition, there can be recovery processes within the grains of nanolamellar fcc TiAlN [64, 21]. Tkadletz et al. [62] suggest that the process of spinodal decomposition and its influence on properties and performance is comparable in coatings prepared by both PVD and CVD and differs only in the chemical composition (higher Al content in TiAlN coatings deposited by CVD) and the magnitude of the initial strain (as discussed in Table 2.1).

The notably higher mechanical resistance of coatings with Al content of cubic phase TiAlN coatings with nanolamellar arrangement compared to those with significant amounts of wurtzite AlN is opposed by a significantly increased oxidation resistance of coatings with even higher Al content. The oxidation resistance of TiAlN coatings with $90 - 95$ at.% Al, though including some hexagonal AlN, was found to be $100 - 150$ °C higher than those with Al contents of 80 at.% but with pure fcc TiAlN supersaturated solution [21]. This can be explained by the formation of a denser and thicker Al_2O_3 scale, which is more effective in serving as an oxidation barrier. Though, the oxidation of TiAlN coatings with slightly lower Al content was reported to be less rapid in its evolution [21]. The increased oxidation resistance is however overshadowed by a substantial increase in hardness due to the cubic crystal structure. In a majority of tooling applications, the increased oxidation resistance of TiAlN coatings with Al contents of $90 - 95$ at.% is not required and the lifetimes of the tools are frequently lower than the heat-treatment time [21]. The substantial increase of hardness as a result of the cubic crystal structure is of higher importance for the performance of the hard coatings in the application.

3.3.2 Blast-treatment

The effect of blast-treatment on a material is strongly dependent on the incident angle of the abrasive particles, where sliding, impact and angular jet wear are distinguished and show distinct behaviour [65]. Sliding jet wear describes jet wear at an incident angle of approximately 0°, in which case the wear mechanisms of micro-ploughing and micro-chipping in addition to micro-breaking lead to a characteristic grooved wear surface and introduce large plastic deformation at the surface. Impact jet wear occurs at incident angles of approximately 90° and causes surface distortion by introducing material stresses. Stress maxima can be induced at and beneath the surface, which can cause cyclically changing multiaxial compressive and tensile stresses. The generation and accumulation of dislocations leads to the creation of voids that can combine to form cracks and produce wear particles if the cracks reach a critical length. Typically, the worn surface as a result of impact jet wear shows crater-like pits with deformed edges. Angular jet wear includes incident angles of

0° to 90° where the impulse can be divided into a sliding wear and impact wear component and depending on the incident angle the magnitude of the components and expected wear rate and wear mechanism varies. The kinetic energy of the abrasive particles arriving at the material surface goes into elastic-plastic deformation, fracture energy for the generation of new surfaces and other secondary processes such as the formation of a reaction layer [65]. The fraction of plastic deformation is increased with increasing grain size at otherwise constant conditions. The hardness of the abrasive particles in relation to the worn material influences the wear behaviour as well, if the hardness of the abrasive particles is higher than the worn material the wear volume depends on the toughness more than the hardness [65].

Blasting of cutting tool coatings deposited by CVD and PVD, particularly Al_2O_3, has shown to have the ability to transform coatings from a state of residual tensile stress to residual compressive stress and create a stress profile in the coating depth up to 1.5 µm [24, 25, 26, 27, 28]. This change of residual stress state can lead to the closing of thermal cracks [25, 28]. Further, blasting post-treatment after coating deposition has been shown to increase coating hardness as well as fracture toughness and decrease surface roughness, which can positively influence other relevant properties, such as friction coefficient and adhesion. This leads to better wear resistance and overall improved tool life [24, 26, 28, 29, 66]. Blast-treatment can be performed either dry or wet, where the abrasive particles are accelerated towards the cutting tool insert either by high-pressure air or water, respectively [29]. Bouzakis et al. [31] concluded that wet-blasting post-treatment is more suitable for increasing tool life from wet- and dry-blasting experiments on PVD TiAlN coatings.

The parameters that can be tuned during the blast-treatment are the blasting medium, its shape and size, the blasting pressure and time. It has been reported, that the surface roughness after blast-treatment increases with decreasing grain size [24, 29]. This can be explained by more intense microchipping by finer grains, taking away material, while coarser grains lead to more plastic deformation [24, 65]. Furthermore, more pronounced compressive residual stress has been observed when an edged abrasive medium is applied in comparison to globular-shaped particles [27]. An increase in blasting pressure leads to an increase in hardness related to the introduction of compressive residual stresses if they were not sufficient previously [24, 30]. The effect of the blasting pressure on the surface roughness is unclear, however, the tribological properties were found to depend strongly on the blasting time, where increased blasting time leads to a reduction of surface roughness [29].

4

Experimental Methods

In the following sections, the experimental methods applied to deposit and post-treat the investigated samples are presented. Deposition of coatings, as well as quality checks by XRD on the as-deposited coatings, were performed by Walter. Blasting post-treatment was conducted by Sandvik Coromant. More detailed characterization of the as-deposited as well as blast-treated samples was performed in the scope of this thesis by SEM, STEM, EDS and TKD, including the preparation of thin foiled cross-sections in a focused ion beam (FIB)-SEM. The samples and performed characterization are summarized in Table 4.1. The rake face edges were examined by plan-view SEM overview imaging for all samples. STEM investigations of the as-deposited samples had been done by Olof Bäcke previously, and the data from his work that is included in the results is marked accordingly. The blast-treated samples were investigated by STEM and TKD in the scope of this work. EDS was performed alongside the investigations by SEM and STEM.

Table 4.1: Overview of investigated samples: sample geometry, nominal lamella periodicity (λ_n), post-treatment (if applicable) and means of characterization performed within the presented work. Some characterization by STEM was performed previously by Olof Bäcke (marked with "OB"). Geometry 1 and 2 refer to SNMA120404 and SPHW120408 geometry according to ISO 1832, respectively.

sample	geometry	λ_n [nm]	state	characterization
6_1_asdep	1	6	as-deposited	SEM, STEM (OB)
15_1_asdep		15	as-deposited	SEM, STEM (OB)
50_1_asdep		50	as-deposited	SEM, STEM (OB)
6_1_bltr	1	6	blast-treated	SEM, STEM, TKD
15_1_bltr		15	blast-treated	SEM, STEM, TKD
6_2_asdep	2	6	as-deposited	SEM
15_2_asdep		15	as-deposited	SEM
50_2_asdep		50	as-deposited	SEM, STEM
6_2_bltr	2	6	blast-treated	SEM
15_2_bltr		15	blast-treated	SEM
50_2_bltr		50	blast-treated	SEM, STEM, TKD

4.1 Coating Deposition by LPCVD

TiN/TiAlN/TiN multilayers were deposited on cemented carbide substrates of ISO 1832 SNMA120404 (geometry 1) and SPHW120408 (geometry 2) geometry. The compositions of the substrates were 94 wt.% WC with 6 wt.% Co and 90.6 wt.% WC with 1.4 wt.% other carbides and 8.0 wt.% Co, respectively. The substrates were polished and cleaned with ethanol before deposition and arranged with the rake face horizontally in the reactor. LPCVD was performed in an industrial hot-wall CVD reactor with a rotating precursor gas supply. First, a roughly 1 µm thick TiN layer was deposited at 850 °C and a pressure below 150 mbar with $TiCl_4$, N_2 and H_2 as precursor and carrier gases. The TiN layer serves as a diffusion barrier for Co from the substrate, as well as an adhesion layer between the cemented carbide substrate and the following TiAlN coating [5]. Subsequently, TiAlN was deposited with a thickness of approximately 6 µm using $AlCl_3$, $TiCl_4$, NH_3 and H_2 as precursor gases at a deposition temperature of 725 °C and a pressure below 25 mbar. Three different rotation speeds of the precursor gas beam enabled the deposition of TiAlN coatings with expected lamella periodicities of about 6, 15 and 50 nm. An outer TiN layer of approximately 0.5 µm thickness was deposited with the same deposition parameters as the initial TiN layer. This top TiN layer serves as a decor layer and provides easy wear detection [5].

The quality of the coatings was examined by XRD to ensure that primarily fcc-structured TiAlN was formed by the deposition process, with a preferred (111) texture and only small fractions of hexagonal AlN. Table 4.2 summarizes the acquired data from XRD of as-deposited samples. The Al content was determined according to Vegard's law (Equation 3.1 with $a = 4.241\,73$ Å for cubic TiN (PDF 00-038-1420) [50] and $a = 4.0450$ Å for cubic AlN (PDF 01-077-6808) [50]) using the lattice parameter determined from the XRD peak positions. The normalized peak areas of the hexagonal AlN (100) peak give an indication of the amount of hexagonal AlN in the coating, where values below 1 indicate amounts that are insignificant for the coating properties. The very low value of 0.05 for the sample with a periodicity of 15 nm suggests that the intensities at the peak position were at the background level. Modelled intensities were corrected with respect to the present film thickness and absorption (presented in section A.1) to calculate the presented texture coefficients of the TiAlN coating. One sample of each geometry and each deposition run with the three different rotation speeds was investigated in the as-deposited state. Another sample of each geometry and each deposition run with the three different rotation speeds was blast-treated as described in the following section and investigated subsequently. This accounts for 12 samples in total, though one sample out of this row was missing, the blast-treated sample of SNMA120404 geometry with the largest lamella spacing (50 nm) (Table 4.1). However, it is expected that the coatings on both used geometries can be compared as they both show largely flat surfaces without complicated convex and concave features such as chip breakers and the gas flow should therefore be similar leading to comparable deposition behaviour..

Table 4.2: Phase information determined from XRD data from the as-deposited samples deposited by LPCVD in one deposition process.

lamella periodicity [nm]	6	15	50
Al content [at.%]	81.2	85.4	82.9
normalized peak area hex. AlN (100)	0.44	0.05	0.51
texture coefficient (111)	1.1	1.9	1.5
texture coefficient (220)	1.8	0.8	1.2
texture coefficient (200)	0.1	0.3	0.3

4.2 Post-treatment

Blasting post-treatment was performed according to the European patent EP 3 872 222 [67]. Wet-blasting was done at an angle of 90° to the sample surface (top-blasting) using an Al_2O_3 (corundum) grit and a pressure of 2.0 bar for 54 minutes for one net of inserts. A mesh grit size of FEPA 230 was applied according to the FEPA (Federation of European Producers of Abrasives) standard, corresponding to a mean grit size of about 82 µm.

4.3 Scanning Electron Microscopy

During SEM an electron beam scans along a sequence of positions on the specimen [68]. Due to different interactions of the electrons with the specimen, contrast is introduced, and an image is recorded by detecting electrons emitted by the sample. A schematic of the electron column of an SEM is shown in Figure 4.1. The electron beam can be produced by a thermionic gun or a field emission gun (FEG) [69]. Advantages of a FEG include a substantially higher gun brightness and a small diameter of the crossover. However, short-term fluctuations (noise) and long-term drift of the emission current can occur. The resulting electron beam is then demagnified by a set of electromagnetic lenses [68]. The electron beam first travels through one to three condenser lenses before it reaches the final objective lens. The objective lens additionally contains scanning coils, a stigmator, and a beam-limiting aperture. By shifting the beam under the aid of electromagnetic coils, the electron beam is scanned across the surface of the specimen. When the electrons reach the specimen, elastic as well as inelastic scattering occurs. As a result, secondary electrons (SE) and backscattered electrons (BSE) - among others - are ejected [69]. The SE excited directly by the primary electron beam exit the specimen from a very thin surface layer with only a few nanometres thickness, which leads to possible resolutions of 1-20 nm. SE mainly image the surface topography as the yield of SE depends on the tilt angle, with enhanced emission at edges and small particles. The emission of BSE also depends on surface tilt, but more importantly, the dependence of the backscattering coefficient on the mean atomic number Z provides contrast. The

resolution during imaging with BSE is reduced in comparison to SE because the electrons stem from a larger information volume [69].

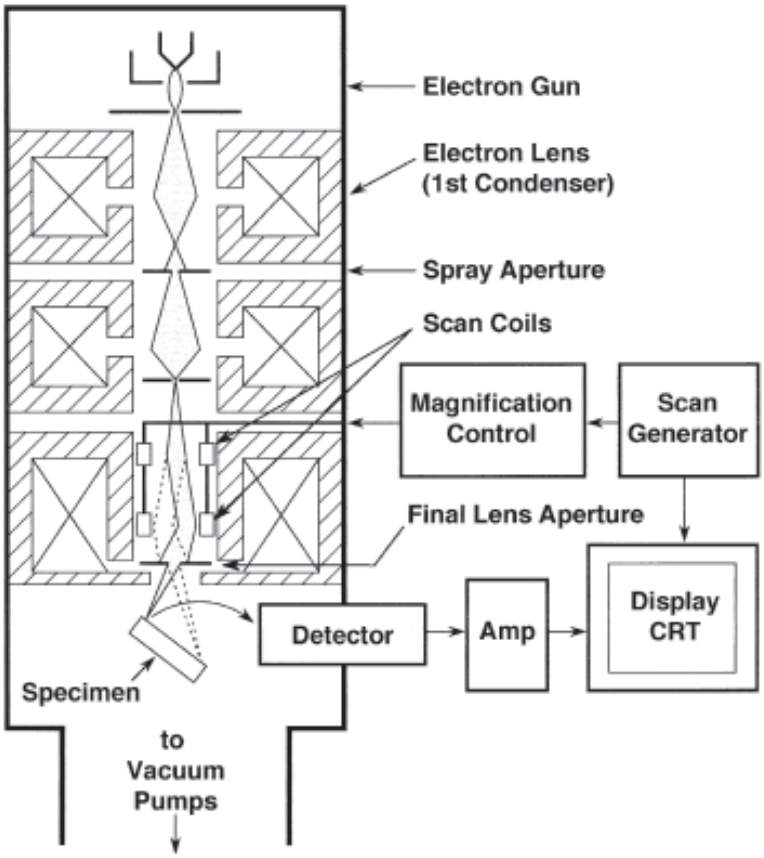

Figure 4.1: Schematic of the electron column in an SEM. The sequence of the electron gun, condenser lenses, apertures and scanning coils are shown. Taken from [68].

In this work, SEM images were acquired from a Zeiss LEO Ultra 55 FEG. Plan-view imaging of the rake face of as-deposited as well as blast-treated samples was done. SE were recorded using the in-lens detector at an acceleration voltage of 3 kV and a working distance of $1 - 3$ mm. Additionally, some images were acquired using a BSE detector at an acceleration voltage of 15 kV and a working distance of about 9 mm to help with the interpretation of contrast in the SE images of blast-treated samples.

4.4 Specimen Preparation Using a Focused Ion Beam

Similarly to SEM, the FIB rasters a beam across the sample surface [68]. The SE or the secondary ions emitted as a result of the ion bombardment can be used for imaging by plotting the resulting signal at each position, analogously to the SEM.

Additionally, the FIB can be used for milling the investigated material by sputtering. Positively charged ions from a liquid-metal ion source are used, most commonly Ga ions. In dual beam instruments, the SEM and FIB columns are arranged at an angle to each other, and the sample is positioned at the crossover of the two beams. This enables the preparation of precise, electron transparent cross-sections for (S)TEM and TKD, where the FIB is primarily used to cut the thin foil out of the bulk material by ion bombardment, while the SEM is used to observe the process. As a result of ion bombardment and implantation, a surface amorphous phase is formed on the specimens [70]. The thickness of this layer depends on the ion energy, angle of incidence, ion species and target material. To shield interesting regions from beam damage and amorphization, a protective layer, e.g. a Pt layer, can be deposited with the aid of the ion or electron beam. For this, a gas injector can be inserted, introducing a gaseous Pt-containing organometallic compound.

Thin foil specimens for STEM and TKD investigations were lifted out of the cutting tool insert with the help of a FIB in a dual-beam instrument (FIB-SEM). An FEI Versa 3D FIB-SEM that is equipped with a micromanipulator was used in this work. The electron and ion column are arranged at an angle of 52° with the cross-over at a working distance of about 10 mm. The steps of the preparation of thin foils are shown in Figure 4.2a to Figure 4.2f. The region of interest was first coated with a Pt layer to protect it from beam damage from the ion beam (Figure 4.2a), which is of particular importance in the case of the blast-treated samples, as the uppermost region is of interest. Typically, an area of 15 µm x 1.5 µm was coated with a thickness of roughly $2 - 4$ µm. A thicker Pt layer has shown to be useful to ensure the preservation of the upper area of the cross-sectional thin foil specimen. Subsequent milling was done at an acceleration voltage of 30 kV and varying currents depending on the highest possible removal rate while keeping the desired spatial accuracy for each step. Trenches were milled on each side of the deposited layer (Figure 4.2b). The edges of the resulting standing wall were undercut, leaving only one edge that attaches the thin-walled specimen to the sample (Figure 4.2c). The specimen was then welded to the micromanipulator by depositing Pt, cut free from the sample and lifted out by lowering the stage (Figure 4.2d). The specimen was attached to a Cu grid (Figure 4.2e) and a window was thinned to achieve electron transparency (Figure 4.2f). The last polishing steps were done at lower acceleration voltages of $2 - 5$ kV to achieve a thinner, negligible amorphous layer.

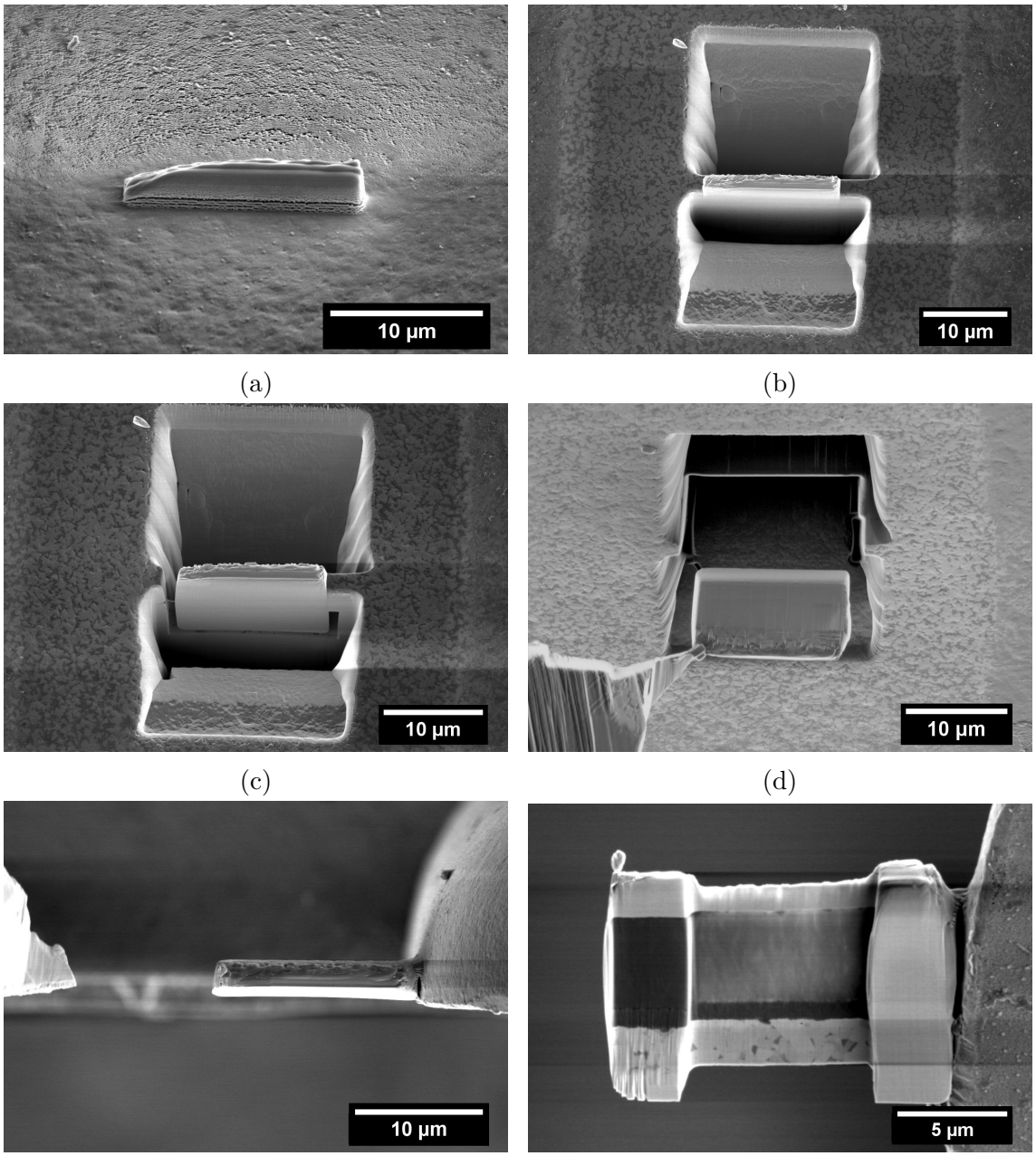

(a) (b) (c) (d) (e) (f)

Figure 4.2: Figures of the procedure of cross-sectional thin foil specimen preparation: (a) Electron (SE) image after Pt deposition (stage tilt: 52°). (b) Electron (SE) image after the cutting of the trenches (stage tilt: 7°). (c) Electron (SE) image after undercutting (stage tilt: 20°). (d) Ion image (SE) during liftout (stage tilt: 0°). (e) Electron (SE) image after attaching the lift-out to the copper grid (stage tilt: 0°). (f) Electron (SE) image after thinning (stage tilt: 54°).

4.5 Electron Backscatter Diffraction and Transmission Kikuchi Diffraction

Diffuse scattering of electrons in a bulk sample (done in electron backscatter diffraction (EBSD)) or a sufficiently thick thin foil specimen (done in TKD) leads to subsequent Bragg diffraction and formation of Kossel cones with an apex semiangle 90°-θ_B [71, 68]. The projections of Kossel cones on a screen are termed Kikuchi lines, which give information about crystallographic orientations as well as lattice distances. More precisely, the intersections of Kikuchi lines relate to specific orientations of a crystal (zone axes), while the distance between a pair of Kikuchi lines (width of Kikuchi bands) is inversely related to the spacing of lattice planes. This results in the possibility of using Kikuchi diffraction patterns extracted from EBSD or TKD measurements for phase identification as well as quantitative orientation determination. Both lateral and depth resolution in EBSD is strongly influenced by sample tilt [68]. While a large sample tilt results in a significantly increased backscatter yield, it is also responsible for a degraded lateral resolution. However, the spatial resolution of EBSD is higher than that of backscattered electron imaging because only electrons that have kept most of the initial electron beam energy contribute to the pattern. Therefore, spatial resolution is influenced by the electron probe size and the depth resolution is confined to the near-surface region of about $10 - 100$ nm in depth. Additionally, the accelerating voltage, as well as the mean atomic number Z will influence the spatial resolution. Improvement of spatial resolution is achieved at decreased acceleration voltages and increased Z. Due to the restricted volume in samples considered in TKD measurements, the interaction volume is smaller in comparison to conventional EBSD, therefore it is possible to index patterns from particles smaller than 10 nm [72]. In addition, the quality of Kikuchi diffraction patterns in TKD is higher in comparison to conventional EBSD, because of the reduction of multiple scattering that is confirmed by higher average energy and narrower energy spread (narrower full-width at half-maximum) of electrons in TKD in comparison to EBSD.

The experimental setup for conventional EBSD measurements as well transmission-EBSD - also termed TKD - in an SEM are shown in Figure 4.3. Bulk samples measured in EBSD measurements are typically tilted at an angle of about 70° between the optical axis and the sample normal towards the detector at working distances of about 15 mm. The sample tilt serves as a balancing angle between achieving a good signal-to-noise ratio as well as sufficient resolution [68, 73]. TKD measurements are commonly done at a specimen tilt of 20° between the optical axis and the sample normal away from the detector to minimize the backscattering of electrons towards the detector and simultaneously maximize the detection of transmitted electrons that have scattered through large angles [72]. Working distances of about 5 mm are frequently applied to detect large parts of the Kikuchi pattern.

TKD measurements were done in a Tescan Gaia3 FIB-SEM equipped with an EBSD detector at an acceleration voltage of 15 kV, a step size of $20 - 50$ nm on

the cross-sectional thin foil lift outs from different positions of the cutting insert. Kikuchi lines were detected and processed by the Oxford Instruments AZtec software, which provides indexing based on comparison with a theoretically calculated electron backscatter pattern (EBSP) connected to the expected crystal structure. Data analysis was performed with the help of the free Matlab toolbox MTEX [74]. The code used for analysis can be found in section A.2. Plotting of orientation maps was done using inverse pole figure (IPF) colouring that connects the orientations to a colour distribution [75]. In addition, the grain orientation spread (GOS) was visualized using the unfiltered data, which shows the average misorientation angle of a grain from the grain's mean orientation [76]. The half-quadratic filter was applied for denoising and filling missing data. This filter considers the next neighbours of a pixel and attempts to restore the original image from corrupted data by minimizing energy functionals [77]. This can include denoising of additive Gaussian noise, as well as filling missing image values. The minimization of the energy functional is performed by reformulating the problem so that it is quadratic with respect to the image, which allows efficient computation. This filter was chosen because it is edge-preserving and would be suitable to show subgrain boundaries if they were to arise from the blast-treatment. The orientation distribution function (ODF) was calculated, which associates each orientation with the volume percentage of grains with the same orientation, giving a quantitative description of the texture in units of multiples of uniform pole density (MUD) [78]. Furthermore, the grain reference orientation deviation (GROD) was computed which represents the misorientation of the orientation at a specified position compared to the mean orientation of the grain to which the position belongs to [76].

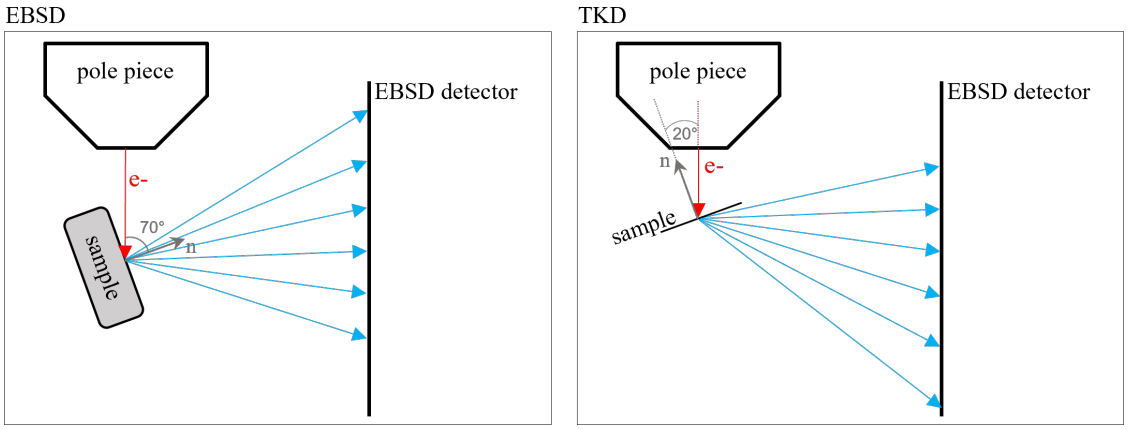

Figure 4.3: Experimental setup of EBSD and TKD measurements in an SEM. During EBSD the sample normal $\vec{n}$ of a bulk sample is tilted towards the detector at an angle of 70° to the optical axis. In contrast, the sample normal $\vec{n}$ of a thin foil specimen is tilted away from the detector at an angle of 20° to the optical axis to perform TKD.

4.6 Transmission Electron Microscopy

The TEM consists of three main parts: the illumination system, the objective lens and stage (image forming system) and the projection and image recording system [71]. The illumination system includes the electron gun and condenser lenses. The projection and image recording system magnifies the image produced by the objective lens and projects it onto a fluorescent screen or charge-coupled device (CCD) camera. The general setup of a TEM is shown in Figure 4.4. Depending on the strength of the intermediate lens, an image or a diffraction pattern can be formed. In the following paragraph, the basic principles of TEM are presented.

Within the illumination system, the electrons from the gun are transferred to the specimen [71]. While conventional TEM requires a parallel beam, a convergent beam is used in STEM and analytical electron microscopy (AEM)). Different electron sources and their advantages have been discussed in section 4.3. Due to the reduced initial source size of FEGs, they are preferred in applications of a convergent beam. After leaving the electron gun, the electrons are accelerated by an anode with acceleration voltages of 100 to 300 kV [79]. A set of three condenser lenses C1, C2 and C3 creates either a parallel or a convergent beam on the sample. The first condenser lens C1 collects the electrons coming from the source and creates a demagnified image. C1 is used to control the probe size and the beam current at the specimen. The C2 lens controls the illuminated area on the specimen, and the C2 aperture controls the convergence angle of the electrons. The C3 lens provides the possibility to easily switch between a parallel and convergent beam and enables the independent adjustment of the illumination area and the convergence angle. Following the C3 lens, the objective lens and the stage containing the specimen are positioned next in the TEM column. The objective lens is a crucial part, as it controls the quality of information that is obtained. The images and diffraction patterns are formed by the objective lens. The thin foil specimen, thin enough for electrons to be transmitted, is positioned between the upper and the lower pole piece of the objective lens. The imaging system which is positioned below the objective lens and stage can be operated in two basic modes: the diffraction and imaging mode [71]. In order to obtain a diffraction pattern, the back focal plane of the objective lens has to act as the object plane for the intermediate lens. If an image is wished to be projected onto the viewing screen/CCD camera, the intermediate lens has to be readjusted so that the object plane is the image plane of the objective lens. The selected area diffraction (SAD) aperture is inserted to select a region on the specimen from which the diffraction pattern will result. The objective aperture is inserted in order to create bright field (BF) or dark field (DF) images. While areas in which the beam has not been Bragg reflected will appear bright in BF images, the objective aperture can be moved to select scattered electrons instead of the direct beam, resulting in bright areas where the beam has been diffracted and dark areas where it has not.

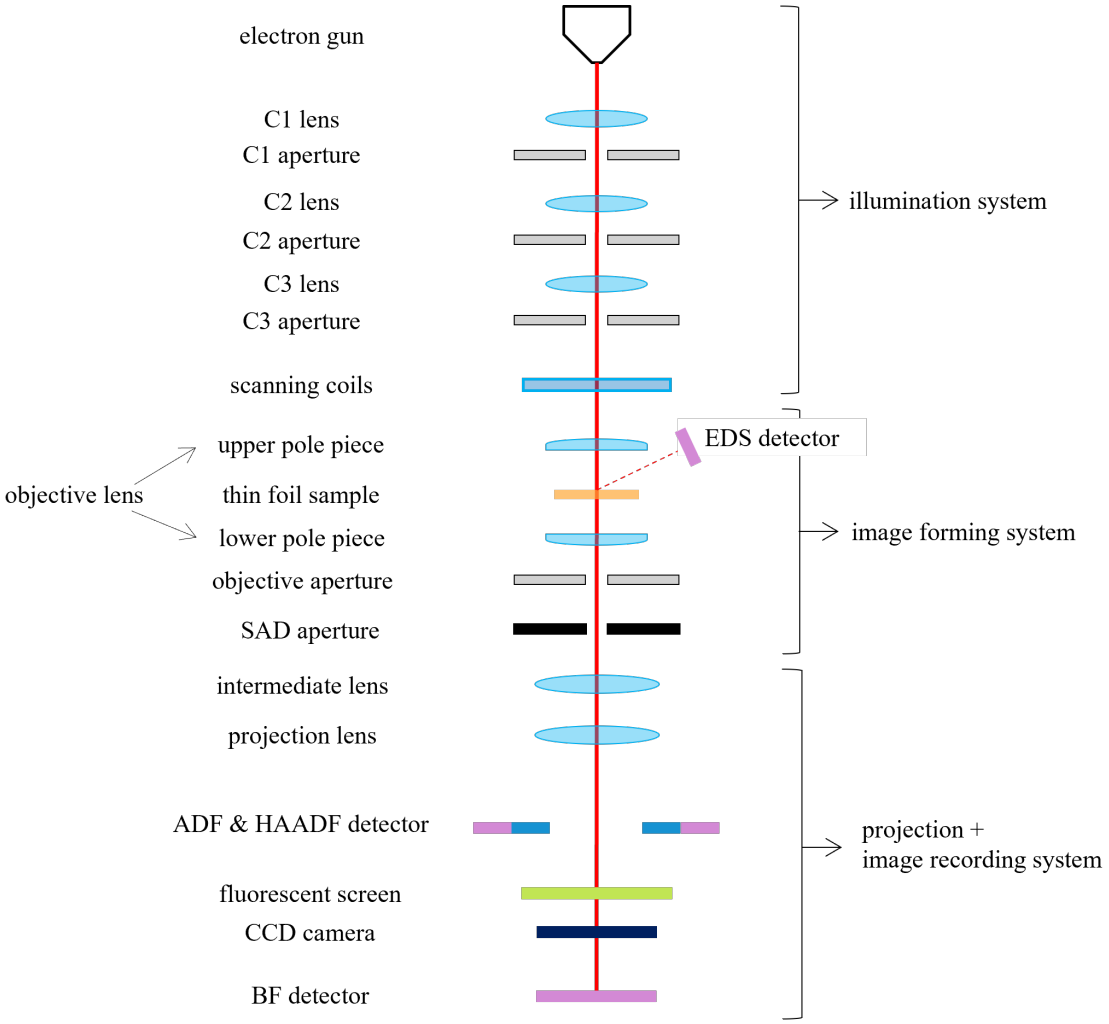

Figure 4.4: Schematic setup of a (S)TEM equipped with a detector for EDS [79, 56].

4.6.1 Scanning Transmission Electron Microscopy

As mentioned in the previous section, a convergent electron beam is desired during STEM operations [71]. The electron scattering processes vary depending on the angle at which the electron beam enters the sample (e.g. diffraction patterns depend on the orientation of the incoming electron beam in relation to the crystallite orientation), therefore the electron beam must stay parallel to the optical axis during the scanning action. This is attained by tilting the beam twice with a pair of scan coils. Then, the C3 lens produces a beam that is parallel to the optic axis, with a C1 lens crossover at the specimen plane. The resulting diffraction pattern is stationary during the scanning. In contrast to TEM imaging, the objective lens does not determine the image quality, instead, the STEM image quality depends on the size and aberrations of the probe. BF imaging in STEM mode entails the visualization of the different intensities of the direct beam at the different positions in the sample. Analogously to the TEM operation mode, any or all of the scattered electrons are selected to form a DF image. However, it is not achieved by tilting

the beam but by shifting the stationary diffraction pattern so that the scattered beam is on the optical axis, hitting the BF detector. Additionally, annular dark field (ADF) imaging can be applied by using an annular detector which surrounds the BF detector. Electrons that are scattered to even higher angles can be detected by another detector surrounding the ADF detector. This is called high-angle annular dark field (HAADF) imaging and provides good Z-contrast while minimizing diffraction contrast, which is interesting for imaging of the nanolamellae of different compositions in the present TiAlN coatings.

In this work, an FEI Titan 80-300 TEM/STEM instrument was operated at 300 kV acceleration voltage in STEM mode. The thin foiled specimens of a cross-section of the coatings on different inserts and positions attached to a Cu grid were mounted in a double-tilt holder. The double tilt holder allows rotation along two axes: α-tilt along the holder axis and β-tilt along the axis in the sample plane and perpendicular to the holder axis. This allows tilting of the specimen to find the suitable zone axis of an individual grain to see the Ti- and Al-rich lamellae. Because the lamellae grow along the <100> directions, the suitable zone axis to observe the lamellae formation is <110> or <100>. STEM BF and HAADF images were recorded.

4.7 Energy-Dispersive X-ray Spectroscopy

The elements present in a material can be determined and quantified by EDS [68]. When a material is irradiated with electrons, x-ray photons are generated within the interaction volume. While the deceleration of electrons results in the production of continuous x-rays (Bremsstrahlung) the interaction with specific shells of an atom results in x-ray photons of specific energies. During the interaction of the beam electron with an atom, it is possible that an inner shell electron is ejected - the atom is ionized and in an excited state. The incident beam electron leaves, having lost the energy necessary to ionize the atom (binding energy). The atom will relax to its ionized ground state by filling the inner shell vacancy with an outer shell electron. For this action, there is only a limited set of allowed transitions. The energy difference of the excited and ground state can be released by two mechanisms, one of which is the ejection of an x-ray photon with a sharply defined energy. By measuring and analysing the energy of ejected x-rays during electron irradiation, the type and relative quantity of atoms can be determined. The resolution is limited by the excitation volume, which is in the order of $1 - 3\,\mu m$ in the case of bulk samples, however, the resolution can be improved in thin-foiled specimens where the excitation volume is reduced significantly [69].

In this work, EDS measurements were performed both in SEM and STEM. Measurements in SEM were performed in a Tescan Gaia3 FIB-SEM equipped with an EDS detector. Point and area measurements were performed at an acceleration voltage of 20 kV and a working distance of about 10 mm. Measurements in STEM mode were performed in an FEI Titan 80-300 TEM/STEM. Evaluation of the acquired spectra was performed within the Oxford Instruments AZtec software and the TEM imaging & analysis (TIA) software by Thermo Fisher Scientific. Because the decon-

volution of the Ti and N peaks is challenging and the N content was not in focus for the present work, quantification was performed by only regarding Ti and Al peak contributions.

5

Results and Discussion

5.1 Surface Morphology Before and After Blast-Treatment

The surface morphology was studied in order to reveal information about the growth and how it varies across the edges of the inserts. The focus was put on the surface morphology of TiAlN, however, the growth of the additional thin TiN top layer made the interpretation more difficult in the as-deposited case and its growth varied in addition to the TiAlN growth.

Plan-view SEM imaging of one rake face of all coated cutting tool inserts was performed as described in section 4.3 to study the surface morphology. Images were taken in 1 mm steps along the edge at a distance of 300 µm from the insert edge. At the cutting edges, additional images were taken at distances of 100 µm and 500 µm. Mostly SE were imaged, sometimes complemented by BSE imaging and EDS measurements. The observations both before and after blasting are presented and discussed in the following sections.

5.1.1 Surface Morphology Before Blast-Treatment

The surface morphology of the as-deposited samples could be categorized into two distinctly different surface morphologies of TiAlN. The first surface morphology that was distinguished, is the previously reported pyramidal surface morphology, which additionally could be divided into two different modifications in the present case. Firstly, the previously found sharp pyramids (Figure 5.1a) and secondly, truncated pyramids that reveal an additional surface at the top (Figure 5.1b). The second surface morphology is a ridge-like surface morphology. Analogously to the pyramidal case, both sharp ridges and truncated ridges revealing an additional surface were observed (Figure 5.2a and Figure 5.2b). A closer look at the surface revealed by the truncation in Figure 5.3a and Figure 5.3b, shows that the top surface is not flat as the facets on the sides, but shows smaller pyramids or ridges.

As mentioned previously, the morphology as a result of TiAlN growth is of interest in this work, and the additional TiN layer in the present case makes the interpretation more difficult. In order to verify, that the truncation and the small pyramids or ridges on the top surfaces that are evident on truncated grains are a result of TiAlN growth and are replicated by the TiN layer instead of being a feature inherent

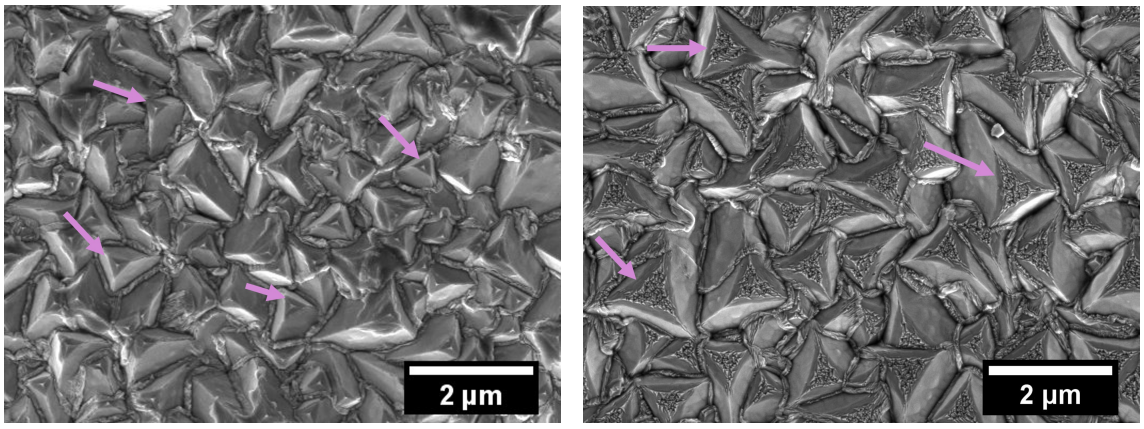

(a) (b)

Figure 5.1: Examples of the pyramidal surface morphology of the as-deposited samples. Imaged by SEM detecting SE with an in-lens detector. (a) Sharp pyramids. (b) Truncated pyramids.

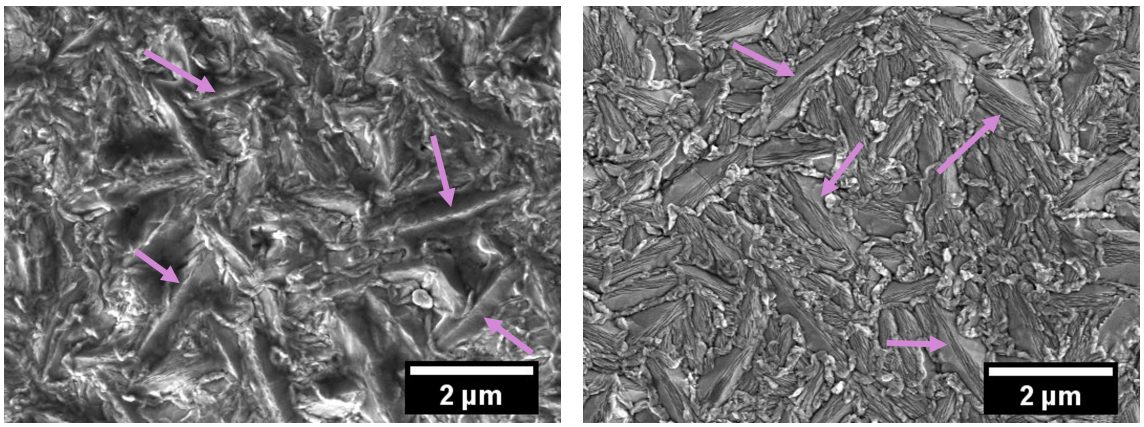

(a) (b)

Figure 5.2: Examples of the ridge-like surface morphology of the as-deposited samples. Imaged by SEM detecting SE with an in-lens detector. (a) Sharp ridges. (b) Truncated ridges.

to the TiN growth, previously done STEM imaging of the as-deposited coatings is taken into consideration. Figure 5.4 shows a STEM HAADF image of the surface region of the coating in cross-section. The side facets of the TiAlN do not meet to close but reveal a top surface which is reproduced by the TiN layer. Therefore, the surface morphology of truncated pyramids and ridges is inherent to the TiAlN growth and not the TiN growth. In addition, the TiAlN grain shows small steps on the surface revealed by the truncation, which is amplified by the growth of the top TiN layer which shows even larger steps or small facets. This can be connected to the small pyramids and ridges shown in Figure 5.3 on the top surface revealed by the truncation.

The surface morphology was categorized in all acquired images and Figure 5.5 sum-

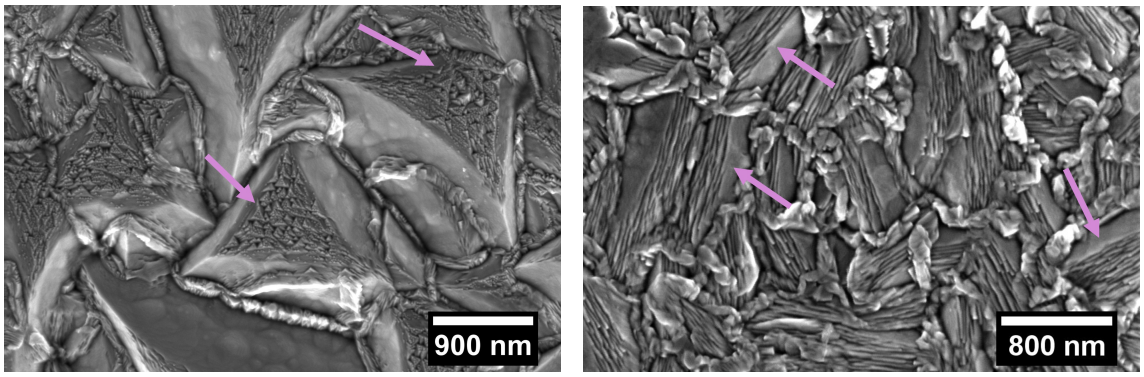

(a) (b)

Figure 5.3: The top surface revealed by the truncation of the pyramidal and ridge-like grains shows smaller facets leading to pyramidal or ridge-like morphology. Imaged by SEM detecting SE with an in-lens detector. (a) Example of the pyramidal morphology. (b) Example of the ridge-like morphology.

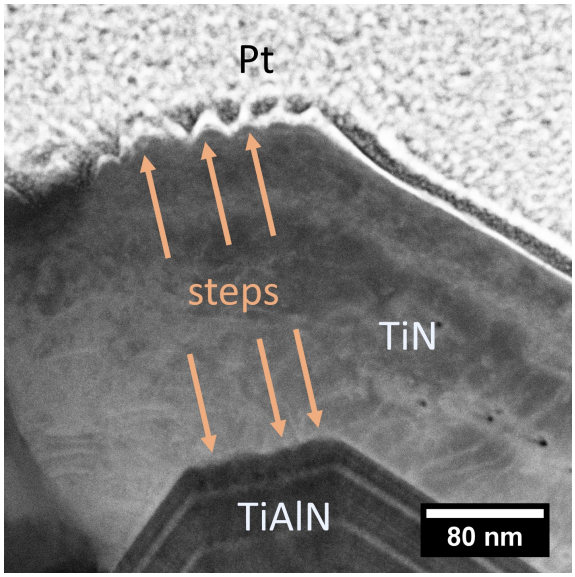

Figure 5.4: STEM HAADF image of a truncated TiAlN grain and the TiN layer on top that amplifies the small steps on the top surface. Image taken by Olof Bäcke.

marizes how it varies along the insert edges for both investigated geometries and the three rotation speeds. Example images of the surface morphology and its variations within one of the determined categories can be found in appendix A.3.1. This overview does not suggest a simple connection to the rotation speed or the gas flow direction. Slight rotations in the actual orientation of the samples in relation to the gas flow could be present and could lead to the surface morphology being more symmetric to the gas flow direction, for example in the case of the sample with geometry 1 and a lamella periodicity of 6 nm, where geometry 1 and 2 have slightly varying shape, but both show largely flat surfaces. However, this possible symmetry to the gas flow does not seem as obvious in all cases. As expected, the geometry does not seem to play an important role in how the surface morphology varies and is

similar comparing geometry 1 and 2 of one deposition run. Though the connections to the gas flow or rotation speed are not clear, the surface morphology varies very locally. Two parameters that can influence this are the temperature and local flow conditions. Because the temperature is not expected to vary decisively within these small distances (µm to mm), it is suspected that the local variations in surface morphology are induced by variations in the local flow conditions. This also suggests that the optimal deposition conditions to achieve one or the other morphology have a very narrow range at the present deposition conditions.

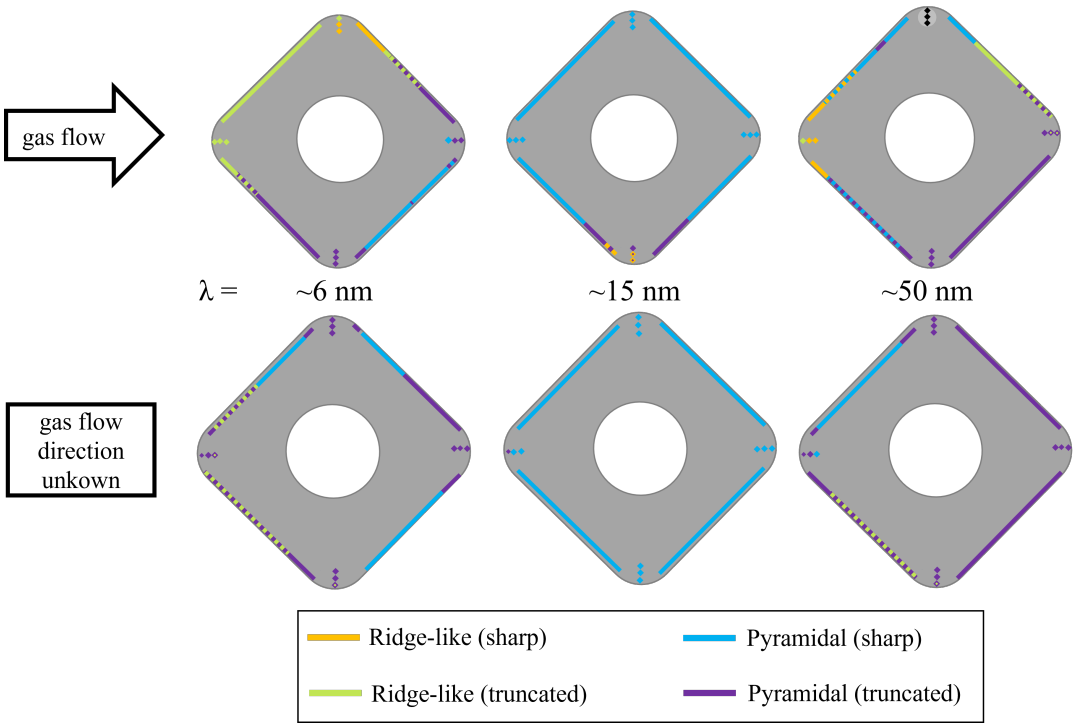

Figure 5.5: Overview of the surface morphology along the edges of the as-deposited samples of different rotation speeds and resulting lamella periodicity. The top row represents inserts with geometry 1, the bottom row represents inserts with geometry 2. Mixed surface morphology was observed in regions that are multicoloured.

The overview imaging along the edges of the inserts by SEM not only revealed the different surface morphologies described above, but also varying grain sizes across single inserts as well as between different inserts coated in the same deposition run. Images illustrating the extent of variations within one insert and between inserts deposited in the same deposition run can be found in appendix A.3.2. This further illustrates how small changes in deposition parameters change the growth of the coating, as has already been concluded from the varying surface morphology across the inserts (Figure 5.5). Though, it also has to be considered that not only different positions in the reactor are compared, but also different sample geometries that could slightly change local flow conditions as well. In addition, crack networks in the coatings were observed that extend both intragranularly and mostly intergranularly, an example is shown in Figure 5.6. These cracks should be thermal cracks that are

typical for coatings deposited by CVD [25, 28]. The existence of cooling cracks in the coatings in the as-deposited state could indicate tensile residual stresses in the coating.

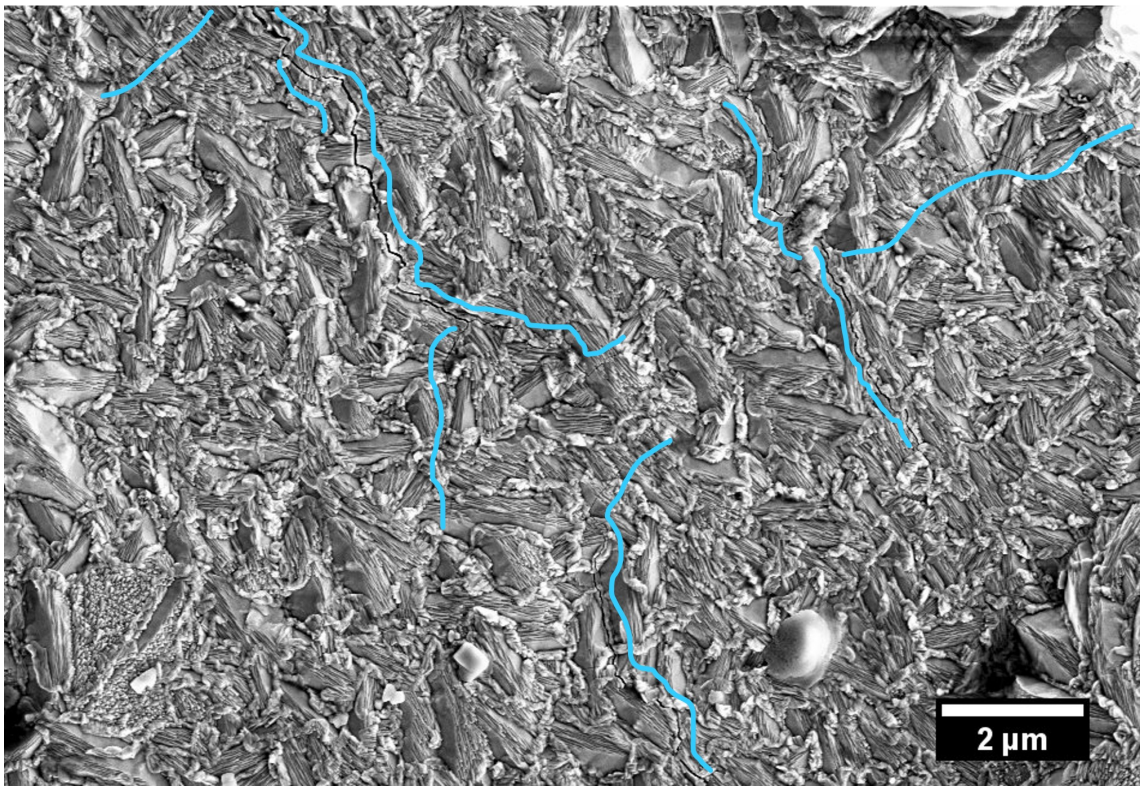

Figure 5.6: Example of cracks found in the coatings. The blue lines indicate cracks next to it. Imaged by SEM detecting SE with an in-lens detector.

5.1.2 Effects of the Blast-Treatment on the Surface Morphology

Imaging with SE of the blast-treated samples revealed a relatively smooth surface compared to the as-deposited case. In addition, it was possible to distinguish previously pyramidal and ridge-like grains after the blast-treatment owing to the remnants of the top TiN layer. In Figure 5.7a the contrast reveals triangular shapes where EDS measurements showed that the areas that appear lighter in Figure 5.7a have a higher Ti content and substantially lower Al content compared to the darker appearing areas, indicating that the lighter areas are remnants of the TiN layer deposited in the valleys of the pyramidal grains. The corresponding EDS map can be found in appendix A.4. Analogously, the previously ridge-like morphology can be distinguished, as shown in Figure 5.7b. Yet, it has to be mentioned that the presented examples are extremes and the previous morphologies cannot be distinguished as easily in all cases. Also, it cannot be distinguished whether the grains originally grew with sharp edges or with truncation.

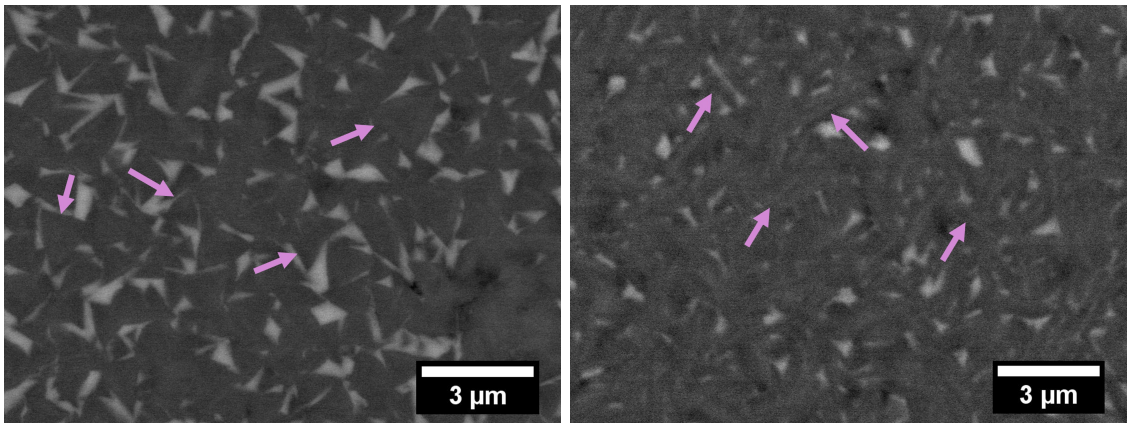

(a) (b)

Figure 5.7: Surface morphology after blast-treatment, imaged by SEM BSE. Previously pyramidal and ridge-like grains can be distinguished owing to the brighter remnants of the top TiN layer. (a) Pyramidal grains. (b) Ridge-like grains.

The remnants of the TiN layer give an indication of how much material was removed due to the blast-treatment, this is illustrated in cross-section in Figure 5.8. The deposited TiN layer had a thickness of around 0.5 µm, additionally taking into account the surface roughness of the TiAlN layer it can be approximated that about $0.5 - 0.8$ µm of the layer thickness was removed. The present depth of coating removal is in a range that does not destruct the protective nature of the coating, as the TiAlN layer is significantly thicker. Too much removal would reveal the substrate, negatively affecting the performance of the coated cutting tool during the application.

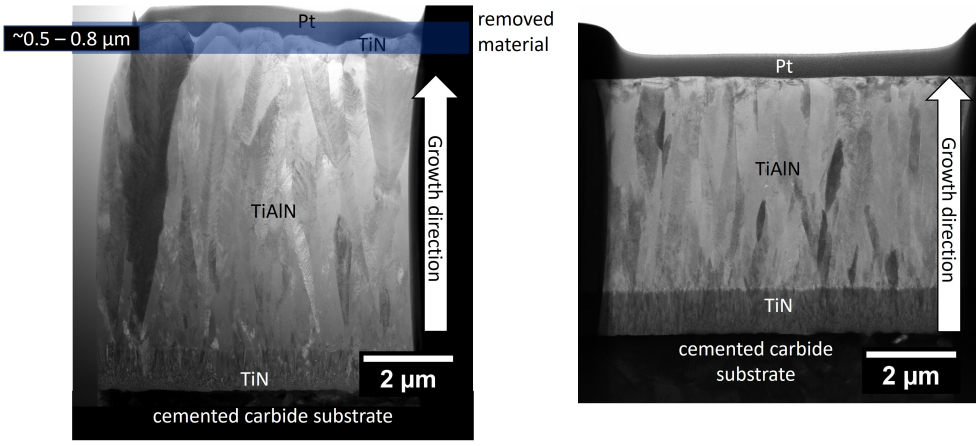

(a) (b)

Figure 5.8: STEM BF images (a) before and (b) after blast-treatment illustrating the amount of removed material as a result of the blast-treatment.

Besides the two appearances shown in Figure 5.7a and 5.7b, further appearances of the surface after blasting were observed, and more examples are shown in Figure 5.9. Figure 5.9a and 5.9b show traces of abrasive wear at different magnifications, where the grooves could be assigned to microchipping and micro-ploughing. This would imply substantial plastic deformation induced by the blast-treatment. Nevertheless, the presence of such traces following impact jet wear is an unexpected observation. As the trajectory of the particles is vertical to the substrate surface, crater-like pits with deformed edges are expected to form as a result of the blast-treatment performed [65]. Additionally, micro-breaking is expected in the case of a hard material such as TiAlN [65]. The traces might result from the particles that already reached the surface being pushed away by newly incoming particles transferring their impulse. Furthermore, the lateral confinement of the coating could lead to the possibility of increased plastic deformation instead of fracture necessary for micro-breaking. Figure 5.9c shows a surface where a wavy contrast variation reinforces the impression that the top surface of the coating has been substantially plastically deformed. It also shows a topography with some surface voids that possibly can be assigned to micro-breaking, the valleys of the surface morphology in the as-deposited case or closed thermal cracks. Though it cannot be clearly assigned in top view, this surface roughness does not seem to exceed far into the coating. It could however provide stress maxima, where crack initiation can happen when the coating is exposed to increased external stresses and wear [80]. Moreover, remanence of corundum particles was very rarely encountered on the sample surfaces subsequent to the blast-treatment procedure. Taking into account the overall aim of the blast-treatment to transform the coating from a state of residual tensile stress to residual compressive stress, the signs of strong plastic deformation can be an indication that the chosen blasting parameters are a suitable choice. The kinetic energy of the corundum particles arriving at the substrate surface converses to the energy necessary for elastic-plastic deformation, the generation of fracture surfaces, and secondary processes. Out of these processes, plastic deformation is suitable to change the stress state in the current scenario. The plastic deformation will be

discussed in further detail in section 5.3.

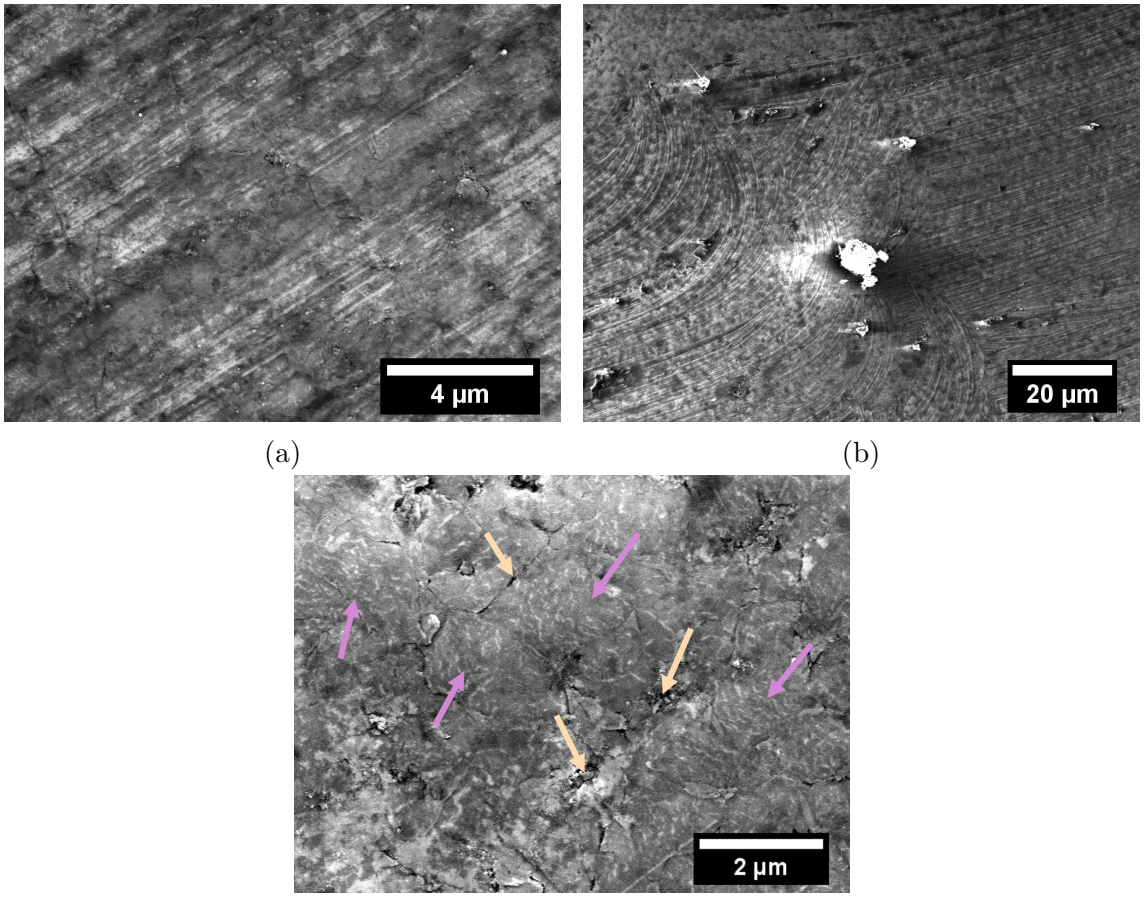

(a) (b)

(c)

Figure 5.9: Images by SEM SE with an in-lens detector of the coating surface after blast-treatment. (a), (b) Traces of abrasive wear (grooves) at different magnifications. (c) Wavy contrast variation (purple arrows) and surface voids (yellow arrows).

5.2 The Connection Between Surface Morphology and Growth

In prior studies, the presence of pyramidal surface morphology accompanied by a (111) texture observed in similar TiAlN coatings has been attributed to the phenomenon of "evolutionary selection". The enhanced growth rate of (111)-orientated grains is attributed to the high surface energy of {111} planes, while the grain exhibits {100} facets with low surface energy [1]. In the present case, an additional ridge-like morphology as well as truncation of pyramidal and ridge-like grains was observed. These morphologies will be connected to the local texture and to local growth conditions in the following sections.

5.2.1 Connection Between Local Texture and Facets

In order to connect the previously observed surface morphologies to the local textures, cross-sectional thin foils were prepared for TKD measurements. In Figure 5.10a and 5.10b, the surface morphologies at the cross-section positions are depicted. Figure 5.10a exhibits triangular remnants of TiAlN and TiN, indicating the presence of a pyramidal surface morphology in the as-deposited state. Conversely, Figure 5.10b showcases more elongated TiAlN and TiN remnants, indicating the presence of a previously ridge-like surface morphology. The IPF orientation maps at each position are shown in Figure 5.10c and 5.10d and their colouration already hints qualitatively what is shown quantitatively in the IPF of the corresponding ODF in Figure 5.10e and 5.10f. Unsurprisingly, the density in the <111> direction is increased in comparison to the uniform density at the position where the previously pyramidal surface morphology was determined (Figure 5.10e). At the position where a previously ridge-like surface morphology was determined, the orientation with the highest density deviates from this behaviour and shows the highest density in the <110> direction. It is therefore concluded that the pyramidal and ridge-like surface morphology are indications for the growth direction of the TiAlN grains, where a pyramidal surface morphology is connected to growth in the <111> direction and a ridge-like morphology is connected to growth in the <110> direction. The texture coefficients determined from XRD measurements presented in Table 4.2 reflect the presence of a mixed (111) and (220) texture as well. While the texture coefficient of (200) is very low, the texture coefficients of (111) and (220) have similar magnitudes. The (110) textured coating previously reported did not show the here presented ridge-like surface morphology [58].

The connection between the grain morphology and its growth direction is summarized in Figure 5.11 which also illustrates that both grain growth directions enable low-energy {100} facets. Out of the six {100} surfaces, there are three unique surfaces in the present case, resulting in three different possibilities for the low energy {100} facets to be positioned on a crystallite. Firstly, growth along a <100> direction, leading to the development of a flat {100} surface. This specific growth mode is not observed in the present case, as evidenced by the low (200) texture coefficient. Growth of a crystallite in <110> and <111> directions comprise the other two pos-

sibilities of revealing {100} facets leading to the observed morphologies summarized in Figure 5.11. These orientations are probably kinetically preferred in the competitive growth of randomly-orientated grains in a polycrystalline film ("evolutionary selection") [37]. From this point of view, it is not surprising to observe the pyramidal and ridge-like grain morphologies. This explanation serves to explain why {111} and {110} orientated grains can preferred in comparison to other random orientations in a coating of sufficient thickness. It should be mentioned, that inclined growth of such crystallites can also lead to a (211) overall texture of a coating, as described previously by Ben Hassine et al. [59]. In the present case, a seemingly random lateral mix between pyramidal and ridge-like grain morphologies is observed in some cases, but larger areas where only one of the grain morphologies is observed are also common. This indicates, that there is an additional factor influencing the grain orientation that is not purely random in nature. Possibilities include epitaxial growth on the underlying TiN layer. The local growth could also be influenced by locally varying deposition parameters, such as the temperature, gas concentrations and flow conditions. Also in this case, no major temperature variations within the distances in which local texture variations are observed are expected, which leaves gas concentration and flow conditions as critical deposition parameters. Further investigation would be necessary to understand this in detail.

5.2.2 Connection Between Grain Morphology and Facets

In the previous section, the surface morphology was connected to the local texture, as shown schematically in Figure 5.11. In Figure 5.1b and 5.2b grains with truncated pyramidal and ridge-like morphology were presented. The truncation leads to the formation of an additional surface. Geometrical considerations illustrated in Figure 5.12 show that these surfaces have significantly increased energy compared to the {100} facets of the sharp pyramids or ridges [61]. However, it was also noted above, that the surfaces revealed by the truncation were not flat but displayed small pyramids and ridges themselves (Figure 5.3) and that this is not inherent to the growth of the top TiN layer but is a feature of the TiAlN grains that is replicated and amplified by the TiN layer (Figure 5.4). Figure 5.13 shows a ridge-like TiAlN grain in an as-deposited coating. The zone axis, which is the normal of the image plane, has to be a direction orthogonal to a <100> direction in order to see the lamellae, as these grow along <100> directions. Because the lamellae are visible on both sides of the grain (the zone axis is orthogonal to the {100} directions on both sides of the grain), the zone axis has to be a <100> direction of the grain. As this orientation was achieved without major tilts of the cross-sectional thin foil in the TEM it is thus concluded that the grain has a <110> growth direction. Figure 5.13 illustrates that the truncation of the grains arises as a consequence of a growth mechanism, different from that observed in the sharp grains, as the lamellae are orientated differently in the core region of the grain, i.e. along <110>. Additionally, these lamellae appear "fuzzier" than the lamellae observed in the side regions of the TiAlN grains. A closer look at the top of the grain reveals that the surface shows steps with small facets. As they are parallel to the large {100} facets on the sides of the grain, it is believed that these facets are {100} surfaces and the high-energy

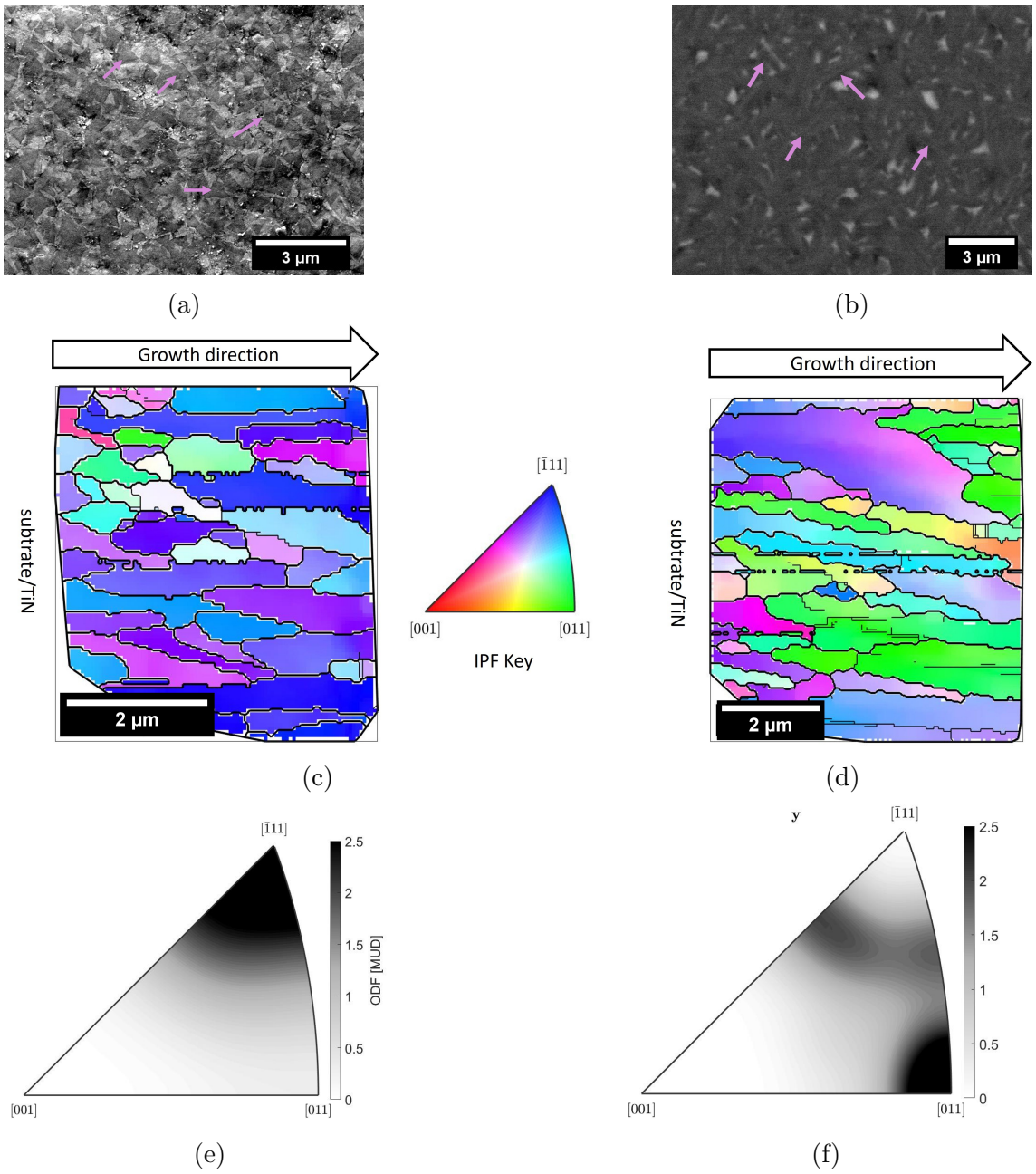

Figure 5.10: Connection of the surface morphology to the local texture. Previously pyramidal morphology is shown on the left (a,c,e), previously ridge-like morphology on the right (b,d,f). (a, b) Surface morphology at the position where the cross-section was prepared. (c, d) TKD IPF orientation map of the TiAlN coating cross-section along the growth direction. (e, f) IPF of the ODF along the growth direction in MUD.

surfaces shown in Figure 5.12 are not present. These facets have a size of only a few nanometres and because the thin foil is about $100-200$ nm thick the "fuzzy" appearance could be the result of a projection effect and the interfaces in the core region of the grain are in fact not less sharp than they are in the side regions. Driven by the low energy of the {100} surfaces that is present in TiN as well, the TiN layer on

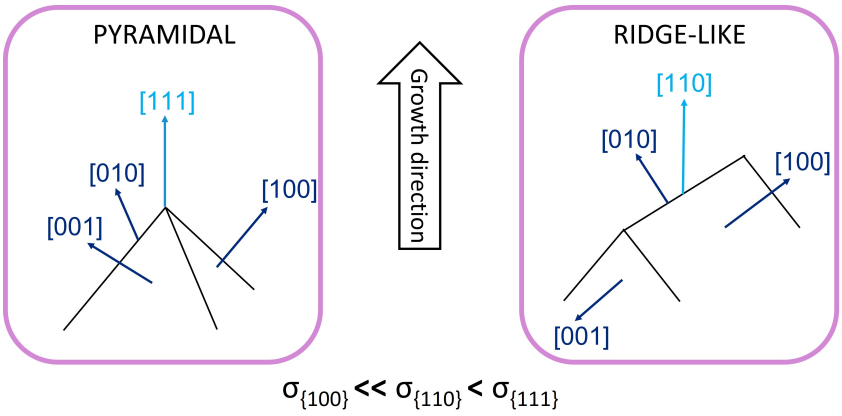

Figure 5.11: Schematics of the connection of the surface morphology to the grain orientation. The surface energy σ of the {100} facets is significantly lower than that of {110} and {111} facets [61]. Both grain orientations reveal the low-energy {100} facets.

top of the truncated TiAlN grain replicates and even amplifies the presence of small {100} facets on the top surface. This grain morphology is illustrated in Figure 5.14. In Figure 5.15 further characteristics of the truncated grains are summarized. On one hand, the width of the core region increases along the growth direction, indicating it is a stable mode of growth. Furthermore, EDS measurements presented in Table 5.1 revealed that the average Al content in the core region is higher than in the side regions with large area {100} facets, typically by about 5 at.%, excluding N in the quantification.

Table 5.1: Al and Ti contents determined by EDS in five core and side regions of truncated grains.

core		side		difference
$c_{Al}[at.\%]$	$c_{Ti}[at.\%]$	$c_{Al}[at.\%]$	$c_{Ti}[at.\%]$	Δc_{Al} [at.%]
88.4	11.6	84.2	15.8	4.2
88.4	11.6	82.8	17.2	5.6
89.7	10.3	84.1	15.9	5.6
84.5	15.5	82.7	17.3	1.8
85.3	14.7	80.5	19.5	4.8

In an attempt to explain the occurrence of the truncated grains and their characteristics, Figure 5.16a summarizes the findings described in the previous paragraph, where the growth direction is [110] or [111], in the latter case the [100] direction would merely be projected onto the image plane and is, in fact, pointing outside the image plane. Due to the small facets on the surface revealed by the truncation, many ledges and kinks are created where both adsorption and dissociation of precursor molecules are preferred, increasing the adsorption and dissociation rate as well as

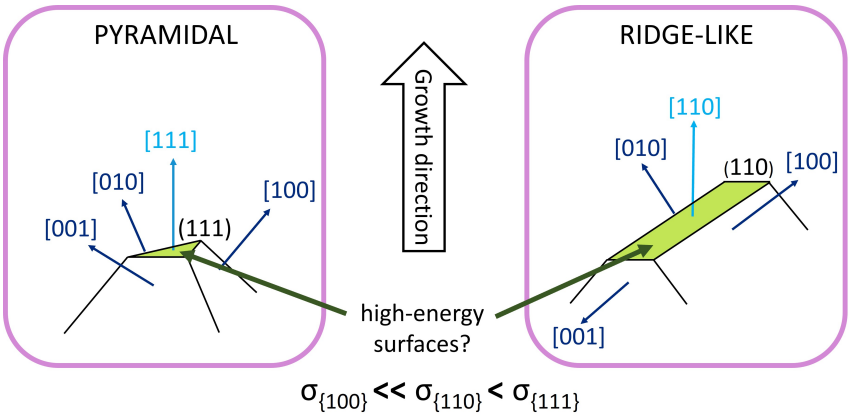

Figure 5.12: Schematics of the connection of the surface morphology to the grain orientation. The surface energy σ of the {100} facets is significantly lower than that of {110} and {111} facets [61]. If the top surface is flat, the truncation reveals high-energy surfaces.

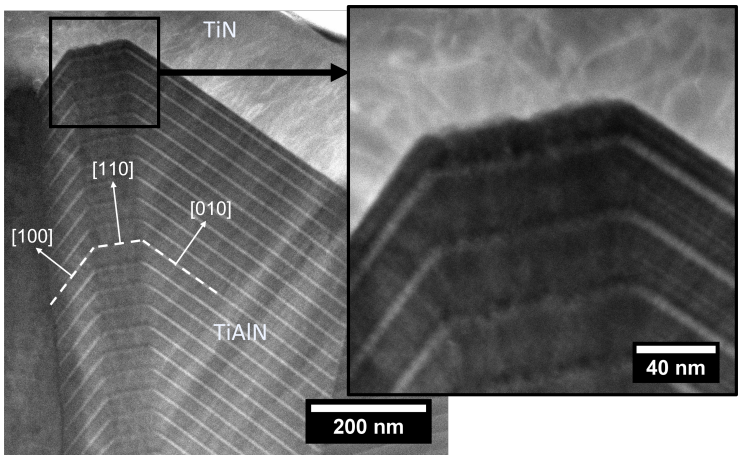

Figure 5.13: STEM HAADF image of a truncated ridge-like TiAlN grain. The lamellae in the core region appear more "fuzzy" and a closer look at the top of the grain (right image) shows that the surface displays small steps. Images taken by Olof Bäcke.

influencing the nucleation behaviour [36]. These special sites exist on the side {100} facets as well, yet, the density is increased substantially on the stepped surfaces revealed by the truncation, decreasing the diffusion paths to reach the special sites (illustrated in Figure 5.16b). In Figure 2.3 the fundamental processes during CVD were presented. The main gas flow and the transport to the surface are the essential processes that can limit the mass transport of the reactive precursor molecules to the surface [32]. Processes that contribute to the kinetics of the surface reaction include the adsorption as well as dissociation of the precursor and surface diffusion. Consequently, the surface kinetics on the surface displaying many small facets are enhanced. Previous results showed that the Ti deposition at moderate temperatures as in the present case is limited by the mass transport [18]. This means that the surface kinetics of Ti deposition are already faster than the rate of arrival of the

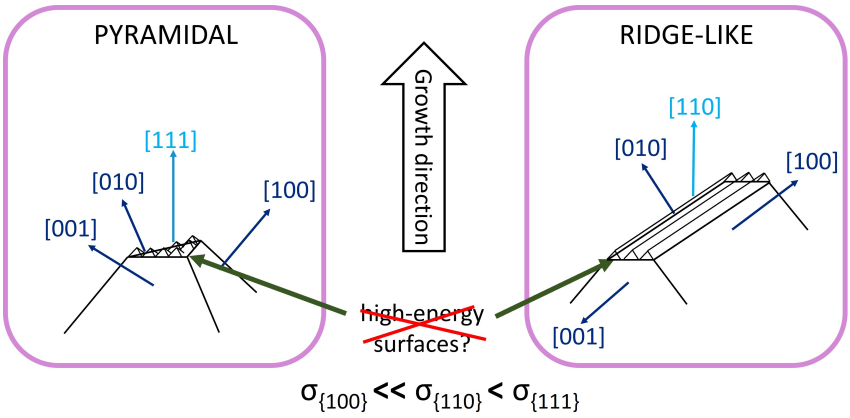

Figure 5.14: Schematics of the grain morphology, including grain orientation and smaller pyramids or ridges on the top surface where only {100} surfaces are present. The surface energy σ of the {100} facets is significantly lower than that of {110} and {111} facets [61].

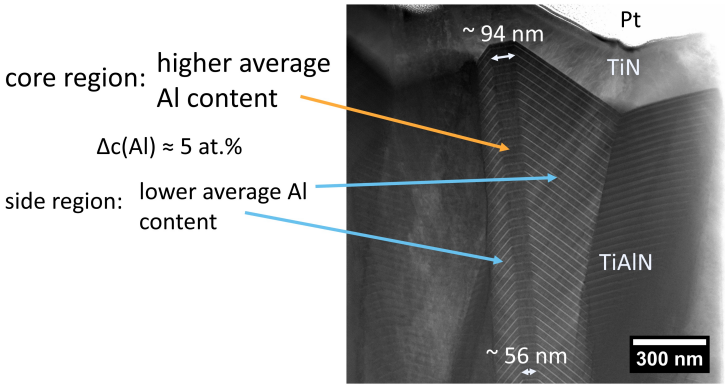

Figure 5.15: STEM HAADF image of a truncated ridge-like TiAlN grain. The Al content is higher in the core region, and the width of the core region increases along the growth direction. Image taken by Olof Bäcke.

Ti precursor at the surface, and the Ti deposition rate is not affected by enhanced surface kinetics. On the other hand, Al deposition is reported to be limited by surface kinetics [18]. Thus, the Al deposition rate is increased by the enhanced surface kinetics due to the increased density of special sites on the step-rich surface revealed by the truncation. The asymmetric change of deposition rate in the core region of a truncated grain is assumed to lead to an increase in Al/Ti ratio compared to the large {100} facets on the sides of the grains. Usually, fast-growing surfaces with high energy disappear [36], nevertheless, the surfaces revealed by the truncation even increase in size. An explanation for this observation is an increased lateral growth rate in addition to the increased growth rate in <110> or <111> direction due to the small facets, contributing to the stability of this growth mode.

Overall, the above can explain the increased Al/Ti ratio in the core region of a truncated grain. It serves to explain how this growth mode can be stable, where an additionally increased lateral growth rate leads to in increased width of the core

region. The growth mode leading to grain morphologies of truncated pyramids or ridges is the result of a distinct growth mechanism differing from the growth mechanism of those grains without truncation. Whether a grain shows a sharp or truncated morphology is most probably determined at very early stages of growth, and the growth mode does not divert later. It can be noted that it is rather typical in thin film deposition that the shape of grains is more facetted due to kinetical reasons than the thermodynamically most favoured Wulff shape [36]. If the above-made assumptions prove to be true, the presence of truncated grains is expected to decrease upon a relatively small increase of the temperature that increases the surface kinetics of the Al deposition.

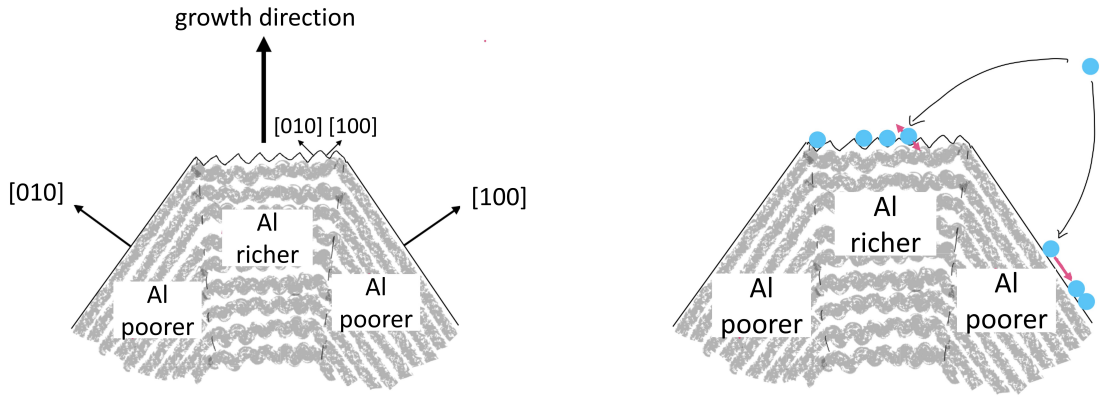

(a) (b)

Figure 5.16: (a) Schematic of a truncated grain. The overall growth direction can be [110] or [111], in the latter case the [100] direction is pointing outside the image plane. The distinctive features of a truncated grain are the small {100} facets on the top surface and large-area {100} facets on the sides, as well as a varying Al content. (b) Schematic of a truncated grain, illustrating the shorter diffusion paths to special sites where adsorption and/or dissociation are preferred [36].

5.3 Effects of Blast-Treatment on the Surface Region

In subsection 5.1.2 the surface morphology after blast-treatment was presented, and it was discussed that the observed surface morphology indicates substantial plastic deformation. This is further discussed in the following paragraphs, including STEM images as well as high-resolution TKD measurements of the surface region. STEM investigations of the nano-lamellar coatings with different periodicities were carried out, examples for each periodicity are presented in appendix A.5. In Table 5.2 the periodicities measured in STEM HAADF images are summarized. The average periodicity of the lowest and highest periodicity roughly match the expectations, yet, the medium periodicity deviates from the desired periodicity (on average 6.8 nm instead of 15 nm. Data retrieved by Walter from calotte grinding and cross-sectional SEM imaging suggests that a lamella periodicity of 15 ± 1.5 nm close to the nominal periodicity is achieved. By estimating the original coating thickness at the position of the cross-sectional lift out by adding $0.5 - 0.8$ µm to the coating thickness after blast-treatment on the thin-foil cross-section (compare to Figure 5.8) the locally expected periodicity can be calculated. Under the valid assumption that each gas rotation results in the formation of one lamella period, an expected lamella periodicity of about $10.8 - 11.5$ nm is calculated using a local coating thickness of $5.2 - 5.5$ µm and 480 gas rotations during the TiAlN deposition. Therefore, the lower periodicity can to some extent be explained by a locally decreased deposition rate, however, it does not completely explain the very low measured periodicity. To reveal additional reasons for the deviating behaviour of the present sample, further investigation is necessary that is not within the scope of this thesis. Generally, it is observed that all averaged periodicities exhibit a tendency to be smaller than the nominal value.

Table 5.2: Comparison of the expected lamella periodicity λ to the measured values in STEM HAADF images.

nominal λ_n [nm]	**6**	**15**	**50**
average λ_{avg} [nm]	4.9	6.8	48
standard deviation of λ_{avg} [nm]	0.4	0.6	9
min. λ_{min} [nm]	3.9	5.7	40
max. λ_{max} [nm]	5.7	8	72

Figure 5.17a shows the GOS of the grains in a thin foil cross-section determined by TKD. The GOS of those grains that reach the coating surface is systematically higher for those grains not reaching the coating surface. This vindicates that plastic deformation in the form of lattice rotations has been introduced as a result of blast-treatment and shows that mainly the uppermost region of the coating is affected. These lattice rotations are also evident in the GROD of the corresponding region in Figure 5.17b. There is a higher density of increased misorientation angles close

to the coating surface in all cases. Upon comparing the GROD plot of the filtered (Figure 5.17b) to the unfiltered data (Figure 5.17c), it becomes apparent that the employed filter tends to introduce substantial data within the near-surface region of the coating, where the amount of indexed pixels declines significantly. However, it is unclear how well the extrapolations of the filter represent the real scenario when applied to so limited data. Nevertheless, conclusions can be drawn from the worsening indexing in proximity to the surface of the coating. Firstly, it could be caused by the sample preparation. When preparing thin foils in a FIB-SEM, wedge-shaped specimens are frequently achieved due to the angles at which the ion milling is performed. This means that the prepared thin foils often show a decreasing thickness towards the top of the coating. The specimen thickness influences the pattern quality and spatial resolution of TKD [81]. High-quality patterns are likely within a range of $75-200\,\mathrm{nm}$ for Al and the range is expected to be lower in the case of elements with higher atomic numbers such as Ti. Therefore, it is not assumed that this scenario is the origin of degraded indexing in the near-surface region, as the thin foils were generally kept at thicknesses of $150-200\,\mathrm{nm}$ and it is not expected that the top region is critically thin. Instead, an increased defect density introducing disorder and disturbance of the periodicity of the lattice would lead to less clear Kikuchi bands that the analysis software has trouble with detecting and indexing.

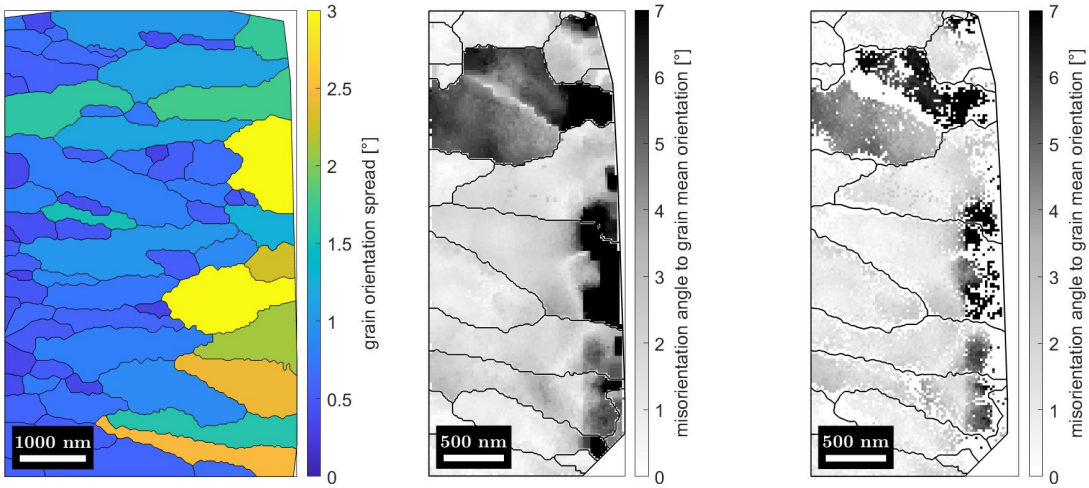

(a) (b) (c)

Figure 5.17: The sample surface is on the right in all images. (a) GOS of a thin foil cross-section based on a TKD measurement. The GOS is higher in those grains that reach the coating surface. (b) GROD determined from high-resolution TKD data of the surface region of the blast-treated coating. Data is denoised and missing data filled by filtering. High misorientation is found close to the coating surface. (c) GROD determined on raw data. Indexing worsens close to the coating surface.

In STEM BF overview imaging of the cross-sectional thin foils, as shown in Figure 5.18, lattice rotations and an increased defect density are observed as varying diffraction contrast in the near-surface region. Though it is difficult to quantify the depth of the affected region near the surface in the STEM BF image, because the

diffraction contrast varies strongly in this region as a result of the lattice rotations, a depth of a few hundred nanometres can be estimated. In order to determine if the different lamella periodicities influence this behaviour, the depth of the impacted region was measured from STEM BF images. The depth was estimated as shown by the blue line in Figure 5.18. This was performed on overview images of cross-sectional thin foils from regions with mainly 111 orientated grains of the three periodicities (the other corresponding images can be found in section A.6), the results are summarized in Figure 5.19. This rough estimation does not indicate any influence of the lamella periodicity on the impact depth with increased defect density and lattice rotations due to the blast-treatment.

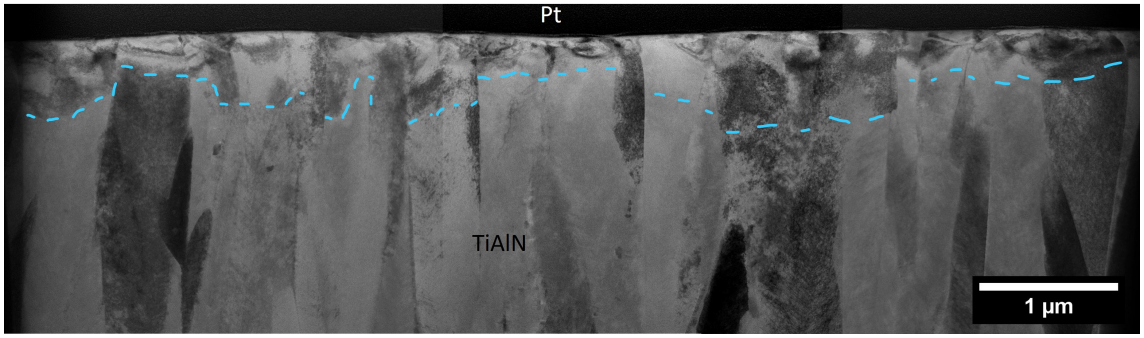

Figure 5.18: Overview STEM BF of a cross-sectional thin foil of a blast-treated sample (15_1_bltr). The estimated depth of the lattice rotations and increased defect density as a result of blast-treatment is indicated by the blue line.

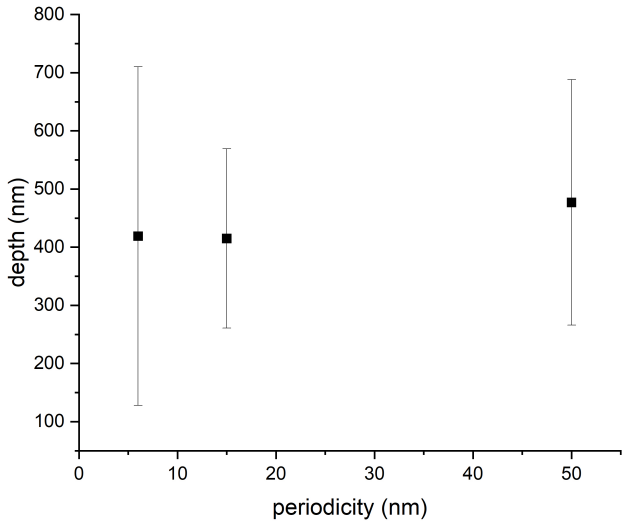

Figure 5.19: Estimated depth of the surface region affected by the blast-treatment vs the (expected) lamella periodicity. No correlation between the depth and the lamella periodicity is found.

A closer look at the strongly influenced near-surface region reveals further observations. Figure 5.20a shows the high defect density that was typically observed near the surface in the blast-treated samples. In Figure 5.20b the diffraction contrast reveals regions with strongly varying orientations, indicating void or crack formation beneath the surface, expected to result from top-blasting [65]. Theoretical considerations reveal that the maximum stress induced by a load is anticipated to occur beneath the surface [65], which aligns with the observations made in the present case, illustrated by Figure 5.20b. Furthermore, Figure 5.21 illustrates that the lattice rotations that are observed both from STEM BF images and TKD data are continuous. The FFTs in Figure 5.21a from the corresponding regions in the STEM BF images show the orientation along the $[1\,\bar{1}\,0]$ zone axis and how the lattice rotates continuously when moving along the grain. Only within this small selected region, a lattice rotation of about 7° is observed. In Figure 5.21b a single grain is selected and the orientation of each pixel along the marked line is plotted in an IPF. Again, the continuity of the lattice rotation is evident, additionally, rotation along all axes (x,y,z) of the specimen is illustrated. This is in contrast to a situation where slip happens along single slip planes, where discrete steps (slip traces) can be observed on the sample surface [82].

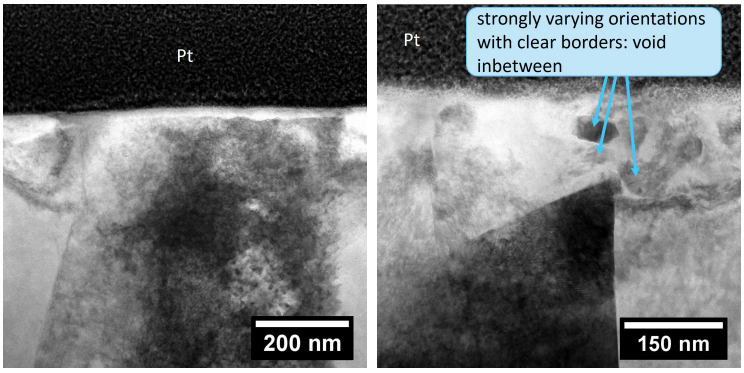

(a) (b)

Figure 5.20: Typical observations in the near-surface region of blast-treated samples by STEM BF imaging. (a) Increased defect density. (b) Void or crack formation.

When aligning individual grains to a zone axis orthogonal to their {100} planes, the behaviour of the alternating Ti- and Al-rich lamellae can be observed. Figure 5.22 shows examples of bending of lamellae close to the coating surface for all three lamella periodicities. Where the lamellae have moved from their original place, some mixing between the Ti- and Al-rich regions is observed. Because the deformation that occurred due to blast-treatment can be tracked with the help of the lamellae, a quantification of the induced strain can be done according to [83]. Equation 5.1 serves to calculate the strain $\overline{\delta}$ using the angle of the feature to the normal of the shear stress plane before deformation ζ and the angle of the feature to the normal of the shear stress plane after deformation θ. The illustration of the angles measured in the present case can be found in appendix A.7, angles of $\zeta = 72.5°$ and $\theta = 125.7°$ were determined, resulting in a compressive strain of 2.6. Yet, the

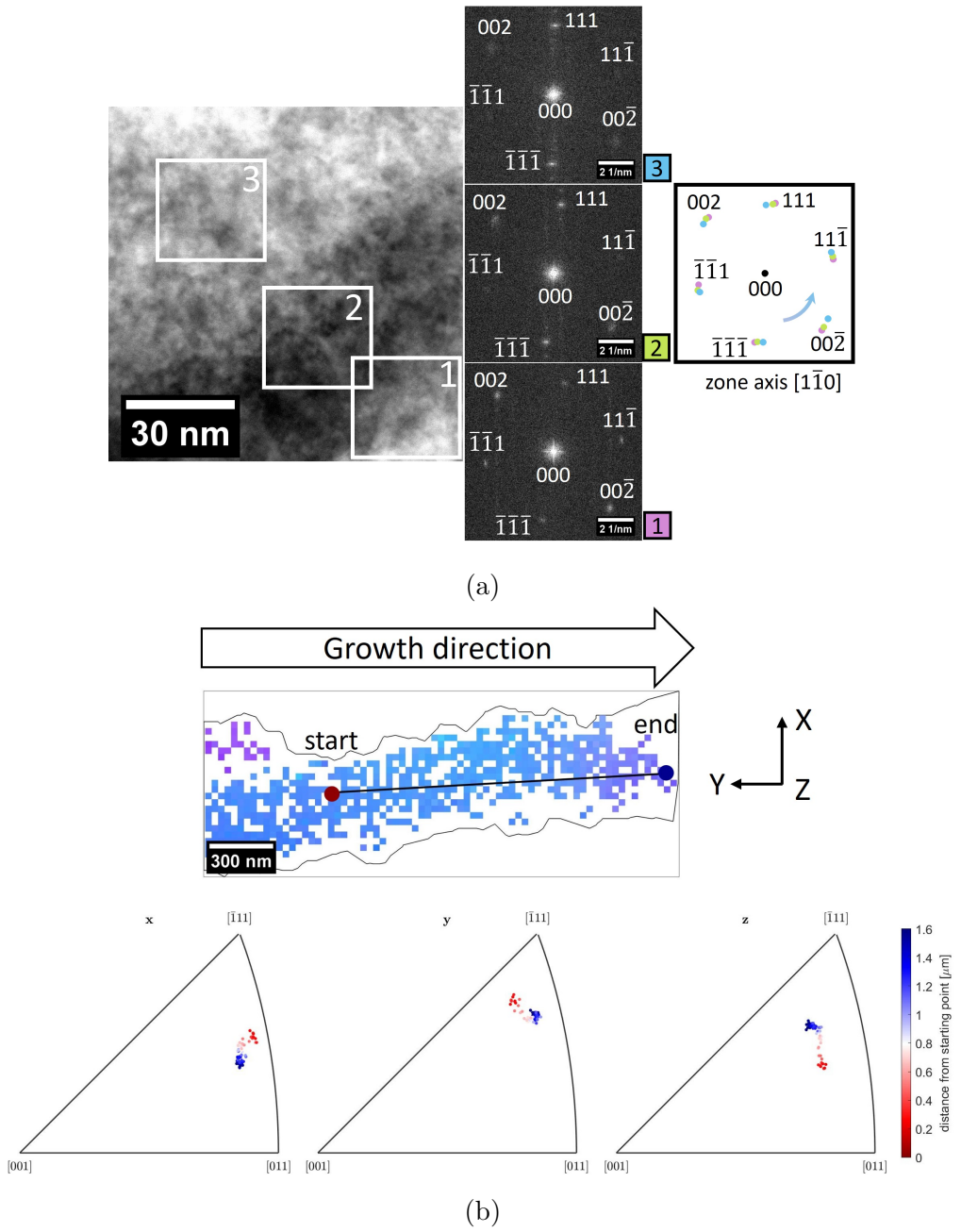

Figure 5.21: The lattice rotations due to blasting are continuous. (a) Lattice rotation of about 7° illustrated by FFTs performed at different positions on a STEM BF image. (b) Lattice rotation of a grain determined along the indicated line and illustrated in an IPF.

formula is derived from the assumption that the cross-section is perpendicular to the plane of the shear stress and simultaneously parallel to the shear stress [83]. While the first assumption is fulfilled in the present case, the latter is not, as was illustrated by changing directions of wear grooves in Figure 5.9b. Therefore, the quantification of the strain in the present case only serves as an estimation and wear tests with a defined shear direction would need to be done in order to study this in more detail.

$$\overline{\delta} = \left(1 - \frac{\tan\zeta}{\tan\theta}\right) \frac{\tan\theta}{\sqrt{3}} \tag{5.1}$$

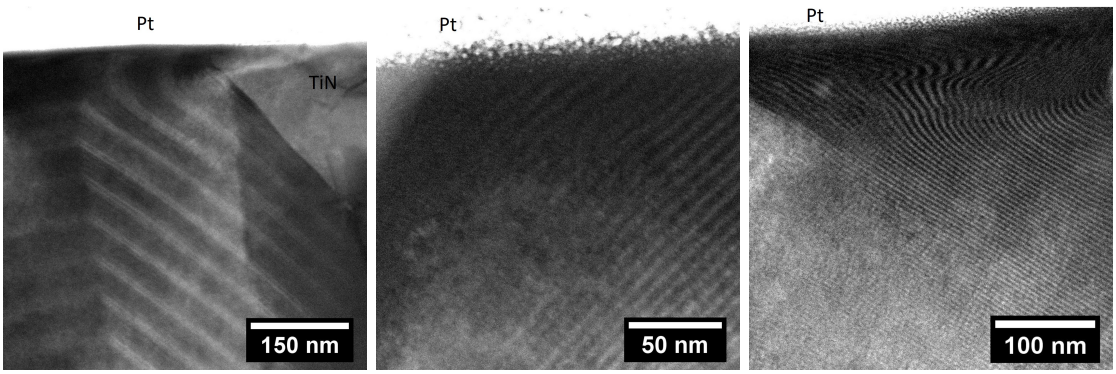

(a) (b) (c)

Figure 5.22: Bending of lamellae as a result of blast-treatment imaged by STEM HAADF. (a) Largest periodicity. (b) Medium periodicity. (c) Lowest periodicity.

In addition to bent lamellae, the disappearance of lamellae in the rotated lattice is observed, as presented in Figure 5.23. In Figure 5.23a lamellae are visible, however, they disappear in a region closer to the coating surface (marked by a blue line). During the investigation, a lattice rotation in this region could be identified with the help of Kikuchi lines. Kikuchi patterns enable the determination of the orientation of the electron beam relative to the crystal with high accuracy [71]. Therefore, the specimen was tilted (α-tilt of the TEM specimen stage) to investigate whether the lattice rotation preserved the lamellar arrangement, as the disappearance of visibility of the lamellae in the region where lattice rotation was present could also be due to a projection effect. The specimen was successfully tilted to achieve an orientation according to the lattice rotation, aligning it with the $[1\,\overline{1}\,0]$ zone axis orthogonal to the [100] growth direction of the lamellae. This is illustrated by the STEM BF images in Figure 5.23c, where darker regions indicate enhanced diffraction of the electrons which is due to the alignment at a zone axis, showing that the specimen was tilted in a way that the region where the lamellae disappeared (compare with the corresponding STEM HAADF images in Figure 5.23b) was now at zone axis. Despite these adjustments, the lamellae remained invisible, suggesting intermixing attributed to the effects of the blast-treatment.

In investigations on coatings of alternating TiAlN and CrN layers that were exposed to wear tests, Luo et al. [84] identified a region where the layers intermixed and another region where the layers were distorted. In their work, the intermixing was attributed to a locally increased temperature and therefore activated diffusion between the TiAlN and CrN layers in addition to plastic deformation. However, in the present case intermixing as a result of locally increased temperature is not assumed, as an increased temperature would lead to spinodal decomposition and

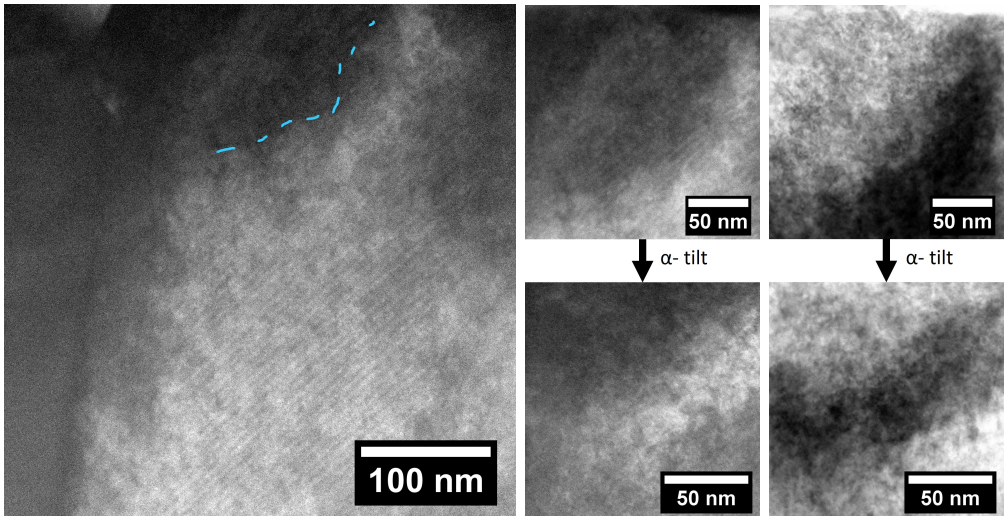

(a) (b) (c)

Figure 5.23: Disappearance of lamellae in the near-surface region strongly affected by the blast-treatment. (a) Lamellae visible in the STEM HAADF image disappear in the region indicated by a blue line. (b) While the lamellae were visible in STEM HAADF images in the less or not affected region, they disappear in the region that has undergone lattice rotations due to the blast-treatment. (c) STEM BF images illustrate how the applied specimen tilt (α-tilt of the specimen stage) follows the lattice rotation.

therefore a pronounced separation of a Ti- and an Al-rich phase [62, 55]. Additionally, the intermixing illustrated in Figure 5.23a is solely assigned to result from plastic deformation. Consequently, it is assumed that it is merely a more severe case of the examples where the plastic deformation could be traced by the distortion of the lamellar structure, as presented in Figure 5.22, indicating substantial strains. In those cases, it was observed that the lamellae were not only distorted in terms of disturbance of their original orientation but also initial intermixing. When the plastic deformation is not too pronounced, the nano-lamellar arrangement of Ti-rich and Al-rich regions in the present coatings provides a unique opportunity to track plastic deformation in detail.

In section 5.1 and 5.2 it was presented, that regions of grains with ridge-like morphology connected to a growth in <110> direction and regions of grains with pyramidal morphology connected to a growth in <111> direction existed. In Figure 5.24a and Figure 5.25a this can be observed as well: while Figure 5.24a shows primarily grains that grew along <111> directions, the majority of grains grew along <110> directions in Figure 5.25a and additional examples are presented in appendix A.8. When considering the maps of the GROD the maximum misorientation angle differentiated in the colour bar of the plot was manually chosen to illustrate the increased misorientation at the coating surface. Here, a too low maximum value would cause the whole plot to be very dark coloured, because some misorientation is present throughout the coating. If the maximum value is chosen too high, the misorientation is barely visible. When comparing those plots including grains with a preferred

orientation in a <111> direction to those with a preferred orientation in a <110> direction, the chosen maximum misorientation angle values for the colour bar are lower by about 3° in the case of <111> orientation than in the case of <110> orientation. Therefore, an increased lattice rotation as a result of blast-treatment is suggested for those grains with a preferred growth direction along their <110> directions compared to <111> directions. Yet, the chosen maximal misorientation angles were chosen subjectively. To improve the certainty of this suggestion, the experimental procedure should be improved with regard to an improved indexing capacity in the near-surface region of the coating and more measurements on <110> orientated grains should be performed to enhance statistics.

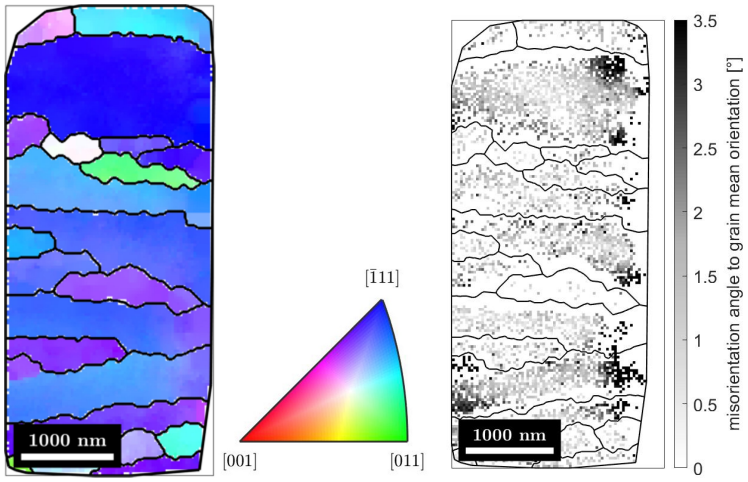

(a) (b)

Figure 5.24: The sample surface is on the right in both figures. (a) IPF orientation map shows a preferred orientation in <111> direction. (b) GROD determined from raw data. Indexing worsens close to the coating surface.

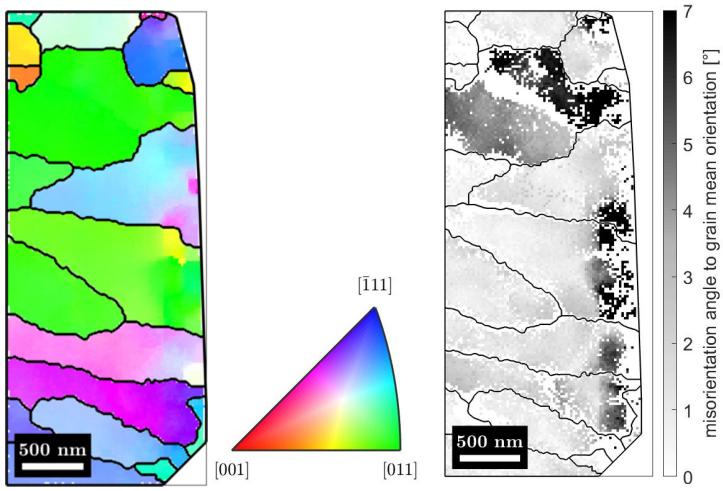

(a) (b)

Figure 5.25: The sample surface is on the right in both figures. (a) IPF orientation map shows a preferred orientation in <110> direction. (b) GROD determined from raw data. Indexing worsens close to the coating surface.

6

Summary and Conclusions

Within the scope of this thesis, the surface morphology of TiN/TiAlN/TiN coatings on cemented carbide substrates was studied in detail by SEM plan-view imaging. Two distinct surface morphologies could be observed: the previously reported pyramidal surface morphology [1] and an additional ridge-like surface morphology. By performing TKD measurements on thin foil cross-sections from positions which showed clear pyramidal or ridge-like surface morphology, the grain morphology could be assigned to a corresponding growth direction. The growth in a <111> direction in the case of pyramidal surface morphology was endorsed. Additionally, the ridge-like morphology could be assigned to growth along <110> directions. The two growth directions enable fast growth with low-energy {100} facets. In both cases, a truncated modification was reported. Applying the connection of the grain morphology to the growth direction, the surfaces revealed by truncation appear to be high-energy surfaces. However, small pyramids or ridges could be observed on the surface revealed by the truncation with small {100} facets which were then replicated and amplified by the growth of the TiN top layer.

In addition, the width of the core region of a truncated grain increased along the growth direction and a higher Al/Ti ratio in the core region was revealed by EDS. This was explained by enhanced surface reaction kinetics on the surface with many small facets resulting in increased adsorption and dissociation rates of the precursors as well as shorter diffusion paths. While the Ti deposition is assumed to be limited by mass transport and therefore not affected by an increased surface reaction rate, the Al deposition is accelerated, as it is limited by the surface reaction kinetics at the present moderate reaction temperatures. This leads to a slightly increased Al/Ti ratio in the region where many small facets are present in comparison to the side regions with larger {100} surfaces. An increased growth rate in the lateral direction explains the increasing width of the core region and the stability of this distinct growth mechanism. Mapping of the observed surface morphologies across the investigated substrates revealed no obvious connection to rotation speed and resulting nano-lamella periodicity or precursor gas flow direction. The observations and proposed growth mechanism of truncated grains contribute to the understanding of the growth and microstructure evolution of TiAlN coatings prepared by LPCVD, nevertheless, it remains unclear what drives the formation of the varying growth modes and directions. The very local variations suggest that the optimal deposition parameters for each growth mode are within a very narrow process window. Because the temperature is assumed to be constant within a relevant range (µm to mm), local flow conditions might be the cause for the variations.

Furthermore, the influence of blast-treatment with corundum particles on the TiAlN coatings was investigated. A near-surface region with increased defect density, crack or void formation and lattice rotations with a depth of a few hundred nanometres was evident. While the depth of the affected layer was not dependent on nano-lamella periodicity, a connection between the extent of lattice rotation due to blasting and the grain orientation was suggested. The nano-lamellae disappeared in some cases, yet, the bending of nano-lamellae was observed, providing a unique opportunity to follow the induced plastic deformation. FFTs of STEM BF images as well as TKD data implied continuous large lattice rotations in three dimensions.

A continuation of the presented work could include investigations on the driving force for the varying surface morphologies. The effect of a slight increase in deposition temperature on the presence of truncated TiAlN grains would help in understanding and validating the proposed growth mechanism. Investigations of the orientation relationships between the bottom TiN and the TiAlN layers could give insight into the reason for the appearance of larger regions of one growth direction instead of a random distribution. Further simulations of the precursor gas flow by computational fluid dynamics could contribute to this as well if the driving force for different orientations is related to the growth rate. This gains relevance when considering that more pronounced lattice rotations as a result of blast-treatment were observed for <110> orientated grains in comparison to <111> orientated grains, which might denote varying performance for differently textured coatings. In order to achieve more detailed information on the lattice rotations in the near-surface region, further work on optimizing the TKD measurements or alternatively precession electron diffraction measurements can be performed. Additionally, the wear and resulting plastic deformation could be studied in more detail by performing wear tests with a defined shear stress direction and taking advantage of the unique opportunity provided by the nano-lamellae of alternating composition to track the plastic deformation in detail. Overall, connecting the findings to diffraction data (e.g. synchrotron XRD) giving insight into the stress state as well as mechanical properties would contribute to closing the knowledge gap between structure and resulting properties leading to the possibility to tailor the properties of TiAlN coatings by tuning of the CVD process and post-treatment parameters to achieve better performing cutting tools.

Bibliography

[1] R. Qiu, O. Bäcke, D. Stiens, W. Janssen, J. Kümmel, T. Manns, H.-O. Andrén, and M. Halvarsson. "CVD TiAlN coatings with tunable nanolamella architectures". In: *Surface and Coatings Technology* 413 (2021), p. 127076. DOI: 10.1016/j.surfcoat.2021.127076.

[2] Fritz Klocke. *Fertigungsverfahren 1: Zerspanung mit geometrisch bestimmter Schneide*. 9. Auflage 2018. VDI-Buch. Berlin, Heidelberg: Springer Berlin Heidelberg, 2018. ISBN: 9783662542071.

[3] Dedalus Consulting. *N.N. Cutting Tools*. 2014. URL: https://www.dedalusconsulting.com/ (visited on 04/03/2023).

[4] Mitsubishi Materials. *CuttingTool Materials*. 2023. URL: https://www.mmc-carbide.com/en_jp/technical_information/tec_other_data/tec_other_data_top/tec_other_data_technical/tec_cutting_tool_materials (visited on 07/05/2023).

[5] Kirsten Bobzin. "High-performance coatings for cutting tools". In: *CIRP Journal of Manufacturing Science and Technology* 18 (2017), pp. 1–9. DOI: 10.1016/j.cirpj.2016.11.004.

[6] M. R. Derakhshandeh, M. J. Eshraghi, and M. Razavi. "Recent developments in the new generation of hard coatings applied on cemented carbide cutting tools". In: *International Journal of Refractory Metals and Hard Materials* 111 (2023), p. 106077. DOI: 10.1016/j.ijrmhm.2022.106077.

[7] Kapil Gupta, R. F. Laubscher, J. Paulo Davim, and N. K. Jain. "Recent developments in sustainable manufacturing of gears: a review". In: *Journal of Cleaner Production* 112 (2016), pp. 3320–3330. DOI: 10.1016/j.jclepro.2015.09.133.

[8] Anuj Kumar Sharma, Arun Kumar Tiwari, and Amit Rai Dixit. "Effects of Minimum Quantity Lubrication (MQL) in machining processes using conventional and nanofluid based cutting fluids: A comprehensive review". In: *Journal of Cleaner Production* 127 (2016), pp. 1–18. DOI: 10.1016/j.jclepro.2016.03.146.

[9] Bruce L. Tai, David A. Stephenson, Richard J. Furness, and Albert J. Shih. "Minimum Quantity Lubrication (MQL) in Automotive Powertrain Machining". In: *Procedia CIRP* 14 (2014), pp. 523–528. DOI: 10.1016/j.procir.2014.03.044.

[10] VDI-Gesellschaft Materials Engineering. *VDI Studie Werkstoffinnovationen für nachhaltige Mobilität und Energieversorgung*. 2013. URL: https://www.vdi.de/ueber-uns/presse/publikationen/details/werkstoffinnovatio

nen-fuer-nachhaltige-mobilitaet-und-energieversorgung (visited on 04/03/2023).

[11] Konstantinos-Dionysios Bouzakis, Nikolaos Michailidis, Georgios Skordaris, Emmanouil Bouzakis, Dirk Biermann, and Rachid M'Saoubi. "Cutting with coated tools: Coating technologies, characterization methods and performance optimization". In: *CIRP Annals* 61.2 (2012), pp. 703–723. DOI: 10.1016/j.cirp.2012.05.006.

[12] R. F. Bunshah. *Handbook of hard coatings: Deposition technologies, properties and applications*. Materials science and processing technology series. Park Ridge, N.J. and Norwich, N.Y.: Noyes Publications and William Andrew Pub, 2001. ISBN: 0-8155-1438-7.

[13] Aharon Inspektor and Paul A. Salvador. "Architecture of PVD coatings for metalcutting applications: A review". In: *Surface and Coatings Technology* 257 (2014), pp. 138–153. DOI: 10.1016/j.surfcoat.2014.08.068.

[14] P.C Jindal, A.T Santhanam, U. Schleinkofer, and A.F Shuster. "Performance of PVD TiN, TiCN, and TiAlN coated cemented carbide tools in turning". In: *International Journal of Refractory Metals and Hard Materials* 17.1-3 (1999), pp. 163–170. DOI: 10.1016/S0263-4368(99)00008-6.

[15] J. H. Hsieh, A.L.K. Tan, and X. T. Zeng. "Oxidation and wear behaviors of Ti-based thin films". In: *Surface and Coatings Technology* 201.7 (2006), pp. 4094–4098. DOI: 10.1016/j.surfcoat.2006.08.026.

[16] T. Leyendecker, O. Lemmer, S. Esser, and J. Ebberink. "The development of the PVD coating TiAlN as a commercial coating for cutting tools". In: *Surface and Coatings Technology* 48.2 (1991), pp. 175–178. DOI: 10.1016/0257-8972(91)90142-J.

[17] C. Czettl, U. Schleinkofer, F. Schedle, C. Wolf, M. Lechleitner, H. Holzschuh, and W. Bürgin. "CVD TiAlN - Development and Challenges for Use in Mass Production". In: (May 29–June 2, 2017). Reutte, Austria: Plansee Group, 2017, HM45/1–HM45/2.

[18] Ren Qiu, Axel Forslund, Olof Bäcke, Anand.H.S. Iyer, Mohammad Sattari, Wiebke Janssen, Thorsten Manns, Johannes Kümmel, Andrei Ruban, Dirk Stiens, Hans-Olof Andrén, and Mats Halvarsson. "Effects of gas flow on detailed microstructure inhomogeneities in LPCVD TiAlN nanolamella coatings". In: *Materialia* 9 (2020), p. 100546. DOI: 10.1016/j.mtla.2019.100546.

[19] Min Zhou, Y. Makino, M. Nose, and K. Nogi. "Phase transition and properties of Ti–Al–N thin films prepared by r.f.-plasma assisted magnetron sputtering". In: *Thin Solid Films* 339.1-2 (1999), pp. 203–208. DOI: 10.1016/S0040-6090(98)01364-9.

[20] I. Endler, M. Höhn, M. Herrmann, R. Pitonak, S. Ruppi, M. Schneider, H. van den Berg, and H. Westphal. "Novel aluminum-rich Ti1−xAlxN coatings by LPCVD". In: *Surface and Coatings Technology* 203.5-7 (2008), pp. 530–533. DOI: 10.1016/j.surfcoat.2008.04.098.

[21] J. Todt, J. Zalesak, R. Daniel, R. Pitonak, A. Köpf, R. Weißenbacher, B. Sartory, C. Mitterer, and J. Keckes. "Al-rich cubic Al0.8Ti0.2N coating with self-organized nano-lamellar microstructure: Thermal and mechanical proper-

ties". In: *Surface and Coatings Technology* 291 (2016), pp. 89–93. DOI: 10.1016/j.surfcoat.2016.02.027.

[22] Yanhui Zhang, Peter Franke, and Hans Jürgen Seifert. "CALPHAD modeling of metastable phases and ternary compounds in Ti-Al-N system". In: *Calphad* 59 (2017), pp. 142–153. DOI: 10.1016/j.calphad.2017.09.006.

[23] J. Zalesak, D. Holec, I. Matko, M. Petrenec, B. Sartory, N. Koutná, R. Daniel, R. Pitonak, and J. Keckes. "Peculiarity of self-assembled cubic nanolamellae in the TiN/AlN system: Epitaxial self-stabilization by element deficiency/excess". In: *Acta Materialia* 131 (2017), pp. 391–399. DOI: 10.1016/j.actamat.2017.04.009.

[24] K.-D. Bouzakis, E. Bouzakis, G. Skordaris, S. Makrimallakis, A. Tsouknidas, G. Katirtzoglou, and S. Gerardis. "Effect of PVD films wet micro-blasting by various Al2O3 grain sizes on the wear behaviour of coated tools". In: *Surface and Coatings Technology* 205 (2011), S128–S132. DOI: 10.1016/j.surfcoat.2011.03.046.

[25] Martina Gassner, Nina Schalk, Michael Tkadletz, Christoph Czettl, and Christian Mitterer. "Thermal crack network on CVD TiCN/α-Al2O3 coated cemented carbide cutting tools". In: *International Journal of Refractory Metals and Hard Materials* 81 (2019), pp. 1–6. DOI: 10.1016/j.ijrmhm.2019.02.006.

[26] Tongwei Shen, Lihui Zhu, and Zhenyu Liu. "Effect of micro-blasting on the tribological properties of TiN/MT-TiCN/Al2O3/TiCNO coatings deposited by CVD". In: *International Journal of Refractory Metals and Hard Materials* 88 (2020), p. 105205. DOI: 10.1016/j.ijrmhm.2020.105205.

[27] M. Tkadletz, J. Keckes, N. Schalk, I. Krajinovic, M. Burghammer, C. Czettl, and C. Mitterer. "Residual stress gradients in α-Al2O3 hard coatings determined by pencil-beam X-ray nanodiffraction: The influence of blasting media". In: *Surface and Coatings Technology* 262 (2015), pp. 134–140. DOI: 10.1016/j.surfcoat.2014.12.028.

[28] Zhi-Qiang Zhong, Li Zhang, Lei Zhou, Lian-Chang Qiu, Hai-Dong Shi, Man-Li Yang, and Ji-Fei Zhu. "Cutting performances and the related characteristics of CVD coated hardmetal inserts changed by post-treatments". In: *International Journal of Refractory Metals and Hard Materials* 70 (2018), pp. 162–168. DOI: 10.1016/j.ijrmhm.2017.10.003.

[29] C. Liu, Z. Liu, and B. Wang. "Modification of surface morphology to enhance tribological properties for CVD coated cutting tools through wet micro-blasting post-process". In: *Ceramics International* 44.3 (2018), pp. 3430–3439. DOI: 10.1016/j.ceramint.2017.11.142.

[30] S. Tanaka, T. Shirochi, H. Nishizawa, K. Metoki, H. Miura, H. Hara, and T. Takahashi. "Micro-blasting effect on fracture resistance of PVD-AlTiN coated cemented carbide cutting tools". In: *Surface and Coatings Technology* 308 (2016), pp. 337–340. DOI: 10.1016/j.surfcoat.2016.07.094.

[31] K. -D. Bouzakis, A. Tsouknidas, G. Skordaris, E. Bouzakis. "Optimization of Wet or Dry Micro-blasting on PVD Films by Various Al2O3 Grain Sizes for Improving the Coated Tools' Cutting Performance". In: *Tribology in Industry* 33.2 (2011), pp. 49–56.

[32] Anthony C. Jones and Michael L. Hitchman. *Chemical vapour deposition: Precursors, processes and applications*. Cambridge, UK: Royal Society of Chemistry, 2009. ISBN: 978-1-84755-879-4.

[33] J. M. Albella, I Jiménez, C. Gómez-Aleixandre, A. Alberdi. "Materials and vapour-phase techniques for the synthesis of ceramic coating". In: *Boletín de la Sociedad Española de Cerámica y Vidrio* 46.4 (2007), pp. 171–176.

[34] M.R. Leys. "Metal organic vapour phase epitaxy". In: *Chemtronics* 2.4 (1987), pp. 155–164.

[35] Anthony C. Jones and Paul O'Brien. *CVD of Compound Semiconductors*. Wiley, 1997. ISBN: 9783527292943.

[36] J. A. Venables, G. D. T. Spiller, and M. Hanbucken. "Nucleation and growth of thin films". In: *Reports on Progress in Physics* 47.4 (1984), pp. 399–459. DOI: 10.1088/0034-4885/47/4/002.

[37] A Van der Drift. "Evolutionary selection, a principle governing growth orientation in vapour-deposited layers". In: *Philips Res. Rep* 22.3 (1967), p. 267.

[38] Udo W. Pohl. *Epitaxy of Semiconductors: Introduction to Physical Principles*. Graduate Texts in Physics. Berlin, Heidelberg: Springer, 2013. ISBN: 978-3-642-32970-8.

[39] A. Stoffel, A. Kovács, W. Kronast, and B. Müller. "LPCVD against PECVD for micromechanical applications". In: *Journal of Micromechanics and Microengineering* 6.1 (1996), pp. 1–13. DOI: 10.1088/0960-1317/6/1/001.

[40] Universität Tübingen LISA+. *Chemische Gasphasenabscheidung*. URL: https://uni-tuebingen.de/forschung/forschungsinfrastruktur/lisa/einrichtungen/duennfilmdeposition/chemische-gasphasenabscheidung/ (visited on 05/22/2023).

[41] O. Oluwatosin Abegunde, E. Titilayo Akinlabi, O. Philip Oladijo, S. Akinlabi, and A. Uchenna Ude. "Overview of thin film deposition techniques". In: *AIMS Materials Science* 6.2 (2019), pp. 174–199. DOI: 10.3934/matersci.2019.2.174.

[42] Yasaman Hamedani, Prathyushakrishna Macha, Timothy J. Bunning, Rajesh R. Naik, and Milana C. Vasudev. "Plasma-Enhanced Chemical Vapor Deposition: Where we are and the Outlook for the Future". In: *Chemical Vapor Deposition - Recent Advances and Applications in Optical, Solar Cells and Solid State Devices*. Ed. by Sudheer Neralla. InTech, 2016. ISBN: 978-953-51-2572-3.

[43] Erich Wintermantel and Suk-Woo Ha. *Medizintechnik: Life science engineering : Interdisziplinaritt, Biokompatibilitt, Technologien, Implantate, Diagnostik, Werkstoffe, Zertifizierung, Business*. 5., überarbeitete und erw. Aufl. Berlin: Springer, 2009. ISBN: 978-3-540-93936-8.

[44] Shuho Koseki, Kenichi Inoue, Shigekazu Morito, Takuya Ohba, and Hiroshi Usuki. "Comparison of TiN-coated tools using CVD and PVD processes during continuous cutting of Ni-based superalloys". In: *Surface and Coatings Technology* 283 (2015), pp. 353–363. DOI: https://doi.org/10.1016/j.surfcoat.2015.10.071.

[45] Sameh Dabees, Saeed Mirzaei, Pavel Kaspar, Vladimír Holcman, and Dinara Sobola. "Characterization and Evaluation of Engineered Coating Techniques

for Different Cutting Tools-Review". In: *Materials (Basel, Switzerland)* 15.16 (2022). DOI: 10.3390/ma15165633.

[46] Yuya Kajikawa. "Roughness evolution during chemical vapor deposition". In: *Materials Chemistry and Physics* 112.2 (2008), pp. 311–318. DOI: 10.1016/j.matchemphys.2008.06.008.

[47] B. Alling, A. V. Ruban, A. Karimi, O. E. Peil, S. I. Simak, L. Hultman, and I. A. Abrikosov. "Mixing and decomposition thermodynamics of c−Ti1−xAlxN from first-principles calculations". In: *Physical Review B* 75.4 (2007). DOI: 10.1103/PhysRevB.75.045123.

[48] Ingolf Endler, Mandy Höhn, Björn Matthey, Jakub Zálešák, Jozef Keckes, and Reinhard Pitonak. "Powder Diffraction Data of Aluminum-Rich FCC-Ti1−xAlxN Prepared by CVD". In: *Coatings* 11.6 (2021), p. 683. DOI: 10.3390/coatings11060683.

[49] A. R. Denton and N. W. Ashcroft. "Vegard's law". In: *Physical review. A, Atomic, molecular, and optical physics* 43.6 (1991), pp. 3161–3164. DOI: 10.1103/PhysRevA.43.3161.

[50] S. Gates-Rector and T. Blanton. "The Powder Diffraction File: A Quality Materials Characterization Database". In: *Powder Diffraction* 34.4 (2019), pp. 352–360. DOI: 10.1017/S0885715619000812.

[51] Nina Shulumba, Olle Hellman, Zamaan Raza, Björn Alling, Jenifer Barrirero, Frank Mücklich, Igor A. Abrikosov, and Magnus Odén. "Lattice Vibrations Change the Solid Solubility of an Alloy at High Temperatures". In: *Physical review letters* 117.20 (2016), p. 205502. DOI: 10.1103/PhysRevLett.117.205502.

[52] David R. Gaskell. *Introduction to the thermodynamics of materials*. Fifth edition. New York: Taylor & Francis, 2012. ISBN: 0-203-42849-8.

[53] M. Hillert. "A solid-solution model for inhomogeneous systems". In: *Acta Metallurgica* 9.6 (1961), pp. 525–535. DOI: 10.1016/0001-6160(61)90155-9.

[54] Katherine M. Calamba. *Phase Stability and Defect Structures in (Ti,Al)N Hard Coatings*. Vol. v.1996. Linköping University Medical Dissertations Ser. Linköping: Linkopings Universitet, 2019. ISBN: 978-91-7685-041-1.

[55] R. F. Zhang and S. Veprek. "Metastable phases and spinodal decomposition in Ti1−xAlxN system studied by ab initio and thermodynamic modeling, a comparison with the TiN–Si3N4 system". In: *Materials Science and Engineering: A* 448.1-2 (2007), pp. 111–119. DOI: 10.1016/j.msea.2006.10.012.

[56] Ren Qiu. *Microstructural investigation of CVD TiAlN, Tin and WN coatings*. Vol. 5009. Doktorsavhandlingar vid Chalmers tekniska högskola. Ny serie. Göteborg: Chalmers University of Technology, 2021. ISBN: 978-91-7905-542-4.

[57] Momoko Deura, Hiroki Sato, Jun Yamaguchi, Tomoko Hirabaru, Hayato Kubo, Takeshi Momose, Takahito Tanibuchi, and Yukihiro Shimogaki. "Kinetic analysis of face-centered-cubic Ti1−Al N film deposition by chemical vapor deposition". In: *Materials Science and Engineering: B* 264 (2021), p. 114992. DOI: 10.1016/j.mseb.2020.114992.

[58] Soham Das, Spandan Guha, Ranjan Ghadai, Dhruva Kumar, and Bibhu P. Swain. "Structural and mechanical properties of CVD deposited titanium alu-

minium nitride (TiAlN) thin films". In: *Applied Physics A* 123.6 (2017). DOI: 10.1007/s00339-017-1032-0.

[59] Mohamed Ben Hassine, Hans-Olof Andrén, Anand H.S. Iyer, Antiope Lotsari, Olof Bäcke, Dirk Stiens, Wiebke Janssen, Thorsten Manns, Johannes Kümmel, and Mats Halvarsson. "Growth model for high-Al containing CVD TiAlN coatings on cemented carbides using intermediate layers of TiN". In: *Surface and Coatings Technology* 421 (2021), p. 127361. DOI: 10.1016/j.surfcoat.2021.127361.

[60] J. Keckes, R. Daniel, C. Mitterer, I. Matko, B. Sartory, A. Koepf, R. Weißenbacher, and R. Pitonak. "Self-organized periodic soft-hard nanolamellae in polycrystalline TiAlN thin films". In: *Thin Solid Films* 545 (2013), pp. 29–32. DOI: 10.1016/j.tsf.2013.08.001.

[61] Axel Forslund and Andrei Ruban. "Surface energetics of AlxTi1-xN alloys". In: *Computational Materials Science* 183 (2020), p. 109813. DOI: 10.1016/j.commatsci.2020.109813.

[62] M. Tkadletz, A. Lechner, N. Schalk, B. Sartory, A. Stark, N. Schell, C. Saringer, C. Mitterer, and C. Czettl. "Influence of spinodal decomposition and fcc→w phase transformation on global and local mechanical properties of nanolamellar CVD fcc-Ti1-xAlxN coatings". In: *Materialia* 11 (2020), p. 100696. DOI: 10.1016/j.mtla.2020.100696.

[63] Ren Qiu, Hisham Aboulfadl, Olof Bäcke, Dirk Stiens, Hans-Olof Andrén, and Mats Halvarsson. "Atom probe tomography investigation of 3D nanoscale compositional variations in CVD TiAlN nanolamella coatings". In: *Surface and Coatings Technology* 426 (2021), p. 127741. DOI: 10.1016/j.surfcoat.2021.127741.

[64] M. Tkadletz, C. Hofer, C. Wüstefeld, N. Schalk, M. Motylenko, D. Rafaja, H. Holzschuh, W. Bürgin, B. Sartory, C. Mitterer, and C. Czettl. "Thermal stability of nanolamellar fcc-Ti1-xAlxN grown by chemical vapor deposition". In: *Acta Materialia* 174 (2019), pp. 195–205. DOI: 10.1016/j.actamat.2019.05.044.

[65] Horst Czichos and Karl-Heinz Habig. *Tribologie-Handbuch*. Vieweg+Teubner, 2010. ISBN: 978-3-8348-0017-6.

[66] C. Barbatti, J. Garcia, R. Pitonak, H. Pinto, A. Kostka, A. Di Prinzio, M. H. Staia, and A. R. Pyzalla. "Influence of micro-blasting on the microstructure and residual stresses of CVD κ-Al2O3 coatings". In: *Surface and Coatings Technology* 203.24 (2009), pp. 3708–3717. DOI: 10.1016/j.surfcoat.2009.06.021.

[67] Carl Björmander. "A coated cutting tool". European pat. EP 3 872 222. 2020.

[68] Joseph I. Goldstein. *Scanning electron microscopy and x-ray microanalysis*. 3. ed. New York: Springer, 2013. ISBN: 978-1-4613-4969-3.

[69] Ludwig Reimer. *Scanning electron microscopy: Physics of image formation and microanalysis*. Vol. v. 45. Springer series in optical sciences. Berlin and New York: Springer-Verlag, 1985. ISBN: 978-3-662-13564-8.

[70] Lucille A. Giannuzzi. *Introduction to Focused Ion Beams: Instrumentation, Theory, Techniques and Practice*. Boston, MA: Springer Science+Business Media, Inc, 2005. ISBN: 978-0-387-23313-0.

[71] David Bernard Williams and C. Barry Carter. *Transmission electron microscopy: A textbook for materials science*. 2nd ed. New York: Springer, 2009. ISBN: 978-0-387-76501-3.

[72] R. R. Keller and R. H. Geiss. "Transmission EBSD from 10 nm domains in a scanning electron microscope". In: *Journal of Microscopy* 245.3 (2012), pp. 245–251. DOI: 10.1111/j.1365-2818.2011.03566.x.

[73] Oxford Instruments. *Electron Backscatter Diffraction (EBSD) Geometry*. 2023. URL: https://www.ebsd.com/hints-and-tips/ebsd-geometry (visited on 04/24/2023).

[74] "Grain detection from 2d and 3d EBSD data–specification of the MTEX algorithm". In: *Ultramicroscopy* 111.12 (2011), pp. 1720–1733. DOI: 10.1016/j.ultramic.2011.08.002.

[75] G. Nolze and R. Hielscher. "Orientations – perfectly colored". In: *Journal of Applied Crystallography* 49.5 (2016), pp. 1786–1802. DOI: 10.1107/S1600576716012942.

[76] Fabian Bartl. *Grain Reference Orientation Deviation (GROD)*. URL: https://fabianbartl.github.io/mtex-toolbox/EBSDGROD.html (visited on 07/01/2023).

[77] Gabriele Steidl, Johannes Persch, Ralf Hielscher, Raymond Chan, and Ronny Bergmann. "Restoration of manifold-valued images by half-quadratic minimization". In: *Inverse Problems and Imaging* 10.2 (2016), pp. 281–304. DOI: 10.3934/ipi.2016001.

[78] Adam J. Schwartz, Mukul Kumar, and Brent L. Adams. *Electron Backscatter Diffraction in Materials Science*. 2nd ed. Boston, MA: Springer US, 2009. ISBN: 978-0-387-88135-5.

[79] Ludwig Reimer and Helmut Kohl. *Transmission Electron Microscopy: Physics of Image Formation*. 6., ed. Vol. 36. Springer series in optical sciences. New York, NY: Springer Verlag New York, 2004. ISBN: 978-0-387-40093-8.

[80] Marc A. Meyers and Krishan K. Chawla. *Mechanical behavior of materials*. 2a ed. Upper Saddle River, N.J.: Prentice Hall, 2009. ISBN: 978-0-521-86675-0.

[81] Glenn C. Sneddon, Patrick W. Trimby, and Julie M. Cairney. "Transmission Kikuchi diffraction in a scanning electron microscope: A review". In: *Materials Science and Engineering: R: Reports* 110 (2016), pp. 1–12. DOI: 10.1016/j.mser.2016.10.001.

[82] Ryan Sperry, Songyang Han, Zhe Chen, Samantha H. Daly, Martin A. Crimp, and David T. Fullwood. "Comparison of EBSD, DIC, AFM, and ECCI for active slip system identification in deformed Ti-7Al". In: *Materials Characterization* 173 (2021), p. 110941. DOI: 10.1016/j.matchar.2021.110941. URL: https://www.sciencedirect.com/science/article/pii/S1044580321000711.

[83] J. H. Dautzenberg and J. H. Zaat. "Quantitative determination of deformation by sliding wear". In: *Wear* 23.1 (1973), pp. 9–19. DOI: 10.1016/0043-1648(73)90036-7.

[84] Q. Luo, W.M Rainforth, and W.-D Münz. "TEM studies of the wear of TiAlN/CrN superlattice coatings". In: *Scripta Materialia* 45.4 (2001), pp. 399–404. DOI: 10.1016/S1359-6462(01)01018-1.

A

Appendix

A.1 Reference Diffraction Data TiAlN

a [Å]			4.09418
Al			75
Ti			25
N			100
h	**k**	**l**	**reference intensity** Powdercell BB-Geo, FWHM = f(u,v,w)
1	1	1	37,67
2	0	0	100,00
2	2	0	56,26
3	1	1	17,48
2	2	2	17,82
4	0	0	9,08
3	3	1	9,81
4	2	0	33,63
4	2	2	42,09
5	1	1	20,91
3	3	3	6,97

A.2 MTEX Code: Analysis of TKD Data

```
%% Specify Crystal and Specimen Symmetries

LAGB = 2*degree;
HAGB = 10*degree;
```

```
% crystal symmetry of TiAlN
CS = {...
  'notIndexed',...
  crystalSymmetry('m-3m', [4.1e+14 4.1e+14 4.1e+14],...
  'mineral', 'Ti3AlN', 'color', [0.53 0.81 0.98])};

% plotting convention
setMTEXpref('xAxisDirection','north');
setMTEXpref('zAxisDirection','outOfPlane');
```

```
%% Specify File Names

% path to files
pname = 'C:\mtex-5.9.0\mtex-5.9.0';

% which files to be imported
fname = ['C:\mtex-5.9.0\mtex-5.9.0\filename.cpr'];
```

```
%% Import the Data

% create an EBSD variable containing the data
ebsd = EBSD.load(fname,CS,'interface','crc',...
  'convertEuler2SpatialReferenceFrame');

% reconstruct the grain structure
    [grains,ebsd('indexed').grainId,...
        ebsd('indexed').mis2mean] ...
    = calcGrains(ebsd('indexed'),'threshold',[LAGB HAGB]);
    % removing all grains smaller than 5 pixels
    ebsd(grains(grains.grainSize<=5)) = [];
   [grains,ebsd('indexed').grainId,...
       ebsd('indexed').mis2mean]...
    = calcGrains(ebsd('indexed'),'threshold',[LAGB HAGB]);
```

```
%% grain orientation spread (GOS) /no filter
min1 = 0;
max1 = 3;
GOSnoF = grains.GOS./degree; %calculate GOS

figure
%plot GOS
[~,m] = plot(grains,GOSnoF, 'colorrange', [min1 max1],...
    'micronbar', 'on')
%specify the length and background of the scalebar
m.micronBar.length = 1000;
m.micronBar.backgroundAlpha = 1;
```

```
mtexColorbar('title',...
'grain orientation spread [degrees]')
saveas(gcf,'GOS_nof.jpg')
```

```
%% Half-quadratic filter
    % filter to denoise + fill missing data
    %apply hf filter, parameters specified below
    F2 = halfQuadraticFilter;
    F2.alpha = 1;
    F2.threshold = 0.2618;
    F2.eps = 10^(-3);
    ebsd = smooth(ebsd('indexed'),F2,'fill',grains);
    [grainsQ,ebsd('indexed').grainId,...
        ebsd('indexed').mis2mean] ...
        = calcGrains(ebsd('indexed'),'threshold',...
        [LAGB HAGB]);
```

```
%% IPF map of the orientations in growth direction
%/halfquadratic filter

ipfKeyQ = ipfTSLKey(ebsd.orientations);
%specify the growth direction
ipfKeyQ.inversePoleFigureDirection = vector3d.Y;
 %specify the colour key
colorsQ = ipfKeyQ.orientation2color(ebsd.orientations);

figure
%plot the orientation map
hold on
[~,m] = plot(ebsd,colorsQ,'micronbar','on')
%specify length and background of the scalebar
m.micronBar.length = 1000;
m.micronBar.backgroundAlpha = 1;
hold off
hold on
%include grain boundaries in the plot
plot(grainsQ.boundary,'linewidth',2)
hold off
%To save the current figure, specify fig as gcf.
saveas(gcf,'YIPFmap_hf.jpg')
```

```
%% orientation distribution function /hf

%automatic halfwidth selection
%compute optimal halfwidth from the
%meanorientations of grains
```

```
psi = calcKernel(grains('Ti3AlN').meanOrientation)

% compute the ODF with the kernel psi
%orientations weighed with grain size
odfQ = calcDensity(grains.meanOrientation,'kernel',psi, ...
    'weights', grains.grainSize)

%now plot with optimal halfwidth
min = 0;
max = 2.5;
figure
%plot IPF of ODF in growth direction
plotIPDF(odfQ,yvector, 'colorrange', [min max])
mtexColorbar

%To save the current figure, specify fig as gcf.
saveas(gcf,'IPFODFy_hf.jpg')
```

```
%% Grain reference orientation deviation (GROD)
%with or without filter --> choose corresponding ebsd data
min = 0;
max = 4; %adapt depending on data so
%that misorientation at surface well visible
GROD = ebsd.calcGROD(grains);
figure
hold on
[~,m] = plot(ebsd,GROD.angle./degree,'colorrange', ...
    [min max],'micronbar','on')
m.micronBar.length = 1000;
m.micronBar.backgroundAlpha = 1;
hold off
hold on
plot(grains.boundary,'lineWidth',1.0)
hold off
mtexColorbar('title',...
    'misorientation angle to grain mean orientation [deg]')
mtexColorMap white2black

saveas(gcf,'GROD_noF.jpg')
```

```
%% select grain and line to determine rotation along a line
%select grain of interest by id
grain_selected = grains('id',7)

%define IPF key
ipfKey2 = ipfTSLKey(ebsdTop(grain_selected).orientations)
```

```
ipfKey2.inversePoleFigureDirection = vector3d.Y;
colors2 = ipfKey2.orientation2color...
(ebsdTop(grain_selected).orientations);

%plot grain + line along which rotation should be determined
figure
plot(grain_selected.boundary,'linewidth',1.0)
hold on
[~,m]=plot(ebsdTop(grain_selected),colors2)
hold off

%define line - adapt depending on data
lineSec = [0.915 1.815; 1.005 0.225];
line(lineSec(:,1),lineSec(:,2), 'linewidth',3,...
'color', 'black')
%save plot
saveas(gcf,'linegrain.jpg')

%select only those data points along the defined line
ebsd_line = spatialProfile(ebsdTop(grain_selected),lineSec);

min = 0;
max = 1.6; %distance of the line
%plot orientations along the line in an IPF
figure
plotIPDF(ebsd_line.orientations,[xvector,yvector,zvector],...
   'property',ebsd_line.y,'markersize',3,'antipodal',...
   'colorrange', [min max])
mtexColorbar('title','distance␣from␣starting␣point␣[\mum]')
mtexColorMap red2blue
%save plot
saveas(gcf,'rotationline.jpg')
```

A.3 Supplementary Images of the Surface of As-Deposited Samples

A.3.1 Variation of Surface Morphology

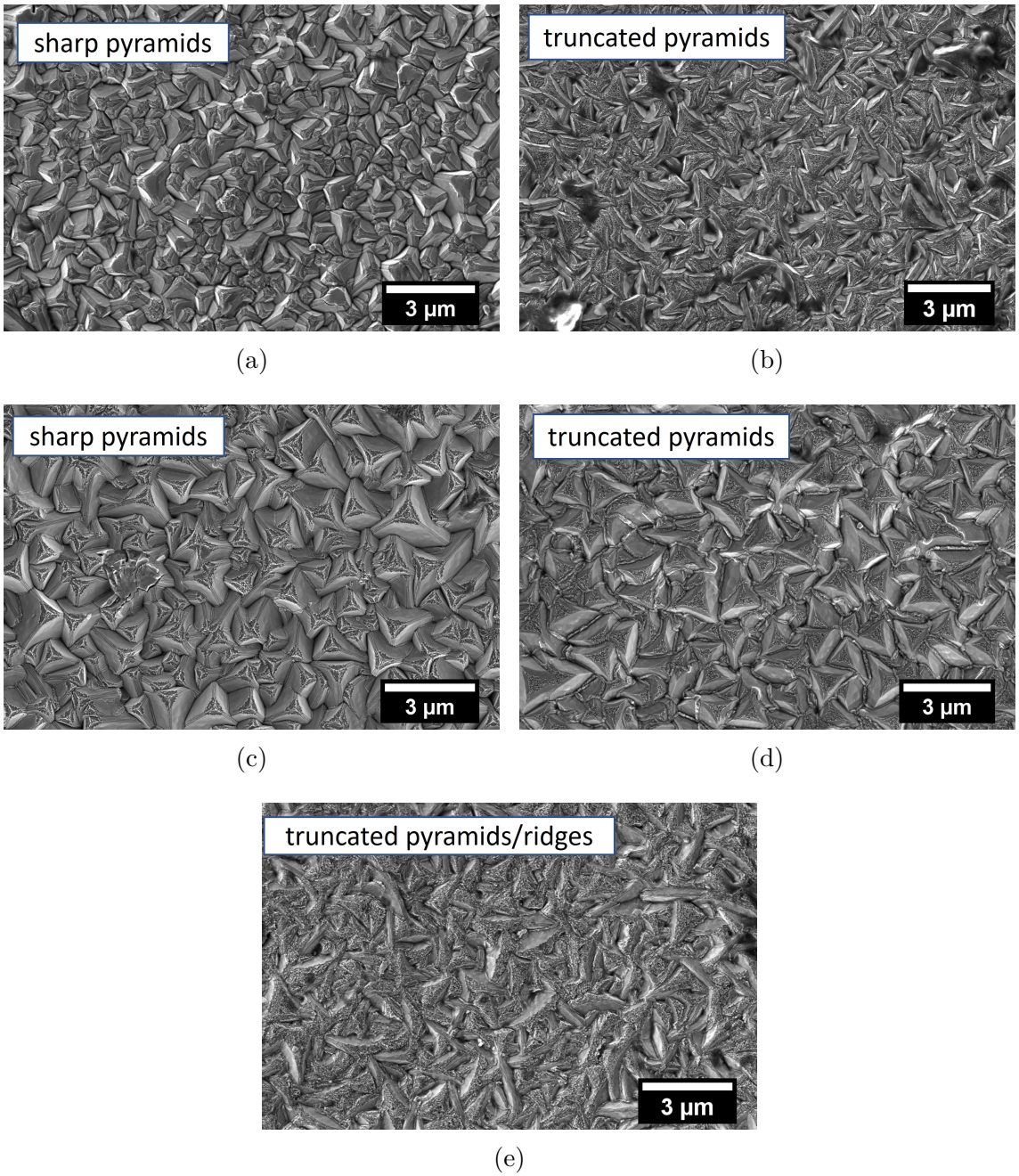

Figure A.1: Supplementary examples of the variations of the surface morphology and their categorization within this thesis. Imaged by SEM detecting SE with an in-lens detector.

A.3.2 Variation of Grain Size

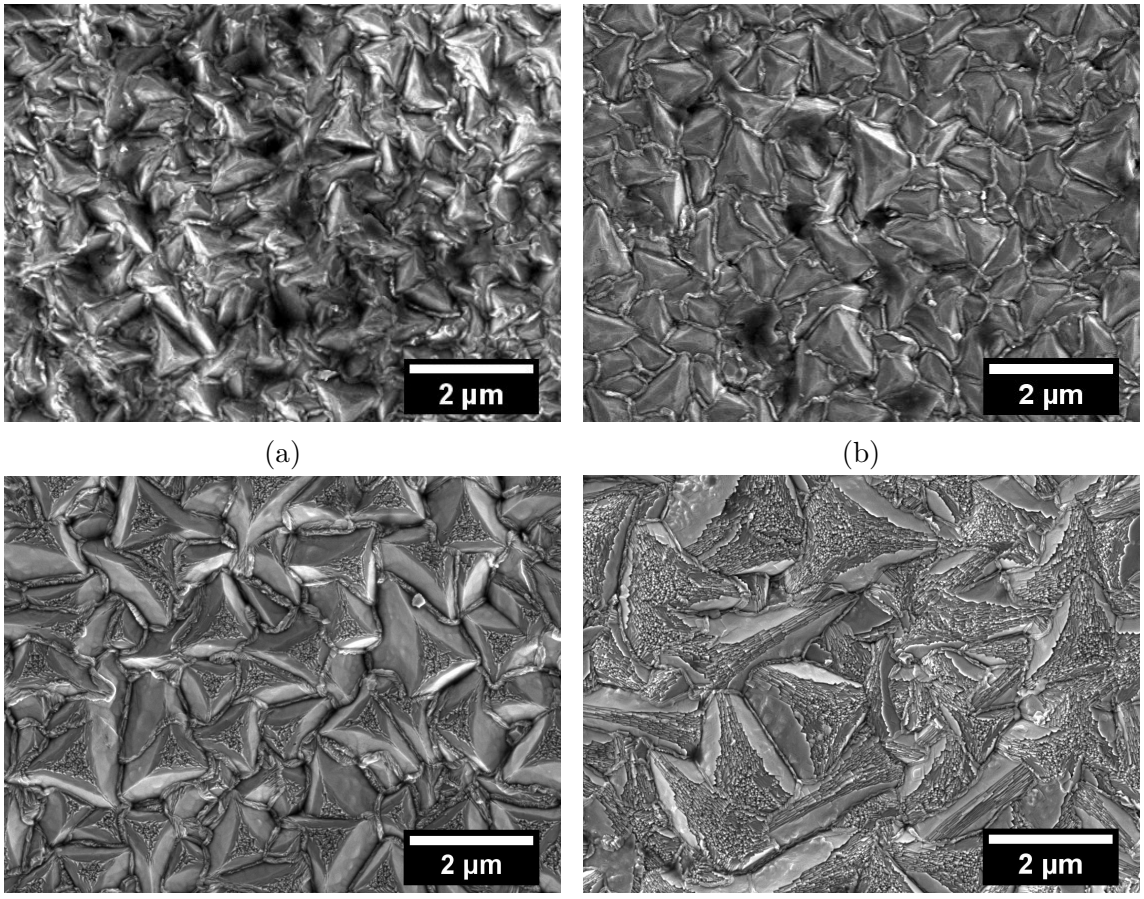

(a) (b)

(c) (d)

Figure A.2: Examples for varying grain size within one deposition run on a single insert and different inserts. Imaged by SEM detecting SE with an in-lens detector. (a) Smaller grains of sample 50_1_asdep. (b) Larger grains of sample 50_1_asdep. (c) Smaller grains of sample 50_2_asdep. (d) Larger grains of sample 50_2_asdep.

A.4 Supplementary Images of the Blast-Treated Surface

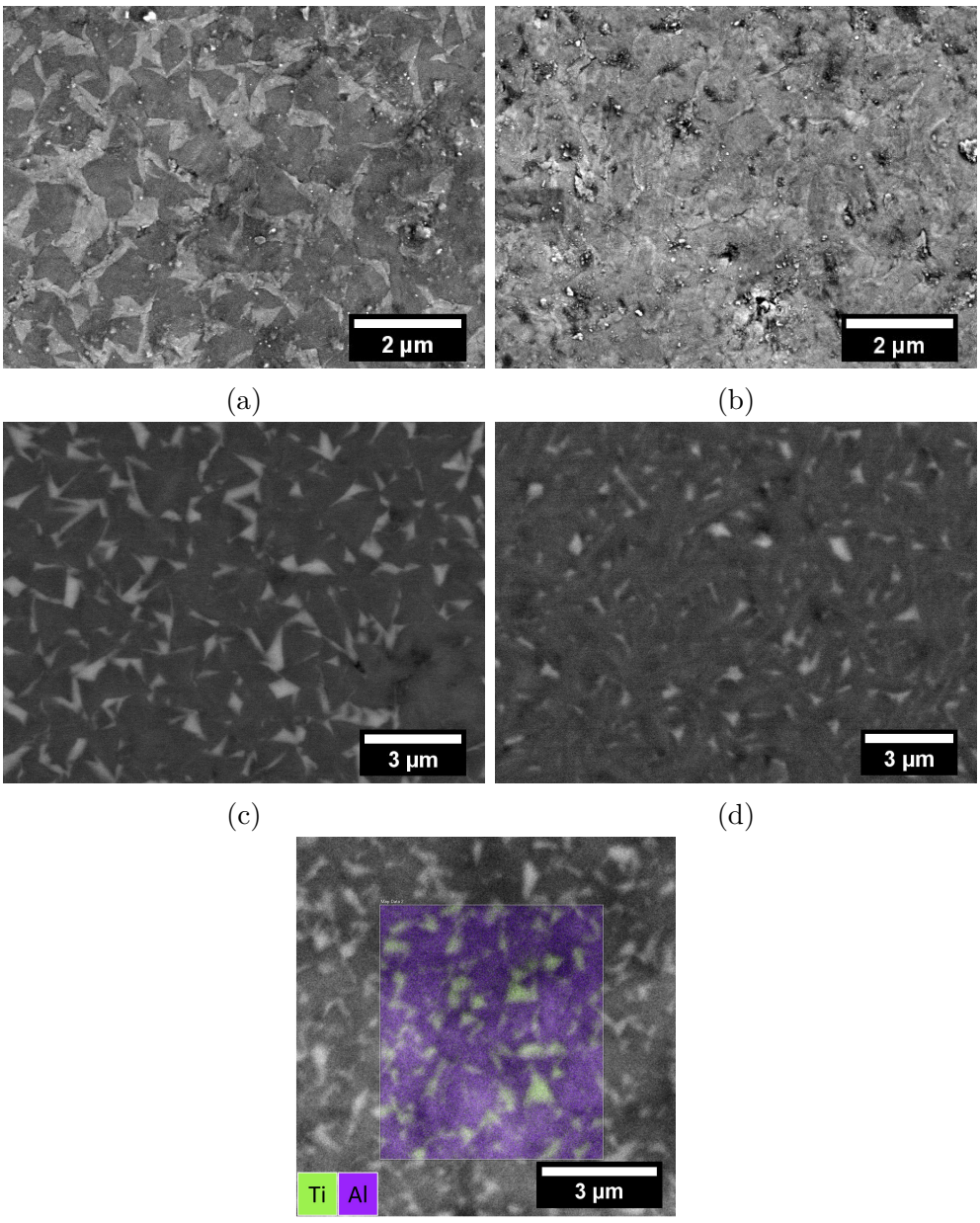

Figure A.3: (a) SEM SE in-lens image with presumably previously pyramidal grains. (b) SEM SE in-lens image with presumably previously ridge-like grains. (c) SEM BSE image with presumably previously pyramidal grains. (d) SEM BSE image with presumably previously ridge-like grains. (e) EDS map showing that areas that appear light in the SEM images have higher Ti content and substantially lower Al content compared to the darker appearing areas.

A.5 Example Images of Lamellae Observed in the TiAlN Coatings

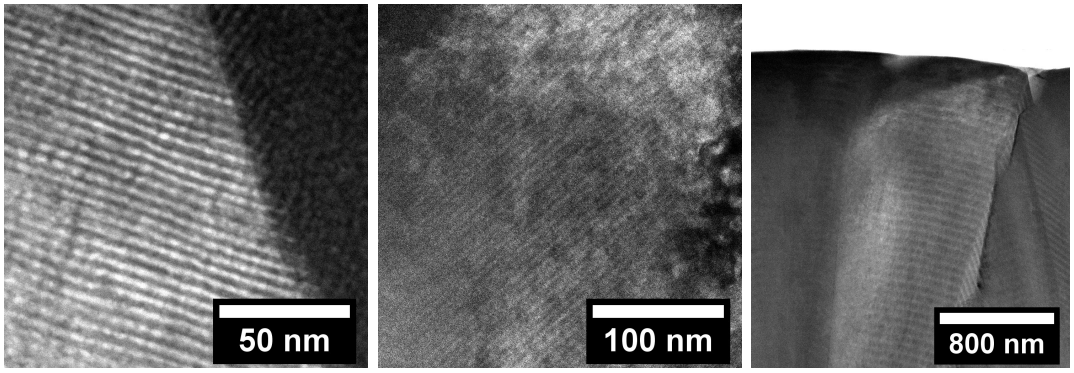

(a) (b) (c)

Figure A.4: Ti- and Al-rich nano-lamellae of the investigated samples. (a) Smallest periodicity. (b) Medium periodicity. (c) Largest periodicity.

A.6 Estimation of the Near-Surface Lattice Rotation Depth

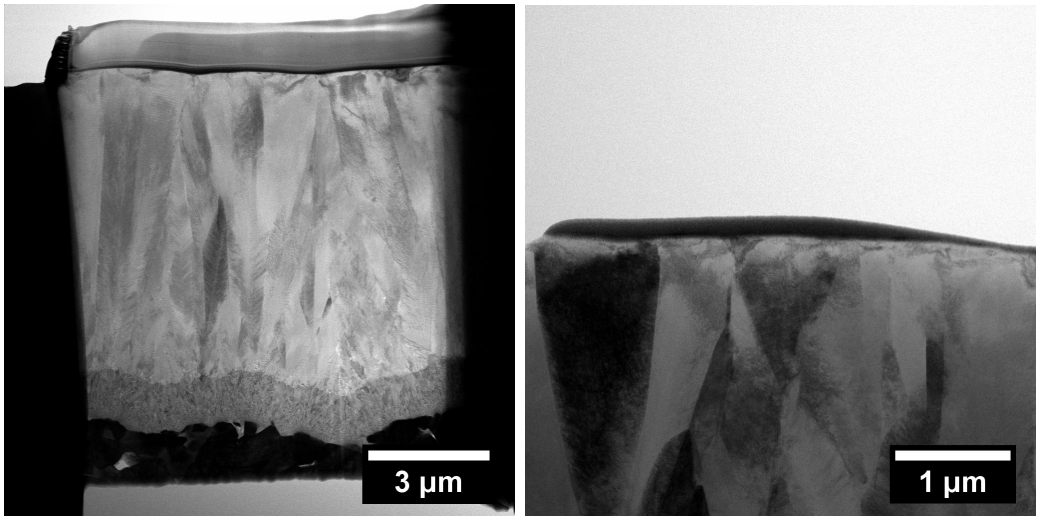

(a) (b)

Figure A.5: STEM BF images used to estimate the depth of the near-surface region strongly affected by blasting. (a) Sample 50_2_bltr. (b) Sample 6_1_bltr.

A.7 Quantification of the Deformation

By inserting the measured angles of $\zeta = 72.5°$ and $\theta = 125.7°$ represented in Figure A.6 into Equation 5.1 the strain can be calculated as follows:

$$\overline{\delta} = \left(1 - \frac{\tan\zeta}{\tan\theta}\right)\frac{\tan\theta}{\sqrt{3}} = \left(1 - \frac{\tan(72.5°)}{\tan(125.7°)}\right)\frac{\tan(125.7°)}{\sqrt{3}} = -2.6 \tag{A.1}$$

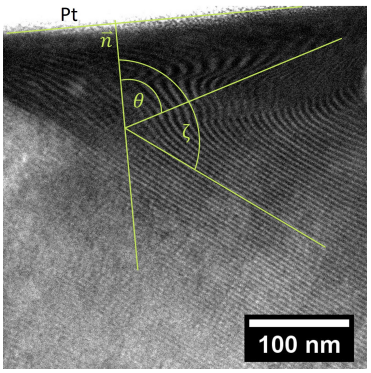

Figure A.6: Illustration of the angles ζ (between the feature before deformation and the normal of the shear stress plane $\vec{n}$) and θ (between the feature after deformation and the normal of the shear stress plane $\vec{n}$) used for the quantification of the present strain.

A.8 Supplementary GROD Plots

In the following, there are supplementary GROD plots illustrating that data from a region with preferred <110> growth directions shows a larger optimum maximum misorientation angle value for the colour bar than that from a region with preferred growth along <111> directions.

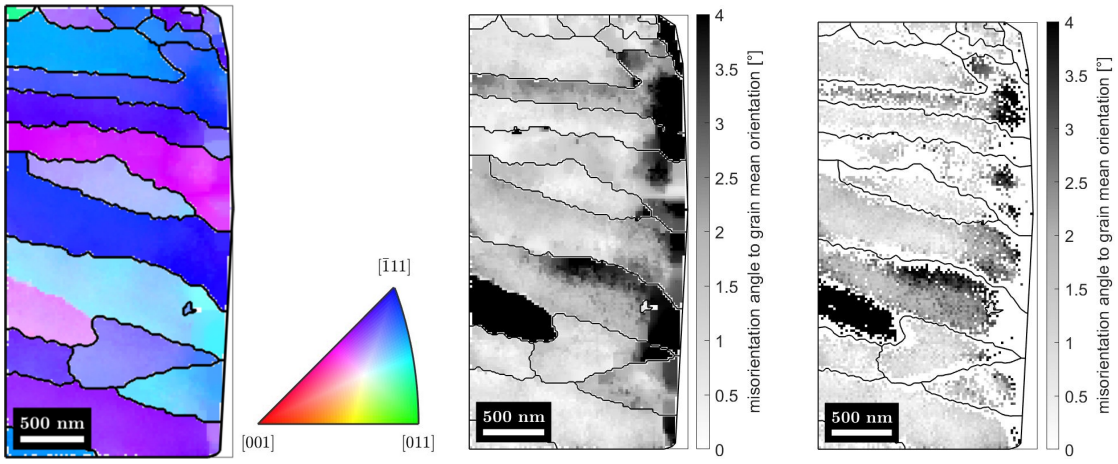

(a) (b) (c)

Figure A.7: The sample surface is on the right in all figures. (a) IPF orientation map shows a preferred orientation in <111> direction. (b) GROD determined from high-resolution TKD data of the surface region of the blast-treated coating. Data is denoised and missing data filled by filtering. High misorientation is found close to the coating surface. (c) GROD determined on raw data. Indexing worsens close to the coating surface.

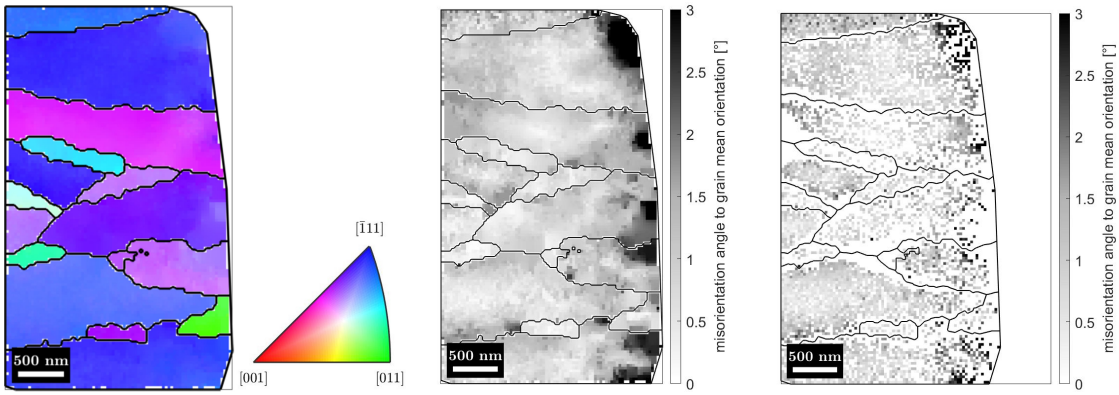

(a) (b) (c)

Figure A.8: The sample surface is on the right in all figures. (a) IPF orientation map shows a preferred orientation in <111> direction. (b) GROD determined from high-resolution TKD data of the surface region of the blast-treated coating. Data is denoised and missing data filled by filtering. High misorientation is found close to the coating surface. (c) GROD determined on raw data. Indexing worsens close to the coating surface.

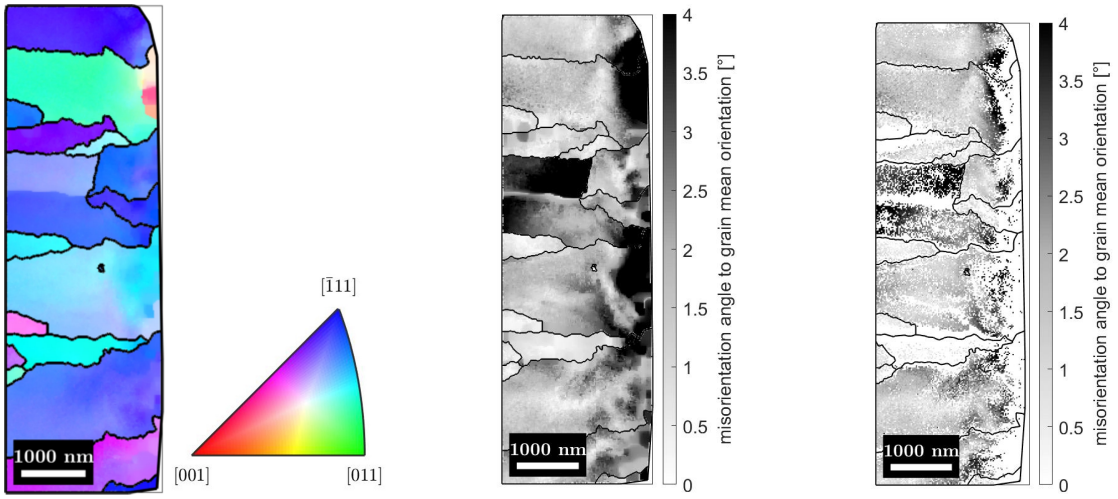

(a) (b) (c)

Figure A.9: The sample surface is on the right in all figures. (a) IPF orientation map shows a preferred orientation in <111> direction. (b) GROD determined from high-resolution TKD data of the surface region of the blast-treated coating. Data is denoised and missing data filled by filtering. High misorientation is found close to the coating surface. (c) GROD determined on raw data. Indexing worsens close to the coating surface.

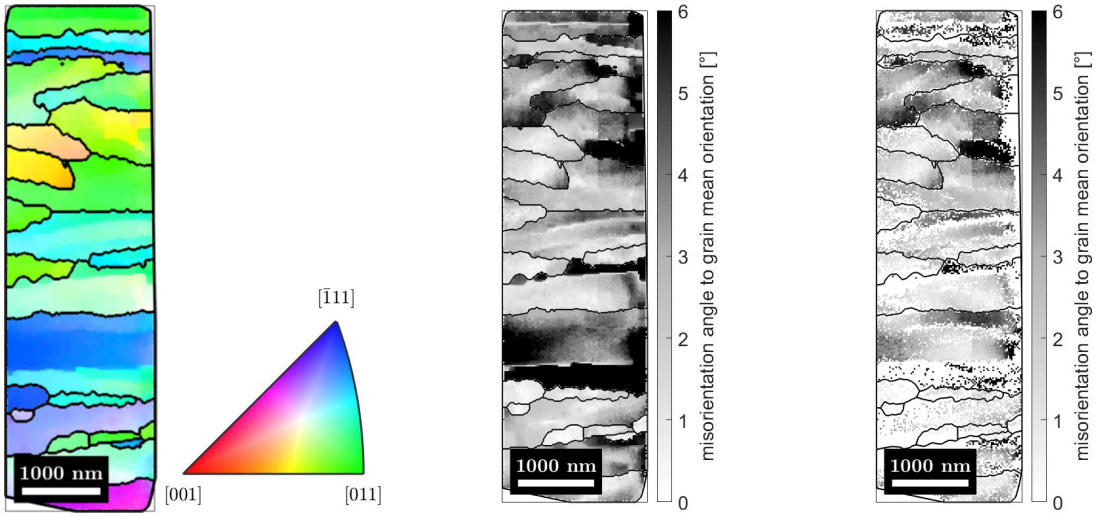

(a) (b) (c)

Figure A.10: The sample surface is on the right in all figures. (a) IPF orientation map shows a preferred orientation in <110> direction. (b) GROD determined from high-resolution TKD data of the surface region of the blast-treated coating. Data is denoised and missing data filled by filtering. High misorientation is found close to the coating surface. (c) GROD determined on raw data. Indexing worsens close to the coating surface.

DEPARTMENT OF PHYSICS
CHALMERS UNIVERSITY OF TECHNOLOGY
Gothenburg, Sweden
www.chalmers.se

CHALMERS
UNIVERSITY OF TECHNOLOGY